PORTABLE HIGH THROUGHPUT DIGITAL MICROFLUIDICS AND ON-CHIP

BACTERIA CULTURES

By

Yiyan Li

Bachelor of Science – Biomedical Engineering
Henan University of Science and Technology
2009

Master of Science – Biomedical Engineering
Chongqing University
2012

A dissertation submitted in partial fulfillment
of the requirements for the

Doctor of Philosophy – Electrical Engineering

Department of Electrical and Computer Engineering
Howard R. Hughes College of Engineering
The Graduate College

University of Nevada, Las Vegas
May 2016

Dissertation Approval

The Graduate College
The University of Nevada, Las Vegas

April 14, 2016

This dissertation prepared by

Yiyan Li

entitled

Portable High Throughput Digital Microfluidics and On-Chip Bacteria Cultures

is approved in partial fulfillment of the requirements for the degree of

Doctor of Philosophy – Electrical Engineering
Department of Electrical and Computer Engineering

Russel Jacob Baker, Ph.D.
Examination Committee Chair

Rama Venkat, Ph.D.
Examination Committee Member

Peter Stubberud, Ph.D.
Examination Committee Member

Hui Zhao, Ph.D.
Graduate College Faculty Representative

Kathryn Hausbeck Korgan, Ph.D.
Graduate College Interim Dean

Abstract

An intelligent, portable, and high throughput digital microfluidic (DMF) system is developed. Chapter 1 introduces microfluidics and DMF systems. In Chapter 2, a low-cost and high-resolution capacitive-to-digital converter integrated circuit is used for droplet position detection. A field-programmable gate array FPGA is used as the integrated logic hub of the system for highly reliable and efficient control of the circuit. In this chapter a fast-fabricating PCB (printed circuit board) substrate microfluidic system is proposed. Smaller actuation threshold voltages than those previously reported are obtained. Droplets (3 µL) are actuated using 200 V, 500 Hz DC pulses. Droplet positions can be detected and displayed on a PC-based 3D animation in real time. The actuators and the capacitance sensing circuits are implemented on one PCB to reduce the size of the system. In Chapter 3, an intelligent EWOD (electrowetting on dielectric) top plate control system is proposed. The dynamic top plate is controlled by a piezoelectric (PZT) cantilever structure. A high resolution laser displacement sensor is used to monitor the deflection of the top plate. The gap height optimization and the harmonic vibration significantly improve the droplet velocity and decrease the droplet minimum threshold actuation voltage. The top plate vibration induced actuation improvement is magnitude and frequency dependent. 100 µm and 200 µm vibrations are tested at 25 Hz. Vibration frequencies at 5 Hz, 10 Hz, and 20 Hz are tested while the magnitude is 200 µm. Results show greater improvements are achieved at larger vibration magnitudes and higher vibration frequencies. With a vibrated top plate, the largest reduction of the actuation voltage is 76 V_{RMS} for a 2.0 µl DI water droplet. The maximum droplet instantaneous velocity is around 9.3 mm/s, which is almost 3 times faster than the droplet velocity without top plate vibration. Liquid that has different hysteresis such as acetonitrile with various concentrations are used as a control to show its compatibility with the proposed DMF

chip. Contact line depinning under top plate vibration is observed, which indicates the underlying mechanism for the improvements in actuation velocity and threshold voltage. The top plate control technique reported in this study makes EWOD DMF chips more reliable for point-of-care diagnostics. In Chapter 4, the mechanisms of the improvements were investigated by observing the detailed changes in the contact angle hysteresis using both parallel and non-parallel top plates. In Chapter 5, on-chip cell cultures are used for anti-biotic resistant bacteria detection. The passively dispensed on-chip cell cultures realize the isolated micro environment electrochemistry measurement, shorten the culturing time, and reduce the required sample volume. The design of the next generation ultra-portable DMF system is covered in the Appendix. Detailed technical notes and hardware design is covered in the Appendix. The proposed portable and high throughput DMF system with on-chip cell cultures have a great potential to change the standards for micro-environment culturing technologies, which will significantly improve the efficiency of actuation, sensing, and detecting performance of the DMF systems.

Table of Contents

viii

List of tables

List of figures

Chapter 1 Introduction to microfluidics and digital microfluidics

1.1 Microfluidics and capillary effects

Microfluidics is a multidisciplinary area that has been rapidly developing since the beginning of the 1980s. The most successful commercial application of microfluidics is inkjet printers (Inkjet printers zoom into the office market.1979). Microfluidics has been used for immunoassay preparation (Ng et al., 2015; Shamsi, Choi, Ng, & Wheeler, 2014), protein depletion (Mei, Seale, Ng, Wheeler, & Oleschuk, 2014), DNA amplification (Zhang, Xu, Ma, & Zheng, 2006) and any fluidic microelectromechanical systems (Kwapiszewski et al., 2011; C. S. Nelson et al., 2013; Nery et al., 2014; Truckenmüller et al., 2011). Microfluidics refers to liquids in small volumes ($\leq$ 1 µL) where the surface tension dominates the dynamics of the interface between the liquid, gas, and solid. In Fig. 1.1, $\sigma_{solid-gas}$, $\sigma_{solid-liquid}$, and $\sigma_{liquid-gas}$ are the surface tensions of the liquid-gas, solid-liquid, and the solid-gas interfaces. Therefore, according to Young's equation for the relation at the contact line, we can get：

$$\sigma_{solid-liquid} + \sigma_{liquid-gas}cos\theta = \sigma_{solid-gas} \qquad (1.1)$$

$$cos\theta = \frac{\sigma_{solid-gas} - \sigma_{solid-liquid}}{\sigma_{liquid-gas}} \qquad (1.2)$$
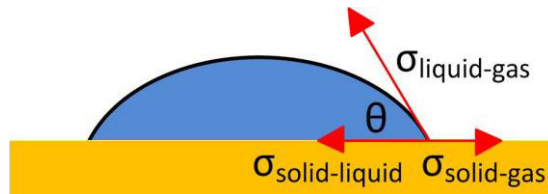
Fig. 1.1 Droplet wetting on a solid surface.

The droplet tends to be in a spherical shape to minimize the surface contact area. However, the surface contact area depends on the combined tension between the three phases (Fig. 1.2).

The surface is considered as totally wetted when the contact angle $\theta = 0^\circ$, and hydrophilic when the contact angle $0^\circ < \theta < 90^\circ$, and hydrophobic when $90^\circ \leq \theta < 180^\circ$, and not wetted when $\theta \geq 180^\circ$.
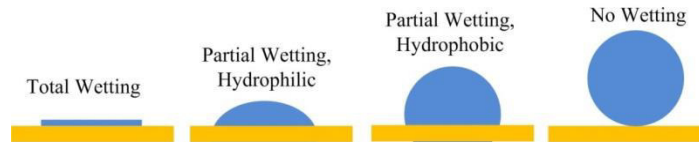
Fig. 1.2 Surface wetting properties.

1.2 Contact angle hysteresis

When a droplet is dispensed by a syringe to the surface, the contact angle does not change. When the droplet is getting bigger and bigger, the contact line starts moving forward, the threshold contact angle that the contact line starts advancing is called 'advancing angle' (Fig. 1.3a); the threshold contact angle that the contact line starts receding is called 'receding angle' (Fig. 1.3b). Contact angle hysteresis is the difference between the advancing angle θ_a and the receding angle θ_r. Contact angle hysteresis is generally attributed to surface roughness, surface heterogeneity, and solution impurities adsorbing on the surface. Advancing contact angle is always larger than the receding contact angle ($\theta_a > \theta_r$).
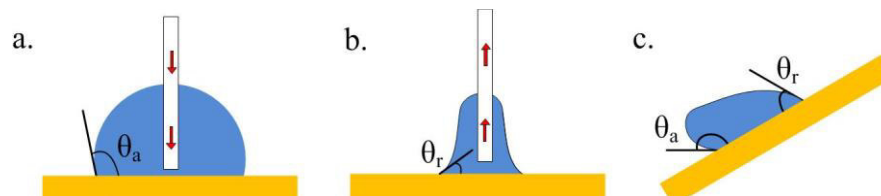
Fig. 1.3 Measurement of contact angle hysteresis. (a and b) Injecting a small droplet on to the surface to measure the hysteresis. (c) Using an inclined surface to measure the hysteresis.

An alternative method to measure the contact angle is when the droplet starts rolling down an inclined surface, the downhill side contact angle is the advancing angle; the uphill side contact angle is the receding angle.

The static hysteresis is very stable, but the moving droplet has a different hysteresis on the same surface. The typical curve for the hysteresis versus the capillary number is shown in Fig. 1.4. At the velocity of 0, there is a gap between the two curves. This gap (difference) is the static contact angle hysteresis. The dynamic contact angle hysteresis increases as the droplet velocity increases. The capillary number is defined as the ratio of viscosity (η) and velocity (U) to liquid vapor interfacial tension (γ_{lv}).
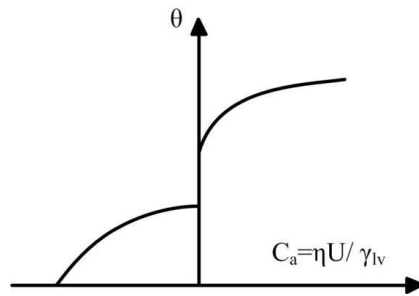
Fig. 1.4 Contact angle hysteresis versus capillary number (velocity). The curve on the right hand side represents the advancing contact angle; the left hand side represents the receding angle.

The theoretical advancing and receding angles are separated by an energy barrier. A slight vibration may shift the angle to the global minimum in energy. Therefore, the experimentally measured hysteresis will be smaller than the theoretical one. This is the potential underlying mechanism of the actuation velocity improvements we achieved by using a vibrated top plate in the EWOD system. More details will be covered in detail in Chapters. 3 and 4. Contact angle hysteresis has been considered as a resistive force to droplet moving in the electrowetting-on-dielectrics (EWOD) systems (Y. Li, Baker, & Raad, 2016).

1.3 Eletrowetting on dielectric digital microfluidics (EWOD DMF)

There are mainly two branches in microfluidics. One is continuous flow microfluidics (Kuntaegowdanahalli, Bhagat, Kumar, & Papautsky, 2009; Kwapiszewski et al., 2011; Mach & Di Carlo, 2010; Seo et al., 2005), which is usually controlled by an external pump and transports fluids continuously within capillary tubes and channels. The other one is droplet-based microfluidics, which can be droplets in channels in immiscible phases with low Reynolds number and laminar flow regimes (Kang et al., 2014; M. Kim et al., 2015) or digital microfluidics (DMF) (Barbulovic-Nad, Yang, Park, & Wheeler, 2008; Fair, 2007; Wheeler et al., 2005) on discrete electrodes. In which, DMF can deliver discrete micro droplets and manipulate droplet behaviors (mixing, actuating and splitting) by digital microcontrollers.

Things become easier and more attractive when the microfluidic chip is interfaced with digital devices. By using microcontrollers or FPGAs (field-programmable gate array), DMF can manipulate a large array of droplets in parallel, which is critical for high throughput microfluidic experiments. With the advances in microelectronics, all DMF controlling and driving devices can fit into a portable box. In DMF, one of the main physical and mechanical principles of moving droplet on a surface is EWOD. EWOD describes a configuration in which an insulating layer separates the working liquid and actuation electrodes. Despite the much higher voltage needed, e.g., 100 V (Vallet, Berge, & Vovelle, 1996) in earlier work and 15-80 V in current work (Lin et al., 2010), EWOD is the preferred arrangement over the traditional direct electrowetting on conductor for two main reasons: 1. Insulators guard working fluids from electrodes, thereby allowing a much higher electric field (strong electrowetting effect) before an electrical leakage or breakdown. 2. One can coat a thin layer of super hydrophobic material on the surface of the chip,

on which the contact angle hysteresis is smaller, thereby allowing the working fluids to be actuated easily.

Voltages applied to the EWOD devices gives rise to electric fringe fields close to the contact line and thus results in a Maxwell stress, which pulls on the liquid surface (Fig. 1.5). In order to balance this stress, the shape of the drop surface has to be curved to keep the Laplace pressure ΔP_L balancing the Maxwell stress everywhere along the surface (Mugele & Baret, 2005; Mugele, 2009). In other words, the surface wettability of becomes tunable when a voltage is applied.
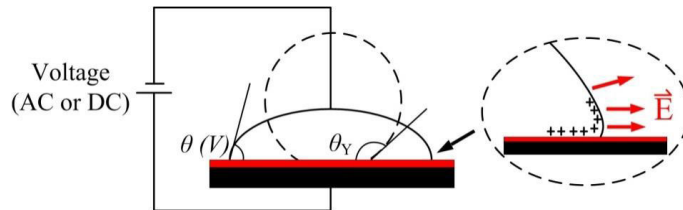
Fig. 1.5 Droplet on an insulation layer (red box) at zero voltage (dashed). A voltage is applied to the electrode (black box) and the shape of the droplet is deformed.

The modern EWOD digital microfluidics uses this asymmetrical electrostatic force created on both sides of the contact line to accurately control the actuation of the drop.

However, there are two main configurations for the EWOD system: single-plate configuration and dual-plate configuration (Fig. 1.6). The single-plate configuration requires grounded neighbor electrodes at the bottom substrate; while the dual-plate configuration requires the top substrate to be grounded. In electrowetting, the electric field applied to the solid surface and the conductive liquid balances the forces at the contact point. Using EWOD there is an insulating layer deposited onto the electrodes. The capacitance of the dielectric material dominates the capacitance of the double layer at the solid-liquid interface.
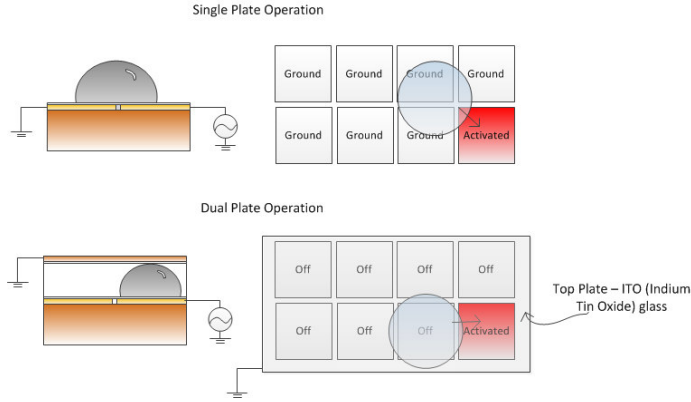
Fig. 1.6 Single-plate and dual-plate EWOD systems.

The variation of the contact angle follows the Lippmann-Young equation:

$$cos\theta = cos\theta_0 + \frac{\varepsilon_0\varepsilon_d}{2d\sigma_{lv}}U^2 \tag{1.3}$$

in which θ_0 is Young's equilibrium contact angle, ε_d is the dielectric constant of the insulation layer, d is the thickness of the insulation layer, σ_{lv} is the liquid-vapor surface tension, U is the applied voltage. When the applied voltage increases, the contact angle decreases very quickly until it is saturated. For typical values: $\sigma_{lv} = 0.072\,J \cdot m^{-2}$ and the dielectric material layer thickness is $d = 8\,\mu m$). The Lippmann-Young equation is plotted in Fig. 1.7.
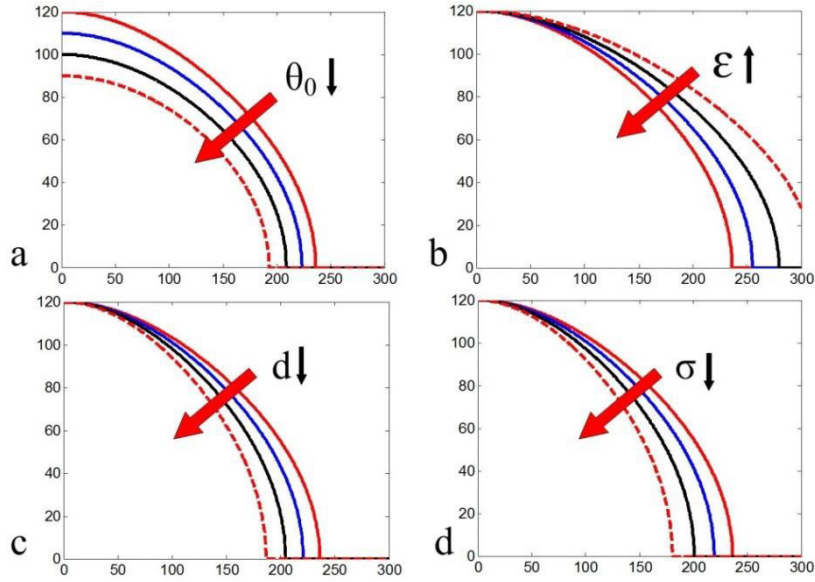
Fig. 1.7 Contact angles under voltages in EWOD. a. Varying the initial contact angle; b. varying the insulating layer dielectric constant; c. Varying the dielectric layer thickness; d. Varying the surface intension.

In Fig. 1.7, we plotted the Lippmann-Young equation by varying each of the variables in the equation and keep other variables fixed. The simulation parameters are shown in the following table:

Table 1.1 Parameters used for Lippmann-Young equation plotting in Fig. 1.7.

	θ_0 Degree	ε relative	d μm	σ J·m-2
(a)	120, 110, 100, 90	3.5	8	0.072
(b)	120	3.5, 3, 2.5, 2	8	0.072
(c)	120	3.5	8, 7, 6, 5	0.072
(d)	120	3.5	8	0.072, 0.062, 0.052, 0.042

The theoretical contact angle with voltages applied in EWOD goes down to 0 when the voltage is high enough. But in the real world, the contact angle variation saturates at some point, regardless of an increased voltage, and the droplet can't be deformed any more. A comparison of the experimental data and the theoretical data can be found in Fig. 3.32. Unfortunately, the contact angle saturation is not totally understood. There is no physical model that explains the saturated condition. Another limitation of Equation 1.3 is the incapability of taking the contact angle hysteresis into consideration. The experimental data can agree with this theory only in a perfectly slippery (low bonding number) surface (Baratian, Cavalli, van den Ende, & Mugele, 2015), in which the EWOD contact angle variation is totally reversible. In fact, the contact angle cannot recover to the initial value by turning off the voltage, which is caused by the hysteresis. Finally, the model becomes more and more complex if the time domain is considered. The gravity of the droplet is neglected in these models. But in reality, the contact angle will change in a small range in the time domain due to the pressure that originates from gravity.

1.4 Lower the driving voltage, speed up the actuation, and monitor droplet position

1.4.1 Lower the driving voltage

Decreasing the voltage applied to the electrode can reduce the size of the driving circuit and therefore increase the scale of the electrode array. A 15 V driving circuit has been able to transport a 460 nL water droplet, which is achieved by increasing the dielectric constant and decreasing the thickness of the dielectric layer (Cho, Moon, & Kim, 2003; Moon, Cho, & Garrell, 2002). The applied voltage and droplet's volume have a great influence on the velocity of the droplet moving on the surface. To move a 2 µL water droplet, when the voltage is larger than 10 volts, the velocity increases exponentially with the increase of the applied voltage (J. Chang, Choi, Han, & Pak, 2010), and the threshold voltage of droplet actuation decreases.

There have been many attempts to lower the EWOD driving voltage. According to Lippmann-Young equation, the voltage can be reduced by decreasing the liquid-dielectric interfacial tension, using an oil environment or surfactant. The threshold voltages depend on the dielectric properties for water droplets in an air or oil environment with the absence of the surfactant (Cho et al., 2003; Cooney, Chen, Emerling, Nadim, & Sterling, 2006; N. Kim, Hong, Park, & Hong, 2006; Moon et al., 2002; M. Pollack, Shenderov, & Fair, 2002; M. G. Pollack, Fair, & Shenderov, 2000). The frequency of the AC voltage directly affects the contact angle, and low frequencies seem more stable than higher frequencies (Nanayakkara et al., 2010).

The normally used layers are CYTOP, Aluminum, SiO_2, and Silicon. CYTOP is directly contacted with the droplet. The thickness of CYTOP, Aluminum and SiO_2 layers should be as thin as several hundred nanometers to insure a low threshold voltage. Devices with 1mm×1mm electrodes coated with 70 nm BST films deposited by metal-oxide chemical vapor deposition (Y. Li et al., 2008; Moon et al., 2002) and 95 nm anodic Ta_2O_5 films (Moon et al., 2002) both reached the relatively low threshold voltage of 15 V. Both materials were coated with a thin fluoropolymer film additionally. The ratio of effective insulator thickness to dielectric constant is the main factor of the required actuation voltage. Even in the same structure, the higher dielectric constant material may not result in lower actuation voltage, and it depends on the film thickness and the hydrophobic layer's properties (Y. Li et al., 2008; Lin et al., 2010). However, the trade-off is using thinner dielectric layer harms the reliability of the surface and causes pin-holes.

1.4.2 Speed up the actuation

The actuation speed is mainly dependent on the roughness of the hydrophobic surface, the composition of the droplet, the strength of the electric field for the EWOD modulation and the driving voltages applied. Many attempts have been made to improve the actuation speed. For

example, using a single-plate topology to avoid extra friction from the top plate (Banerjee, Qian, & Joo, 2011), using silicone oil environment in the chamber to increase the contact angle changes and therefore increase the electrostatic force the droplets experience (Brassard, Malic, Normandin, Tabrizian, & Veres, 2008). Additional efforts have been made in modulating the driving voltages to increase the actuation speed. Single DC (J. Hong, Kim, Kang, Oh, & Kang, 2013) pulse, DC pulse train (Koo & Kim, 2013), AC waves (Abdelgawad & Wheeler, 2007; Abdelgawad & Wheeler, 2008) and even some pulse width modified voltages (T. Chen et al., 2014; Dong et al., 2014; Murran & Najjaran, 2012a) have been investigated to enhance the speed of the droplets. Using a single DC pulse at the electrode adjacent to the droplet will drag the droplet immediately toward the activated electrode. When a single DC pulse is added to the electrode, the droplet is suddenly accelerated, which will cause overshoot or even fragmentation (Murran & Najjaran, 2012a). At the same time if the electrode is driven with a single DC pulse, a double layer (Quinn, Sedev, & Ralston, 2003) or a polarized dipole will be created at the droplet-insulator interface and then increase the capacitance. Large droplet hysteresis may occur in this case. If AC waves are used they constantly alternate the polarizations and no hysteresis problem is observed.

1.4.3 Droplet position detection

The reliability of an automated microfluidic system depends on its self-surveillance capabilities. To avoid incorrect movements of the droplets the controlling computer should be able to identify the position and control the destination of the droplets. If the droplet does not go to an expected destination the computer should create an error log and notify the operator. Optical surveillance systems using cameras have solved this problem to some extent (Basu, 2013; Ren, Fair, & Pollack, 2004); an optical droplet tracking software developed by Basu (Basu, 2013)

shows great performance in extracting the droplet edges from a background and measuring the velocity of the droplet's movements. However, optical monitoring techniques require high-resolution source image frames, so the experiment process has to be recorded in a specific optical environment. Some experiments using optic-phobic solutions such as argentum nitricum, potassium iodide, and potassium thiosulfate cannot be tracked using this technique.

Electrode capacitance is sensitive to droplet size, composition, velocity and position. Studies using capacitive sensors to identify the droplet's parameters are showing reliable performance by detecting capacitance changes (Murran & Najjaran, 2012b; Ren et al., 2004; Schertzer, Ben-Mrad, & Sullivan, 2010). We apply these parameters to track the droplets instead of using optical techniques. Using conventional bench single-channel capacitance meters (which are large in size) (Murran & Najjaran, 2012b; Schertzer et al., 2010) is good for testing the capacitance of a single electrode pair, however, this approach suffers from several limitations including low resolution, uncontrollable outputs, physical size, and a mono-channel output. With the advances in integrated circuit (IC) design, capacitance data can be directly read out of a serial communication port from an all-in-one IC performing a capacitance-to-digital conversion (CDC). For example, the AD7745 (Analog Devices, Inc., MA, USA) is a high-resolution (24-bit) CDC with a maximum measurement range from a couple of picofarads (pF) to 48 pF. The resolution of the sensor goes down to 4 femtofarads (fF). High-reliability and stability were reported in a 24-hour period monitoring the humidity, temperature, and capacitance of a sensor system (Brassard et al., 2008). The potential applications of this high-resolution CDC IC chip are numerous. Another useful property of a capacitive sensor is that droplet position detection can be implemented (Y. Li, Li, & Baker, 2015). The current capacitive sensor developed in our preliminary research work is good enough for the droplet position detection of small electrode arrays. Larger electrode

arrays need a much faster response to realize the real-time "capacitive vision" concept developed

in our initial work (Y. Li et al., 2015). More details will be covered in Chapter 2, section 2.3.

Chapter 2 PCB digital microfluidics

Printed Circuit Board (PCB) substrate microfluidic chips, biosensors and actuators can be prototyped very quickly in a very low cost. The standard PCB fabrication process is mature. There are several open-source CAD tools to layout the circuit board into a 3-D structure, which means the components can be connected by the wires travelling through vias and multi-layer laminated metal networks. It is far more difficult to stack a 3-D metal network structure on silicon and glass. This multi-layer structure allows a bigger electrode matrix layout (Gong, 2008). Industrially standardized interfaces, pins, cables, and control units can be easily integrated into the electrode array substrate without any post-fabrications. However, one of the major limitations of using PCB substrate are the minimum metal space is too big for the microfluidic device. Due to this limitation, the droplet volume cannot be too small. Another limitation is the surface roughness is huge compared to glass and silicon, which leads to larger contact angle hysteresis and larger driving voltages. The large driving voltage in turn, will jeopardize the integrity of the dielectric layer. In this chapter, the PCB digital microfluidic substrate is tested in section 2.1; a liquid concentration detector (section 2.2) and a droplet position system (section 2.3) are developed.

2.1 A fast fabricating electrowetting platform to implement large droplet manipulation

2.1.1 Introduction

Reliable batch processing of rat brain samples is a critical and difficult issue in immunohistochemistry experiments. Conventionally, in tissue immuno-staining experiments, the neurologists use tweezers or hooks to move the micro-meter thick brain sections, which contain important data, from one petri dish to another. This process is repeated several times to complete the process steps present in an immunohistochemistry experiment. The brain sections are very

easily cracked along the boundary of the cortex and the mesencephalon during this process due to the hard dragging and frequently movements by the metal handling instruments. In many experiments, the result is a loss of data from, for example, a monthly prepared tissue sample. Current lab-automation techniques implemented by Electrowetting (M. S. Kim et al., 2010; M. G. Pollack et al., 2000) and Dielectrophoresis (Medoro et al., 2003; H. Zhao, 2011) are providing promising solutions to automate the experimental procedures and reduce the tissue damage. However, very few studies have tried to modify a platform specifically suitable for a rat's brain section immunohistochemistry staining. Because areas of tyrosine hydroxylase cells are in a range of about 4 mm, the conventional electro-wetting platforms are too small to wet the tissues efficiently. Further, fabricating an electro-wetting system using photolithographic techniques requires clean room facilities and expensive prototyping masks. To simplify the procedures this work develops a low-cost electro-wetting platform on a printed-circuit board (PCB) with large electrodes. The specific goal of this platform is for applications in rats' brain sections staining. The post-processed PCB array presented here can move large droplets (~30 μL) with a much smaller voltage and frequency than previously reported (Abdelgawad & Wheeler, 2008). Voltage / frequency related performance and limitations of the PCB microfluidic system are also investigated. Result shows that it is a promising technique to assist neurologists in conducting tissue staining experiments.

2.1.2 Materials and methods

A standard (FR-4, glass epoxy) double-sided PCB board (Advanced Circuits, Tempe, AZ, USA) is used for the substrate material. A PIC24FJ96 microcontroller (Microchip, USA) is used to control the operation of the circuit. The droplet operation can be pre-programed as self-running

or it can be controlled in real-time with keyboard commands. The high-voltage module (EMCO F40, EMCO, Schweiz, Switzerland) is capable of supplying a DC voltage from 0 to 2000 V.

A high-voltage square wave is created at the drains, B0-B17, of NMOS transistors (VN2460) seen below in Fig. 2.1. P0-P17 are connected to the I/O ports of the microcontroller. For example, if P0 goes high then B0 goes low. If P0 goes low then B0 is pulled to the High DC Voltage through a resistor.
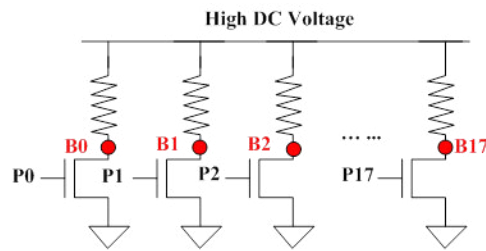
Fig. 2.1 Schematic of the voltage supply circuit.

The electrodes are made using bare copper rectangles on the top of the PCB. A plastic sheet (Saran Wrap, 15 µm thick polyethylene) (Abdelgawad & Wheeler, 2008) is cut in suitable size and coated on the top of the electrodes. Before the Saran Wrap is put on the top of the copper electrodes, a tissue is used to dampen a thin layer of peanut oil (or any other kitchen oil) on the top of the electrodes to help repel air bubbles that form on top of the electrodes. Peanut oil is also placed on top of Saran Wrap to create a hydrophobic surface. We did not use a commercial water-repellant liquid, such as Rain-X (Abdelgawad & Wheeler, 2008) to create the hydrophobic surface for our experiments. Peanut oil is used instead due to the capability of creating a larger contact angle than possible with Rain-X.

Both single- and dual-plate operation were investigated in the work reported here. For single-plate operation the droplet must bridge two adjacent electrodes. To move the droplet, one plate (colored gold in Fig. 2.2) is activated (driven to a high voltage) while the other plate is grounded.

The droplet moves towards the activated plate. In a dual-plate operation topology the top plate is grounded so the droplet does not have to bridge two electrodes for movement to occur. In our dual plate experiments the top plate is made by ITO glasses (Adafruit, NYC, USA) and coated with a layer of Saran Wrap.
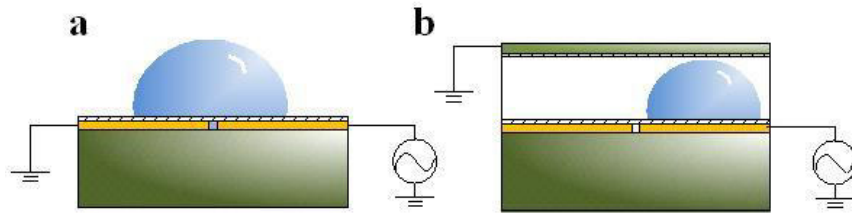
Fig. 2.2 Diagram of single plate operation (a), and dual plate operation (b).

A diagram showing the electrowetting system is seen in Fig. 2.3. The control section of the system is a separate board, with display and keyboard. The electrode array is placed along with the high-voltage supply on its own board. A cable is used to connect the control board to the array board.
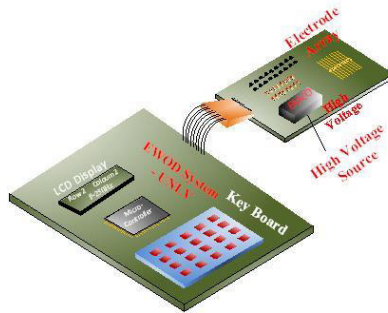
Fig. 2.3 Diagram of the electro-wetting system.

The contact angle is approximated (Fig. 2.4) and calculated as following:
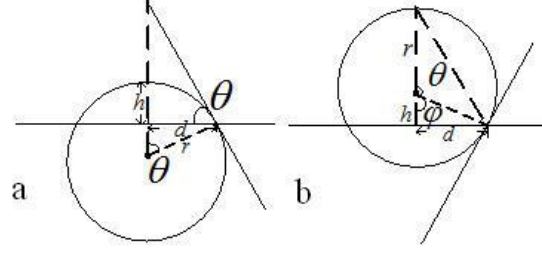
Fig. 2.4 (a) Diagram showing how the contact angle is calculated if the contact angle is less than 90˚. (b) Contact angle calculation if it is larger than 90˚.

Assuming θ is the contact angle, and that d and h are known, then for (a),

$$\tan \theta = \frac{d}{r-h}, \quad d^2 + (r-h)^2 = r^2 \tag{2.1}$$

$$d^2 + r^2 + h^2 - 2rh = r^2, \quad r = \frac{d^2 + h^2}{2h} \tag{2.2}$$

$$\tan \theta = \frac{2hd}{d^2 - h^2}, \quad \theta = \arctan \frac{2hd}{d^2 - h^2} \tag{2.3}$$

and for (b)

$$\tan \theta = -\tan \varphi, \quad \tan \varphi = \frac{r+h}{d} \tag{2.4}$$

$$d^2 + (h-r)^2 = r^2, \quad r = \frac{d^2 + h^2}{2h} \tag{2.5}$$

$$\tan \varphi = \frac{d^2 + 3h^2}{2hd}, \quad \theta = \pi - \arctan \frac{d^2 + 3h^2}{2hd} \tag{2.6}$$

However, this geometrical model is based on a truncated spherical shape of the droplet, which neglects gravity, and the contact angle hysteresis. In fact, the droplet will be a truncated sphere when the bonding number is small enough (Baratian et al., 2015).

17

Figure 2.5 shows varying contact angles between a droplet of water and different surfaces. An actuation voltage of 500 V at 18 kHz was previously reported when using Rain-X [6]. But, in our experiments, the lowest actuation voltage is around 200 V at DC to 1 kHz. This may be attributed to the hydrophobic oil applied to the surface. The peanut oil coated surface can increase the contact angle to 98˚, Fig. 2.5d.
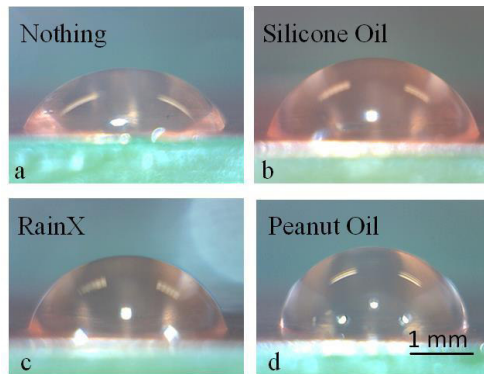
Fig. 2.5 Differences in contact angles of pure water droplet on different coated Saran Wrap surfaces. No voltages applied. a. Nothing coated on the Saran Wrap; b. With silicone oil coated on the Saran Wrap. c. With RainX coated on the Saran Wrap. d. With Peanut Oil coated on the Saran Wrap.

2.1.3 Results

Ideally, the droplet's contact angle is large with no voltage applied and becomes small with the application of a voltage (electric field). When this occurs the droplet can be moved quickly from one position to another. The contact angles of pure water droplets were compared on four different surfaces, Fig. 2.6. The surface coated with peanut oil, Fig. 2.5d, shows the largest contact angle with no applied electric field.
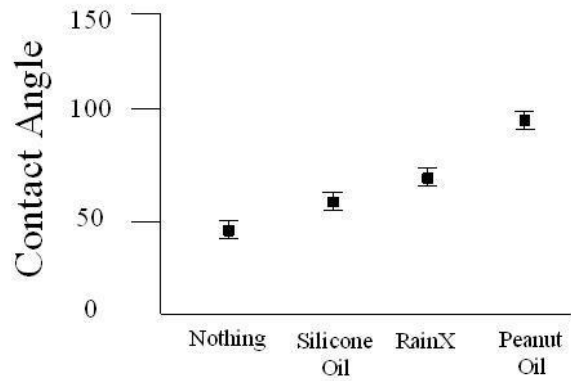
Fig. 2.6 Diagram of the average contact angles of the four surfaces, and standard deviations (SD) of the contact angle of different surfaces

The contact angle is more sensitive to changes in voltages than changes in frequencies, Fig. 2.7 and Fig. 2.8. The Young-Lippmann equation in the following shows the voltage related contact angles changes, but doesn't include the hysteresis in the real world.

However, for a sessile water droplet, the droplet-substrate contact angle varies with the electrowetting number (η):

$$cos\theta = cos\theta_Y + \frac{\varepsilon_0 \varepsilon_d}{2d\sigma_{lv}} U^2 = cos\theta_Y + \eta \tag{2.7}$$

in which θ_Y is Young's equilibrium contact angle, ε_d is the dielectric constant of the insulation layer, d is the thickness of the insulation layer, σ_{lv} is the liquid-vapor surface tension, U is the applied voltage.

19
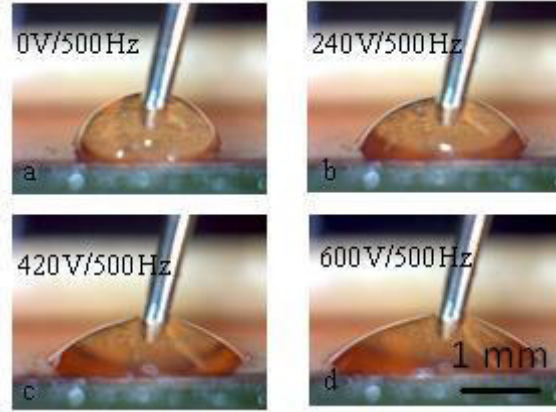
Fig. 2.7 On a peanut oil coated surface, measuring the contact angle change with voltages. Voltages are supplied at the surface. The stainless steel needle penetrating the droplet is grounded.

The actuation (threshold) voltage (at 500 Hz) to move the droplet in single-plate platform is much smaller than in the dual-plate platform. In the dual plate platform, the grounded electrode (the top ITO glass) is less conductive than metal, and the dielectric layer (Saran Wrap) is too thick (15 µm).
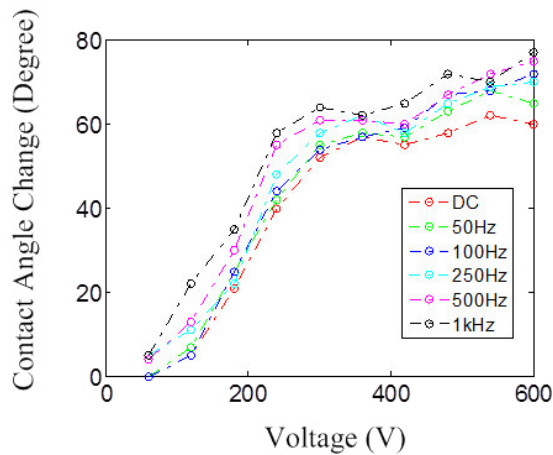
Fig. 2.8 Contact angle change with frequencies and voltages again using a pure water droplet on peanut oil surface.

The contact angle changes get saturated when the voltage is larger than 300 V. Driving voltages with higher frequencies lead to larger contact angle changes because the contact angle hysteresis is smaller in higher frequencies and the resistive force caused by the hysteresis is smaller.
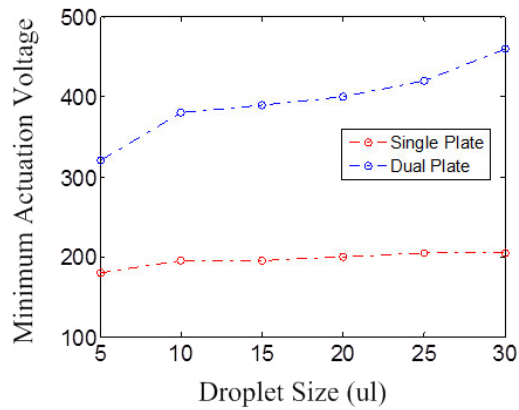
Fig. 2.9 Minimum actuation voltage at 500 Hz in single-plate and dual-plate platforms.

The driving voltage of using the dual-plate system is much larger than using the single-plate system (Fig. 2.9). The dual plate system has an extra top plate which introduces more frictions. Figures 2.10 and Fig. 2.11 show actuation, merging, and splitting (respectively) of coffee droplets on both the single-plate (a) and the dual-plate platforms (b).
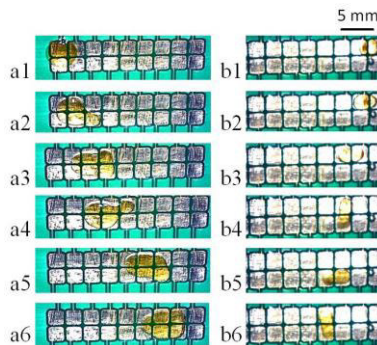
Fig. 2.10 Actuation of coffee droplets in single plate platform (a1-a6), and dual plate platform (b1-b6).
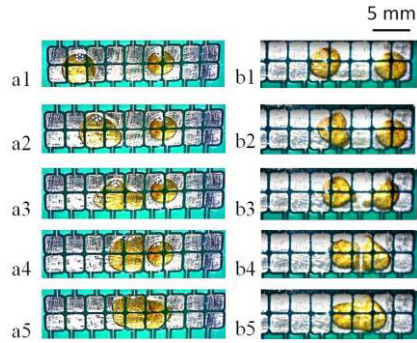
Fig. 2.11 Merge of coffee droplets in single plate platform (a1-a5), and dual plate platform (b1-b5).

2.1.4 Conclusion

A platform for the manipulation of droplets has been developed and characterized. In the dual-plate design the size of the droplet is more flexible. The droplet can be scaled down to the same size as the electrode. In the single-plate design the droplet should be no smaller than 2 electrodes (4 mm when a 2 mm electrode is used) to ensure reliable movement. The droplet size is one limitation of the standard PCB prototyping. When designing the PCB board, the gap between the electrodes should be no less than 75 μm, so it is hard to make intersectional electrodes which will ease the movements of smaller droplets. A razor blade can be used to create the gap between electrodes as described in other studies (Abdelgawad & Wheeler, 2007; Abdelgawad & Wheeler, 2008; Abdelgawad & Wheeler, 2009). Even with these shortcomings, this technique is still attractive for neurological experiments due to the absence of mechanical components and the resulting reduction in damage to the tissue being tested.

The single-plate electro-wetting platform developed in this study can move 30 μL (5-6 mm in diameter) droplets with an actuation AC voltage of around 200 V. Prototyping this microfluidic system is fast and efficient requiring no clean room facilities or special

semiconductor-fabrication related skills. This technique can be a good candidate for assisting neurologists in the reliable and efficient batch processing of immunochemistry and H&E (Y. Li, Tian, Qian, Yu, & Jiang, 2011) staining of rats' brain sections.

Future work will investigate how electrode geometry and the size of the gaps between the electrodes influence the actuation voltages. Further, scaling to smaller geometries, perhaps using integrated circuit (IC) technology, will be explored. The use of the thinner dielectrics in ICs under the electrodes, for example, should result in smaller actuation voltages.

2.2 Volume and concentration identification by using an electrowetting on dielectric device

2.2.1 Introduction

EWOD can be used to improve the throughput and the reliability of biological experiments. Small liquid droplet can be created, actuated, merged and split on a EWOD platform, so the small chemical droplet preparation can be controlled electrically instead of manually. Efforts have been taken to make electrical portion of the EWOD system more automated and intelligent. For example, a fuzzy PID control system was used to optimize droplet actuation in (Gao et al., 2013). A real-time feedback control circuit was applied for volume-dependent droplet creation in (Gong, 2008). Droplet composition and volume status monitor was employed for high efficient droplet mixing in (Schertzer et al., 2010). In (Basu, 2013), a morphometry and velocimetry measuring system was proposed for droplet tracking. The most important part of any intelligent feedback system is the front sensing component. The accuracy and reliability of the sensed signal dominate the judgment of the backend digital signal processing system. The capacitive sensor should be sensitive to the droplet parameters, including the droplet volume, composition and position. Capacitance is one of the most sensitive parameters to subtle droplet volume and composition changes.

The droplet introduced variations in capacitance has been used to measure the speed of the droplet movement (Elbuken, Glawdel, Chan, & Ren, 2011), to identify the composition of the dynamic droplets and to estimate the position of the droplet on the EWOD platform (Murran & Najjaran, 2012b). Most of the previous capacitance measurement techniques are based on a simple oscillator circuit (Ren et al., 2004) or a bench capacitance meter (Murran & Najjaran, 2012b; Schertzer et al., 2010; Schertzer, Ben Mrad, & Sullivan, 2012), which suffer from low resolution, low throughput and incompatible interfaces to an external digital system. In this study, an ultra-high resolution (24-bit) commercial IC (Integrated Circuit) is used to identify the volume and concentration variations of a droplet on a printed circuit board (PCB) based EWOD platform (Y. Li, Chen, & Baker, 2014). The results presented in this paper are useful for further studies of using a commercial IC CDC for intelligent control of specific biological animal tissue staining experiments.

2.2.2 Materials and methods

The capacitive sensor is fabricated using a standard double-sided PCB process. The electrodes are 2.3 mm × 2.3 mm square bare copper spaced 0.3 mm apart as seen in Fig. 2.12. A plastic layer (15 µm thick Saran Wrap) is used as the dielectric layer for the electro-wetting device. In the dual-plate configuration, the probes are connected between the top and the bottom electrodes. Single-plate EWOD is used in this study because it is easier to add and remove liquid between the electrodes (access is available, unimpeded, directly above the electrodes). The capacitance-resistance models of the single-plate and dual-plate systems are shown in Fig. 2.13.

A high resolution capacitance-to-digital converter (CDC) (AD7745, Analog Device, Inc., MA, USA) is used for the front-end capacitance measurement. The AD7745 has a resolution of 24-bits. Without using an extension circuit (in the CDC Block) shown in Fig. 2.14, the CDC's

measurement range is 4 pF. The measurement range can be extended to 48 pF if the extension circuit is applied. (The extension circuit includes the op-amp. Additonal details can be found in the AD7745's datasheet). AD7745 has a delta-sigma ADC to convert the analog capacitance data to digital signals, and communicate with microcontrollers through I2C serial port. The digital data is stored in three 8-bit registers before transmitting to the outside world by the I2C serial port. A 16-bit, 80-pin micro-controller (PIC24f96J, Microchip, USA) is used to receive the capacitance data from the CDC and forward to an LCD monitor for display. At the same time the same capacitance data package is sent to a PC through a UART serial communication port for a real-time display.
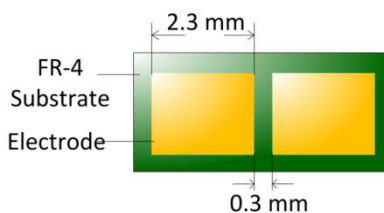
Fig. 2.12 Single-plate EWOD capacitance sensor.

The capacitances of pure water and NaCl solutions were tested on the EWOD platform. The capacitance of the droplet is volume and concentration dependent. A 0.5 μL (the pippette has a dispensing range of 0.5 μL to 10 μL in steps of 0.1 μL) droplet is added directly on the top of the two electrodes. Only the first 10 measurements were recorded since the small droplet will evaporate in 5 minutes. When varying the volume of the droplet an additional 0.5 μL droplet was added vertically to the center of the droplet by a pippette. The reason we keep the same direction and angle when adding the droplet is that the sensor is very sensitive. Adding the droplet from different angles will cause the droplet to change shapes resulting in tens of femto Farads' variation in the measured capacitance.
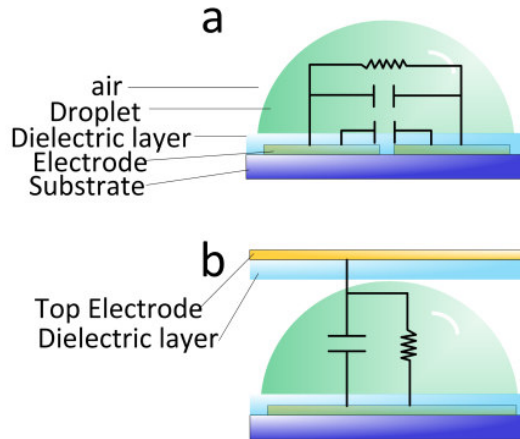
Fig. 2.13 (a) Single-plate and (b) dual-plate configuration.

To test the capacitance of various NaCl concentration on the EWOD platform, droplets of the same volume but different concentration are added and removed from the electrodes. Because the position deviation will cause errors when depositing the droplets manually, a fixed position for the droplet in each measurement is required. A microscope is used to fix the droplet position in this measurement (Fig. 2.15). Digital Microscope Suite 2.0 (a real-time video capture software, Celestron, LLC.) is used to show the real-time video on a PC. Desktop drawing software, Epic Pen, is used to draw the contours of the droplets directly on the captured video. The standard contour is created when the first droplet is deposited onto the electrode as seen in Fig. 2.15. The red contour will stay on the screen while the video continues to operate in real-time. This ensures that the following droplets are in the same position. Droplets with different concentrations are then fit into the contour before reading the measurement value.

26
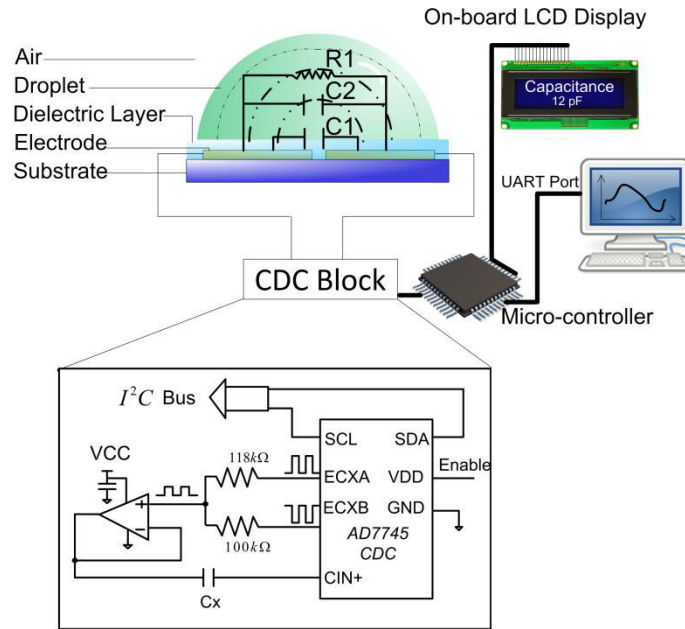
Fig. 2.14 Diagram of the CDC system

The PCB-based EWOD substrate has 9 electrode pairs. But in this study, only the first electrode pair is used for the capacitance measurement. The other electrodes are used for actuating, merging and spliting the droplets by applying a modulating high-voltage signal.

2.2.3 Results

As seen in Fig. 2.16 the capacitance changes dramatically with the volume of the droplet. The change in capacitance slows down when the droplet is larger than 3.5 μL. The electrode pair starts to be totally covered when the droplet is larger than 3.5 μL. Without a varying covered area, only the droplet's volume is affecting the capacitance. With a fixed position, the CDC sensor can resolve capacitance changes by 0.1 μL variation in volume (Fig. 16, see the small embedded illustration).
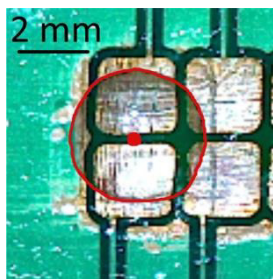
Fig. 2.15 A capture of the EWOD electrodes and a 3.5 µL droplet bridges the electrode pair. The droplet is marked by a red contour in the figure. When the contour is created, the following droplets should be fit in to the contour frame to ensure an unchanged droplet position.

As can be seen in Fig. 2.1 pure water has a larger dielectric constant than saline solutions, so the saline solution droplet has a lower capacitance than the water droplet. The deviations of the droplet capacitance measurement is small (around 10 fF, reduced by almost 10 times by using Epic Pen to fix the position and the shape of the droplets).
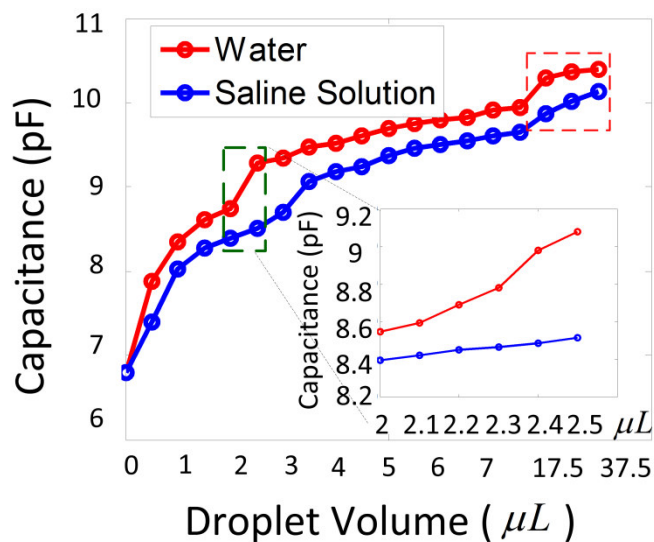
Fig. 2.16 Comparison of the capacitances with various droplet volumes (0.5 µL in step). The green dashed square marks the selected volume range, 2 µL – 2.5 µL, for a 0.1 µL (minimum unit of the pipette) step measurement. The data marked by a red dashed square in the right corner

28

is obtained by 17.5 μL, 27.5 and 37.5 μL. The rest of the data are from 0 μL to 7.5 μL, with a step of 0.5 μL.

A 1% concentration step is selected for the capacitance versus droplet concentration experiment, Fig. 2.17. The deviation of the measurement is about 10 fF. The CDC cannot resolve concentration changes smaller than 1%. The dielectric constant decreases when there are more ions dissociated, so as shown in Fig. 2.17, the capacitance decreases when the concentration increases.
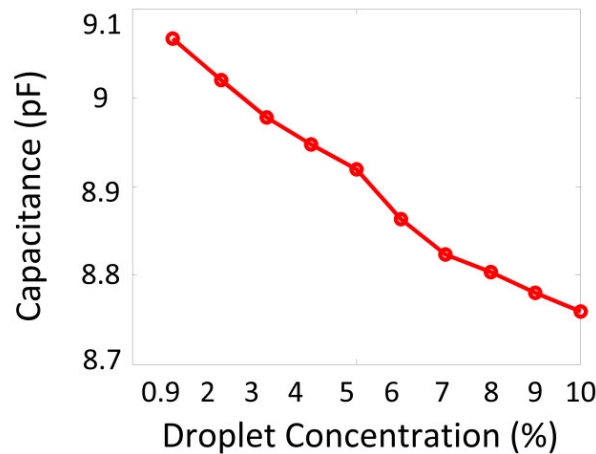
Fig. 2.17 Capacitance changes with different NaCl concentrations.

2.2.4 Conclusion

A commercial high resolution CDC is used in an EWOD device for capacitance measurement. The applications of using high resolution capacitance sensor in microfluidics are numerous. For example, controlling the droplet creation and merging in an EWOD system (Gong, 2008; Schertzer et al., 2010) and detecting the droplet position for an EWOD-based H&E (Y. Li et al., 2011) or immuno-histochemistry staining experiments.

The CDC used in this system is an all-in-one IC. Digital data can be directly read out from the I2C communication port by a microcontroller and a PC. By using the extension circuit (Fig. 2.14, CDC block), the measurement range can reach 48 pF. The theoretical resolution of the CDC is 4 fF. In the real measurement, the CDC system can resolve 0.1 μL changes in volume and 1% changes in concentration. If the position of the droplet is fixed, the capacitance deviation is around 10 fF.

A PCB-based EWOD device has several advantages over the platforms fabricated in a clean room. It has a lower cost and it can provide a fast fabricating technique for biologists who do not have clean room facilities. A larger EWOD array with distributed CDC sensors can be used to create a high throughput, intelligent microfluidic system. The capacitance sensor proposed in this study can improve the automation of some specific biological experiments. The data presented in this study may be an important reference for further studies towards the automation of animal tissue staining experiments.

2.3 A PCB substrate single-plate electrowetting actuator with embedded capacitive position detector

2.3.1 Introduction

Electrode capacitance is sensitive to droplet size, composition, velocity and position. Studies using capacitive sensors to identify the droplet's parameters are showing reliable performances by detecting the capacitance changes (Murran & Najjaran, 2012b; Ren & Fair, 2002; Ren et al., 2004; Schertzer et al., 2010). Using conventional bench single-channel capacitance meters (which are large in size) (Murran & Najjaran, 2012b; Schertzer et al., 2010) is good for testing the capacitance of a single electrode pair, but they suffer from several limitations, such as low resolution, uncontrollable outputs, physical size, and a mono-channel output. With the advances

in integrated circuit (IC) design, capacitance data can be directly read out of a serial communication port from an all-in-one IC preforming a capacitance-to-digital conversion (CDC). For example, the AD7745 (Analog Devices, Inc., MA, USA) is a high-resolution (24-bit) CDC with a measurement range from a couple of picofarads (pF) to 48 pF. The resolution of the sensor goes down to ±4 femtofarads (fF). High-reliability and stability were reported in a 24-hour period monitoring the humidity, temperature, and capacitance of a sensor system (Avramov-Zamurovic & Lee, 2009). The potential applications of this high-resolution CDC IC chip is numerous, no studies have used it for droplet position detection in microfluidic systems. In the research presented here a 2×8 sensor array is used in a droplet position detection system. A CDC is used to scan the electrode pairs in the array to monitor the capacitance changes. These data are then used to reconstruct the experiment's operation and generate animations which are viewed on a PC. This droplet monitoring method, "capacitive vision," is an alternative to traditional optical imaging which, as already mentioned, has limitations in some optic-phobic experiments such as Quantitative PCR (qPCR).

MATLAB 3D Animation is used to process the received data and reconstruct the droplet environment on a PC. The data is obtained by a multipoint control unit, MCU, from the sensor array. The data is then immediately transferred to a PC for monitoring. The computer then monitors if the droplet was issued as expected or if the droplet is being actuated toward a correct direction. This technique improves the automation of the microfluidic system in immunohistochemistry experiments and thereby reduces the cost associated with human monitoring. Further, the physical size of the system is much smaller than a bench capacitance meter as reported before (Murran & Najjaran, 2012b).

2.3.2 Materials and methods

The fabrication and design of the PCB digital microfluidic substrate is introduced in 2.1.2. The gates of the MOSFETs are connected to the I/O ports of the microcontroller. A high-voltage square wave is created at the drains of the MOSFETs in Fig. 2.18. For example, if the gate voltage goes high then the drain voltage goes low. If the gate voltage goes low then the drain voltage is pulled to the "High Voltage" through the resistor.

Fig. 2.18 System-level design of the droplet position monitor.

The electrodes are made using bare copper rectangles on the top of the PCB. A plastic sheet (Saran Wrap, 15 μm thick polyethylene) is cut in suitable size and coated on the top of the electrodes. Single-plate operation is much easier to be mounted than a dual-plate operation. In the single-plate device, the droplet bridges two electrodes, which has one activated with alternative pulses and another one grounded. In the dual-plate device, all the bottom plates is activated with alternative voltages, the top plate is an ITO glass which is grounded. The experimental results presented here use single-plate operation.

The MOSFETs in Fig. 2.18 are used for controlling the high-voltage signals connected to the electrode array. The red circular dots indicate the connection to corresponding electrodes on the PCB substrate. Their gates are interfaced with separate regular I/O ports of the MCU. When the gate voltage is 'high', the electrode voltage is shorted to 0V; when the gate voltage is 'low', there is no current flow through the MOSFETs, and the voltage at the electrode is the high-voltage. High-voltage pulses are controlled by changing the gate voltages.

Since a high-voltage is connected to the electrodes, and the electrode is directly connected to the CDC probes, relays are needed to isolate the CDC probes from the electrodes (a high-voltage can't be applied directly to the CDC). When the high-voltage is applied the relay is turned off isolating the CDC probes from the high-voltage. When there is no high-voltage applied the relay is on and the sensor is able to sense the capacitance of the electrodes. The 470 pF capacitors are serially connected between the electrode pairs to reduce the total capacitance in the circuit so that the input range falls into the measurement range of the CDC sensor. At the same time the reduction in capacitance enables the circuit to operate at the 1 kHz pulse rate.

The AD7745 does not have a specific address for each individual product. This means that if all of the CDCs are attached to the same I2C bus the computer will not know where the received data comes from. An address counter is used in the FPGA to select the specific CDC via an enable signal from FPGA. The FPGA will send the address information for a CDC to the MCU at the same time (in the same loop). Then the MCU can collect the data from I2C and the address information from the FPGA at the same time. After a short post process of the data inside the MCU, the data is displayed in real time. Fig. 2.19 shows a representation of the system.
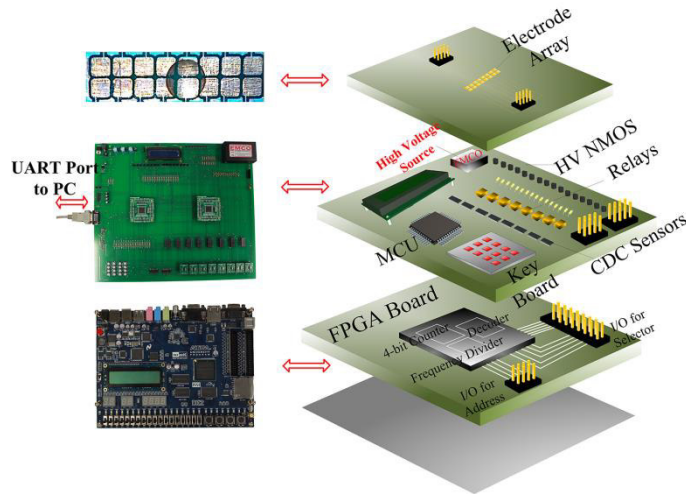
Fig. 2.19. Representation of the capacitance sensor system architecture. The bottom level is the FPGA logic controlling level. The FPGA is used to implement the main logic functions of the system. The second level is the central processing module. The high-voltage supply, microfluidic controller, LCD display, control keypad, CDC chip array and PIC24F microcontroller are all integrated on this middle level which makes the system more portable. The PIC24F has I2C serial communication module which receives the digital capacitive data from the CDC chips. The UART port transmits the received data to a PC for display. The microfluidic electrode array is seen on the top, or third level.

Note that there is no enable pin designed for AD7745 so the power pin is used instead. The problem with using this method is that when the chip is powered up the data placed on the I2C data bus is not meaningful so this data must be discarded. From the time the sensor is powered up to the time that the first valid data is available is, approximately, 150 ms. If the size of the array is large the time spent on scanning over all the electrodes will be long and probably make the system fail to detect the position and the error on time.

Without the measurement extension circuit (Analog Devices,) applied the initial measurement range of the CDC is ±4 pF. Figure 2.20 shows a block diagram of the CDC. The

34

ECXA and ECXB signals seen in Fig. 2.20 coming from the sensor are equal and opposite (complements) so the differential signal (pulses in smaller amplitude) are generated at the non-invert input of the op-amp seen in Fig. 2.20. Note that Cx, seen in Fig. 2.20, represents the capacitance between the electrode pair in the array.
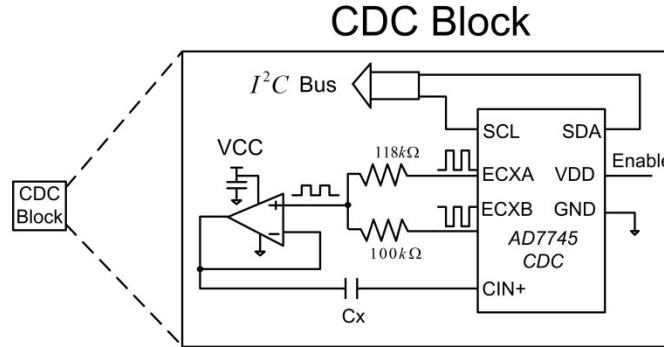
Fig. 2.20. A zoomed in view of the CDC block in Fig. 2.18. It consists of a CDC chip and a measuring range extension circuit (Analog Devices,).

The differential resistors are selected to calculate the range extension factor. For example, the designer would use 100 kOhm as resistor connected to ECXB in Fig. 2.20, and wants to get a capacitance measuring range extension to 48 pF. The resistor connected to ECXA should be R2, which is calculated as:

$$F = \left| \frac{R_1 + R_2}{R_1 - R_2} \right| = \left| \frac{100k\Omega + R_2}{100k\Omega - R_2} \right| = 12 \tag{2.8}$$

Solving, R2 = 118 kΩ. So the extended measurement range of the CDC is:

$$C_{DYN} = C_{original} \times F = 12 \times \pm 4\,pF \approx 48\,pF \tag{2.9}$$

Data appears on bus when either of the CDCs enabled. The UART baud rate is set as 9600 bit/s. The circuit was tested with baud rates from 9600 bit/s to 38400 bit/s. When the baud rate is greater than, or equal to 38400 bit/s, the transmission errors increased significantly. In this

system the conventional UART baud rate (9600 bit/s) works fine since the bottle neck in speed performance is the analog-to-digital converter inside the CDC. If the typical time spent on the data converter and readout circuit is 200 ms/byte in total, then the maximum speed for transmitting effective data stream is about 40 bit/s, which is far less than 9600 bit/s. So using the typical baud rate results in reliable communication.

Figure 2.21 shows the timing diagram of the system. The 8-bit enable pulses from FPGA are separated by a 100 ms delay to avoid the data collision. The electrode address is counted by an embedded counter in the FPGA, the MCU can collect the capacitance data and the corresponding electrode address at the same time.
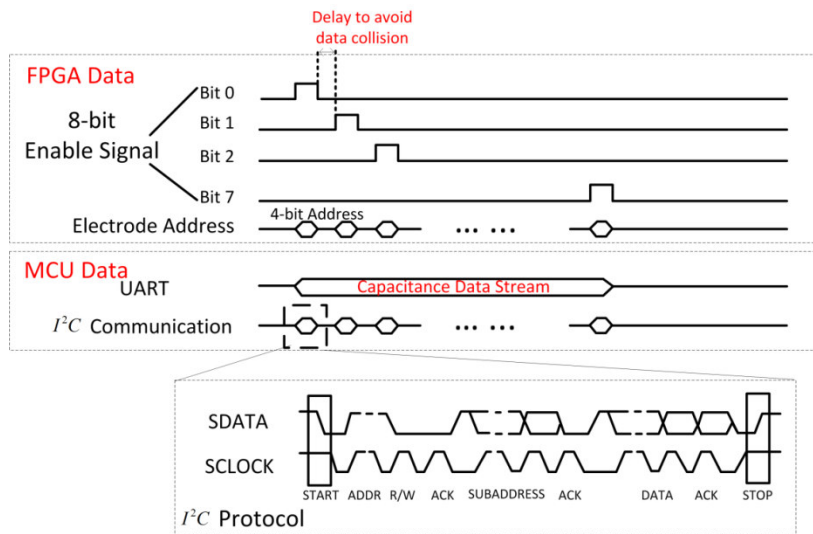
Fig. 2.21. The timing diagram of the logic module in FPGA, MCU and CDC chips.

The PIC24f96 is a 16-bit MCU, the capacitance data collected from the CDC sensor is in bytes. The resolution of the sensor is 24 bits, so all the capacitance data are stored in 3 individual 8-bit memory units. So every time the data are ready to be read, the MCU should re-process the 3 byte data into one 24 bit real capacitance value, and then transmit the data to the PC via UART port.

36

MATLAB has libraries for reading data from the UART serial port and plotting the data in real time. This software should be able to discard the error data and obtain the correct data from the data stream. There are two types of data appear on the I2C bus should be discarded. One is the over-ranged data (48 pF in our system) which is caused by the delay and the enable signal, another one is the messy data caused by the enable signal at VCC. The over-ranged data can occur at any time but corrupted data only occurs when the CDC chips are enabled (powered up). Figure 2.22 shows the software flow chart to filter out the over-ranged data and the corrupted data.
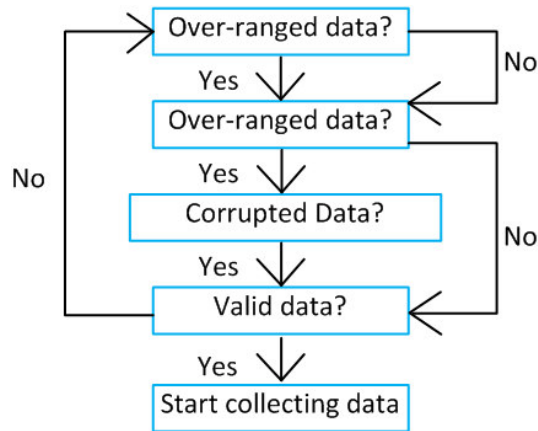
Fig. 2.22 Data filtering software flow chart.

The MATLAB plotting library can reconstruct the droplet with the updated position information received from the capacitance sensors. Because of this the UART at the receiving end doesn't need to be programmed. The MATLAB UART reading library is already set to read each byte. The only thing required is reconstruct the bytes into 24 bit real capacitance data again and store it in the matrix for analysis.

2.3.3. Results

The CDC sensor array is evaluated when the droplet is located at different positions. The capacitances cp1-cp8 in Fig. 2.23 represents the capacitance of the 8 electrode pairs. The different positions in Fig. 2.23 are numbered as 1-5, and the corresponding capacitance at 1-5 are shown in Fig. 2.24. Only cp1-cp3 are shown in Fig. 2.24 because the droplet position only has three statuses: fully occupied, half occupied, and 'off' the electrode. For example, in Fig. 2.24 (a) for cp1, position 1 is fully occupied, position 2 is half occupied, position 3 is 'off'. In this case cp1 has three statuses – 1 full occupied status, 1 half occupied status, and 1 'off' status. Then cp2 and cp3 have 1 full occupied status, and 2 half occupied statuses and 2 'off' statuses because the droplet can be half occupied at the left or at the right side of the electrode. The software can distinguish if the droplet is on the left or on the right by checking the address. This is why an FPGA is used, that is, to hold the address information.
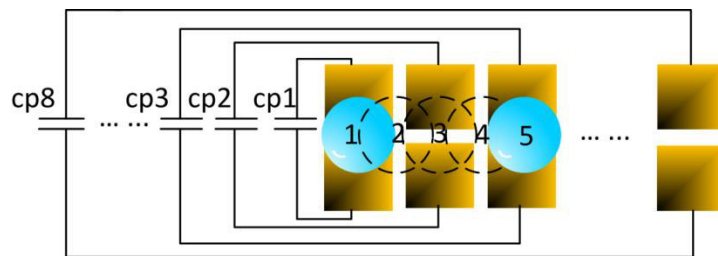
Fig. 2.23 Diagram of the capacitance of each electrode pair. The five droplets in this figure are specifically used to represent the five different positions of the droplets on the first three electrode pairs which help explain the parameters in Fig. 2.24.

In Fig. 2.24, when there is no droplet on the top ('off' status), the initial capacitance is varies from between the electrode pairs. This is because different transmission paths have different parasitic capacitances. Note that the initial capacitance should be measured in advance and stored in a matrix in the software as a baseline.
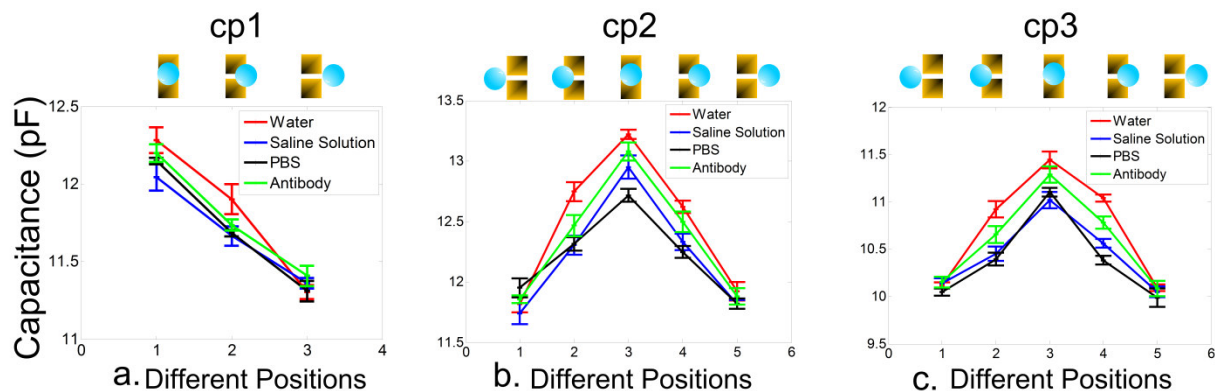
Fig. 2.24 Diagram of cp1 (a), cp2 (b) and cp3 (c) values at different positions. For example, cp1 has the greatest value when the droplet at position 1. The initial value of the capacitance of cp1 is around 11.3 pF which is obtained when the droplet is at position 3 (since there is no contact between the droplet and cp1 electrode). Biotinylated secondary antibody was bought from Zymed.

Note that the capacitance measured using a pure water droplet is higher than the capacitance of other types of droplets. The large dielectric constant of water means that ionic bonds of the solute will tend to dissociate in water yielding solutions containing ions. Water as a solvent opposes the ionic force between the ions. Water molecules have four hydrogen bonds and this structure of water greatly resists the random thermal motions. This hydrogen bonding is responsible for its large dielectric constant.
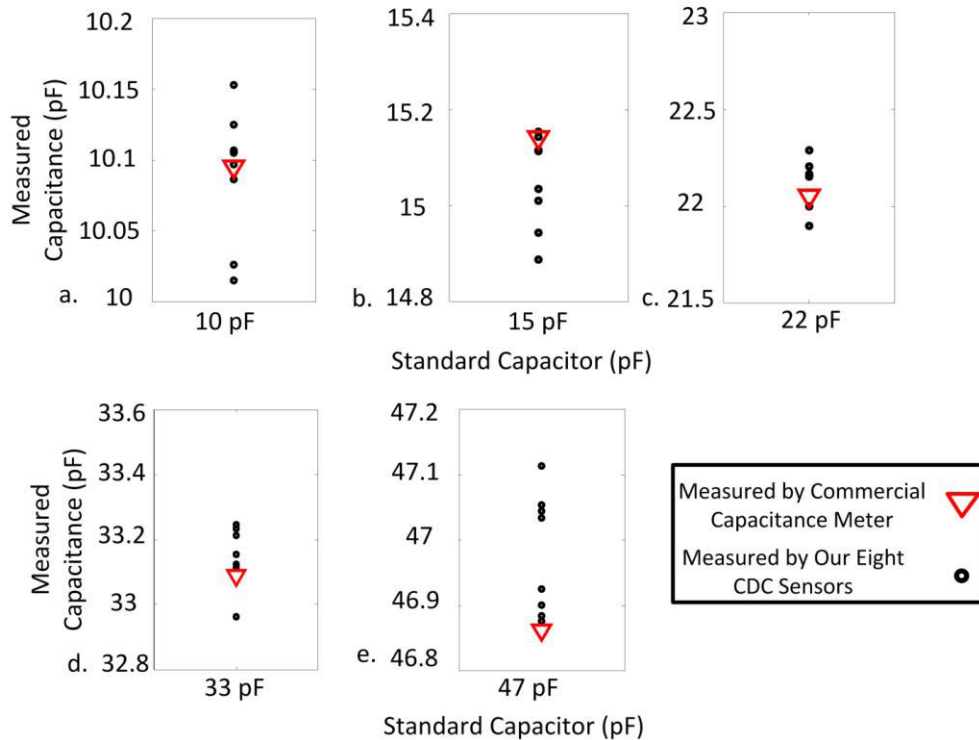
Fig. 2.25 Diagram of the capacitance of the standard ceramic capacitors measured by AD7745 and Bech LCR/ESR Meter (B&K Precision Corp, Yorba Linda, CA, USA). The Black dots represent the capacitance measured by the eight AD7745 CDCs in the array. The red triangle is the capacitance value measured by Bech LCR/ESR Meter, which is a commercially capacitive meter. The diagram shows the comparison of the measurements of standard ceramic capacitors with the values of (a) 10 pF, (b) 15 pF, (c) 22 pF, (d) 33 pF, (e) 47 pF.

There is a deviation of up to 200 fF between the CDC sensors when testing the same standard ceramic capacitor. This is large compared to the sensor's resolution (± 4 fF). The data seen in Fig. 2.25 was measured with circuits built with connection wires and bread boards. The CDC sensors are mounted on different SOIC-16 SMT adapters. Subtle parasitic capacitance changes are created by the differences of adapters and wires and the fabrication process of the CDC chip. In addition, the extension circuit and the approximation made in the microcontroller software adds

some additional variations to the results. However, these issues aren't a problem if the changes in the capacitances are sensed and not the absolute values of capacitance.

One may be concerned with the consistency of the CDC when it is measuring the same capacitor. Figure 2.26 shows the stability of one CDC sampling a standard ceramic capacitor. The deviations are small and negligible (around 10 fF). The deviation seen in Fig. 2.24 is in 200 fF range, but deviation when testing standard ceramic capacitors is much smaller. This is because the deviation of the droplet system may be caused by the subtle displacement of the droplet, undistinguishable with the naked eye (changes of hundreds of femtofarads may occur).
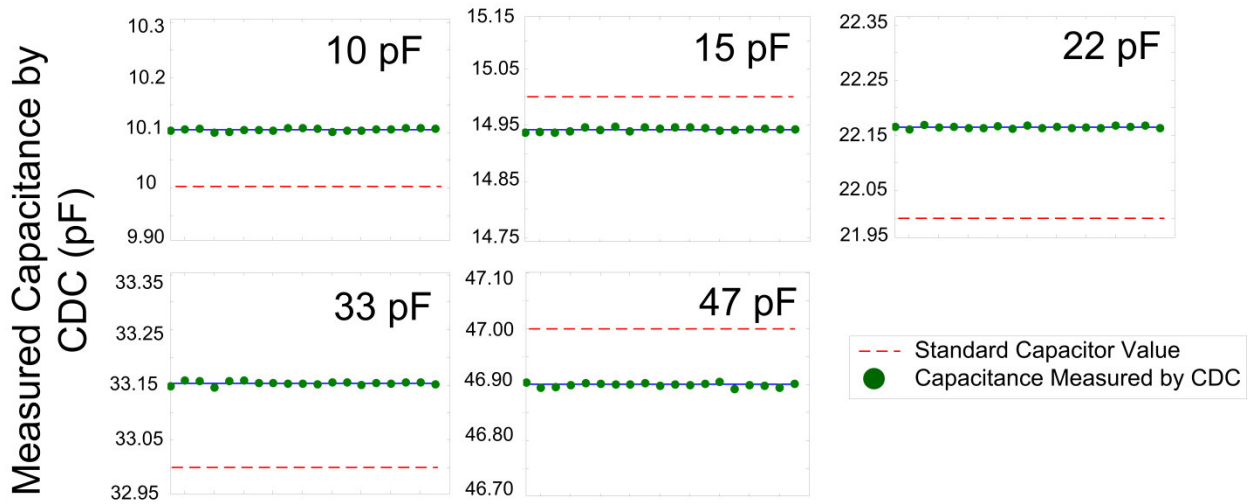
Fig. 2.26 Diagram of the evaluating one CDC with a standard ceramic capacitor. The value of the standard capacitor is marked by the red dashed line in the sub figures. The 20 samples measured by one CDC is marked with green dots, and the average value is plotted in the blue solid line go through the dots.

As shown in Fig. 2.27, the droplet sensing system can distinguish the three statuses (fully occupied, half occupied and 'off') for single droplet or multiple droplets. If the position of the droplets changed, then the software can update the position information in the matrix instantly,

and reflect the new positions in the animation. The capacitance data comes together with the electrode address to the MCU and then transmitted through the UART port to PC, so the computer will not make any mistake about the ownership of the capacitance data.
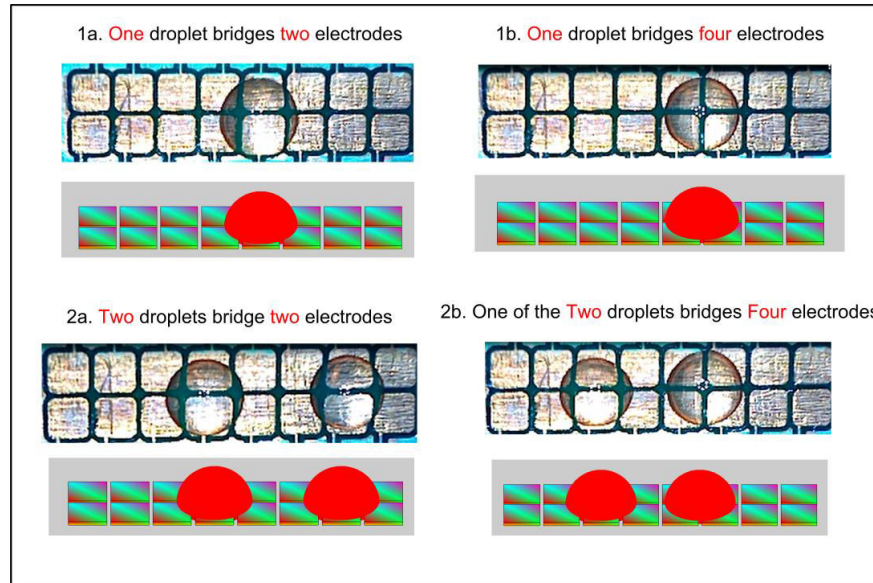
Fig. 2.27 Static droplet position detection in air environment for (1a) one droplet bridges two electrodes, (2a) two droplets bridges two electrodes, (1b) one droplet bridges four electrodes, (2b) one of the two droplets bridges four electrodes. The droplets are put on the electrode array by pipette. The system can detect if the electrode is fully occupied, half occupied or 'off' the electrode. Single-plate electro-wetting device is used in the system, which means the first row of electrode array shown in this figure is activated by alternative high-voltage pulses, the bottom row of the electrode array is grounded.

When the droplet is moving the system can update and reflect the position information dynamically (Fig. 2.28). An oil environment is preferred because the droplet will have a larger contact angle change with voltage pulses added to the corresponding electrode.
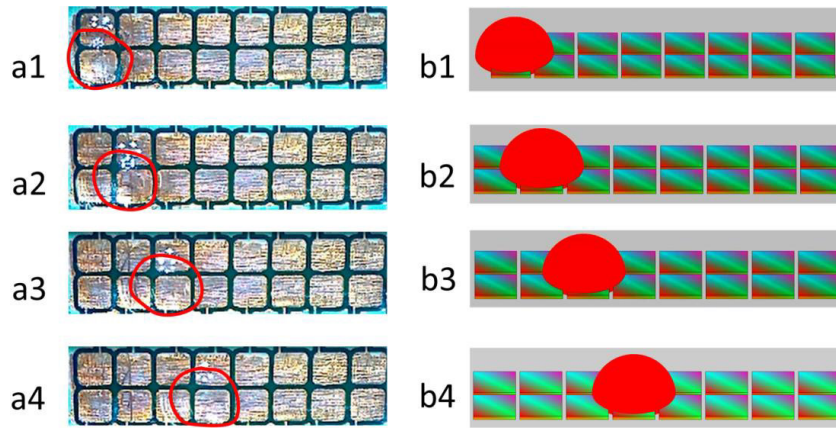
Fig. 2.28 Dynamical detection of the droplet position in oil environment. It is hard to see the transparent water droplet edges in an oil environment (droplets in Fig. 2.27 are moved in air) under the camera LED lights, so red contour of the droplet is added to a1-a4.

To the best of our knowledge, this is the first study using commercially capacitive IC chips to localize the droplets on the microfluidic chips ("capacitive vision"). The fast prototyping PCB-based microfluidic chips are easy to fabricate and customize. The post-processed PCB array presented here can move large droplets with a much smaller voltage and frequency than previously reported (Y. Li et al., 2014). This is important because if large droplets are actuated, very high-voltages above 600 V are no longer required. This is important since large voltages may break down the dielectric layer on the top of the electrode. Reduction in the actuation threshold voltage level at the same time increases the capability of actuating larger droplets, an essential part of the microfluidic device design. Another benefit of using the high-resolution CDCs is making the system have a capability of distinguishing additional droplet locations, more than presented in this study (Fig. 2.23) such as '1/3 occupied' or '1/4 occupied' statuses. The 1/3 and 1/4 statuses are not counted in our system since the capacitance changes between half occupied and 1/3 occupied are too subtle. This makes it difficult to distinguish deviations of the capacitance caused by the environment. However, the high-resolution CDC has another potential

benefit, that is, to distinguish the droplet composition from several unknown droplets, or detect the volume of a specific droplet. Based on the results presented in our experiment, the capacitance differences between saline solution (0.9% NaCl) and pure water is around 100-150 fF.

When the droplets arrive at the specific electrode, it takes hundreds of mili-second, on average, for the sensors to scan over all the capacitance changes and then read out the data for the 3D animation reconstruction. The speed bottle neck of the whole process to locate the droplet is the analog-to-digital converting process inside the CDC. So if the capacitance becomes larger, the response time for the CDC will be even slower because of the longer charging time. This will be an issue if using a single MCU to scan over a large electrode array. Further study will focus on developing a distributed system that has more MCUs to avoid this bottle neck. Obviously, the time spent on using single MCU to scan the array is highly dependent on the size of the array. If the array is huge, then the time to scan over all the electrode pairs in the array will be long. If using a distributed MCU array which has the same number with the number of the CDCs in the circuit instead of just using one, the cost and the space will increase. On the other hand, a customized the ASIC capacitive sensors for the microfluidic system can further expedite the response time of the detection. The current CDC is transmitting data using I2C bus. There is only one wire responsible for transmitting the data, which is saving the I/O interface, but the transmitting rate is much slower than parallel communication. Also, the capacitance range of the electrodes is normally between 8 pF to 15 pF. The existence of the droplet will cause a capacitance change around 1 pF. The type of liquid in the immunohistochemistry staining experiment will cause a capacitance deviation of around 100 fF. The resolution of the ASIC

capacitive sensor does not have to be as high as 24 bits. Instead, only 10-12 bits resolution would be good enough for position detection.

Using AD7745 is far more flexible than the Bench LCR/ESR Meter and similar devices like bench meters (PXI-4072) as reported previously (Murran & Najjaran, 2012b). Digital output of the chip can be easily processed by microcontrollers and ASIC chips, and then processed and displayed by PC. The ASIC chip mentioned here is not the CMOS based hybrid sensors (Ghafar-Zadeh & Sawan, 2007; Ghafar-Zadeh & Sawan, 2008; Ghafar-Zadeh, Sawan, & Therriault, 2009), but an independent IC chip with digital readout I/Os.

The final purpose of this study is to investigate the capacitive sensing and position detection capability of our fast prototype microfluidic system for applications in rats' brain sections staining. Detection of the droplets position on the electrode array is the most critical part to make the experiment process electrically visible instead of optically visible to the computer. Batch process of hundreds of rat brain slides is very common in neuroscience experiments. Processing so many brain slides is repetitive and tedious work. However, it is a critical step in experimental data analysis. The neuroscientists may have performed experiments or drug testing with the rats for several months only to wait for the final process of collecting the data. Large deviations may occur if the staining processes fail because of manual operation. The brain sections are very easily cracked along the boundary of the cortex and the mesencephalon during this process due to the hard dragging and frequently movements by the metal handling instruments. In this presented study, the capacitive sensor based droplet position detection system is built on a fast prototype PCB microfluidic actuator as we reported before (Y. Li et al., 2014), if the wetting and staining process can be operated on the microfluidic chips, the tissue damage by hand handling and metal tweezers can be avoided. Neuroscientists can customize the electrode array size to

serve their specific experiment sample seize without using clean room facilities, which makes this technique promising. The reason it's important to actuate larger droplet is in TH+ immunohistochemistry staining experiment is the diameter of the TH+ cells area in rat's coronal section is around 500 μm, so the droplet should be large enough to cover and wet the tissue to ensure thorough chemical reactions within the cells.

Normally, electrowetting is implemented in an oil environment since the droplet in the oil has a much smaller contact angle hysteresis than that in an air environment. A larger contact angle change can then be obtained, which makes the droplet actuation easier. But if the microfluidic chip is used for immunohistochemistry staining experiment the oil environment is not acceptable because the concentration and ingredient of the liquids used in the staining experiment are strict and extra oil isn't acceptable. By using smaller electrodes (but high throughput) and a smaller gap size between the electrodes a decrease in the required voltage threshold for actuating the droplets is possible. This makes it easier to actuate the liquids without an oil environment. There are several studies directed at using an air environment to actuate the liquids by using smaller electrodes and more hydrophobic surfaces (Shih et al., 2012). If the contact angle of the droplet on the electrode is large enough in air then the oil environment can be avoided. Pumping and collecting the droplets are also required for the staining experiment. However, for disposing wasted liquid the electro-wetting devices need to be assembled with capillary pump as described before (H. Kim et al., 2013; H. Kim et al., 2011; Thaitrong et al., 2012). Microfluidic chips designed based upon the techniques present in this study, but assembled with capillary tubes, may have significant potential in animal tissue staining experiments.

2.3.5 Conclusion

The low cost, fast-prototype PCB based microfluidic system is developed and tested in this study. Lower threshold voltage to actuate large droplets is achieved by using a single-plate electrode array. The capacitance detection circuit can localize single or multiple droplets statically and dynamically, and display the position of the droplets on a PC in a 3D animation. Optimizations regarding improvements on the response time of the sensor for large electrode array, and assembling capillary tubes for immunohistochemistry experiments are expected in additional studies.

Chapter 3 Glass substrate digital microfluidics

In addition to PCB substrates EWOD DMF systems have been fabricated on paper (Fobel, Kirby, Ng, Farnood, & Wheeler, 2014), polyimide tape (Kirby & Wheeler, 2013), and glasse (Ng, Choi, Luoma, Robinson, & Wheeler, 2012; Ng, Chamberlain, Situ, Lee, & Wheeler, 2015). More interestingly, the driving electrodes can be non-metal materials. For example, regardless of the low breakdown voltage and the limited reliability, ITO (Shen, Fan, Kim, & Yao, 2014) and graphene (Tan, Zeng, Yi, & Cheng, 2013) can be directly patterned as EWOD electrodes on the DMF substrate. These alternative substrates can be a little bit more expensive than a PCB substrate but, at the same time, beating the PCB in the smaller surface roughness and the threshold actuation voltage. For the metallic electrodes on glass, an adhesion layer of Ti or Chromium should be used in between the top layer metal and the glass (Vancea, Reiss, Schneider, Bauer, & Hoffmann, 1989). The adhesion between Au and SiO2 is very poor, which will fail the lift-off process in the lithography. The Chromium nanoparticles are oxygen active which lead to very stable nucleation centers. Additionally, coating a thin film of Chromium prior to coating the Au layer can significantly inhibit the island growth and reduce the surface roughness (Vancea et al., 1989). However, in the EWOD application, the surface metal layer is just used as a conductive layer or actuator, if there is no particular sensing purpose for the electrode, a single layer of Chromium will be good enough for the actuation purpose. Therefore, a glass substrate, which is low-cost, with a 100 nm Chromium thin film coated on the glass, is used as the 2nd version EWOD substrate and employed for the DMF system design.

In this chapter, a Chromium coated EWOD DMF chip is introduced and tested to implement droplet actuation, merging and splitting in section 3.1; a dynamic top plate EWOD system is proposed to improve the performance in actuation velocity, dispensing volume control, reducing

threshold driving voltage, and decreasing the contact angle hysteresis are covered in sections 3.2-3.4.

3.1 A highly efficient and reliable electrowetting on dielectric device for point-of-care diagnostics

3.1.1 Introduction

DMF can manipulate a large array of droplets in parallel, which is critical for high throughput microfluidic experiments. With the advances in microelectronics, all DMF controlling and driving devices can fit into a portable box (Fobel, Fobel, & Wheeler, 2013). In DMF, one of the main physical and mechanical principles of moving a droplet on a surface is EWOD. EWOD describes a configuration in which an insulating layer separates the working liquid and actuation electrodes. PCB (printed circuit board) EWOD chips are low cost and easy to fabricate, but the driving voltage is high and oil environment is required for a smooth actuation. A reliable EWOD DMF chip with an 8 µm parylene C dielectric layer is proposed in this study (Fig. 3.1). Droplet dispensing, merging and splitting are tested under various droplet volumes. The droplet dispensing accuracy and splitting minimum voltages are discussed.

3.1.2 Materials and methods

Devices were fabricated in the cleanroom facility of Nevada Nanotechnology Center at University of Nevada, Las Vegas. The fabrication reagents includes Schott Boro Float glass substrate with Chrome coated (100 nm) microfluidic blank slides (with positive photoresist coated, Telic, Valencia, CA, USA), Teflon-AF solution (amorphous fluoroplastic resin in solution, 400S2-100-1, DuPont, Mississauga, ON, CA), photoresist developer RD6 (Futurrex, INC., Franklin, NJ, USA), Chromium etchant (Sigma-Aldrich, Co., MO, USA), photoresist

remover (Microposit Remover 1165, Rohm and Haas Electronic Materials LLC, MA, USA), indium tin oxide (ITO) coated glass (Adafruit INC., NYC, USA). Open source integrated circuit (IC) layout tools Electric VLSI (Http://Cmosedu.com/cmos1/electric/electric.htm.) is used to pattern the mask of the electrode array. GDSII output files from Electric VLSI are sent to Infinite Graphics INC. (MN, USA) for plotting (25,000 dpi). The top plate gap height is controlled by a PZT plate.
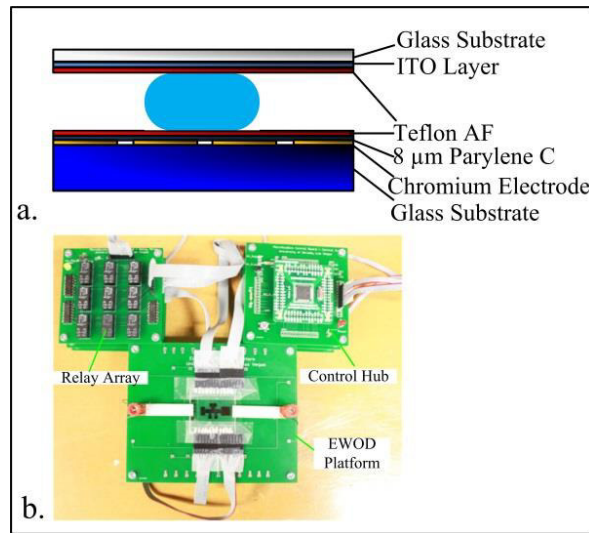
Fig. 3.1 The EWOD chip fabrication layers (a) and the EWOD system (b).

In order to make the surface more robust for higher voltages, an 8 µm parylene C is coated to the EWOD chip with a chemical adhesion process. The parylene C coating is conducted at Kisco Conformal Coating, LLC (San Jose, CA, USA). 250 nm Teflon AF is spin coated to the EWOD chip and the top plate surface. DI water droplets are used as the testing liquid for the experiments.

A high-voltage module (EMCO F40, EMCO, Schweiz, Switzerland) is used for the high voltage supply. A high-voltage square wave (1 kHz to 10 kHz) is created at the drain of the NMOS transistors (VN2460) seen below in Fig. 3.2. The gate is connected to the I/O ports of the

microcontroller. For example, if the gate goes high then the drain goes low. If the gate goes low then the drain is pulled to the high DC voltage through a resistor.
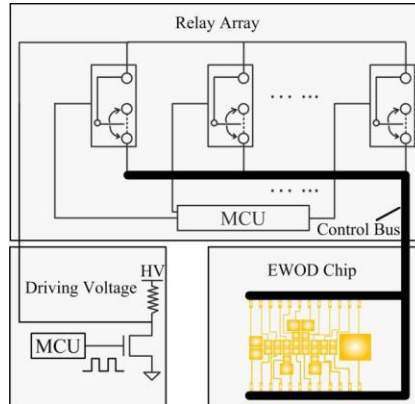
Fig. 3.2 The EWOD chip and the control system.

There are 27 electrodes on the EWOD chip, so 27 relays are needed as the switches for the electrodes. The high voltage pulses are connected to the input of the relay array. A MCU is used to turn on/off the electrodes; then the high voltage sources will be delivered or blocked by the relay. The other electrodes that do not need to be activated are floating (turned off the electrode by disconnecting the relay).

The driving pulse train of the two neighbor electrodes (Fig. 3.3) have an overlapping area. The receding electrode is still turned on for a while after the forwarding electrode has been turned on. The purpose is to keep the droplet in a big footprint area while the forwarding electrode is trying to drag it forward. If the droplet is moving slowly, then the overlapping area (in time) should be larger to wait for the droplet to travel through the receding electrode. Otherwise the droplet will miss the opportunity to be actuated by the forwarding electrode. The droplet velocity has big differences with different droplet volumes and different gap heights.
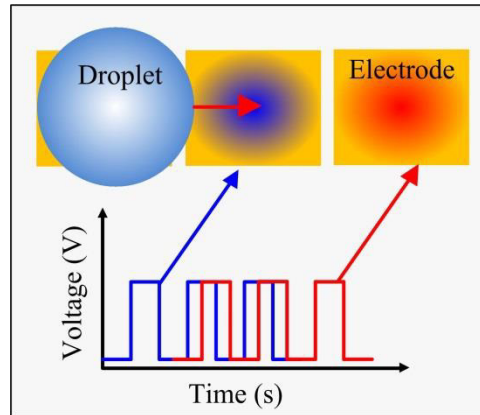
Fig. 3.3 EWOD electrode driving voltages. The DC pulses have an overlapping area for a more reliable actuation.

3.1.3 Results

Dispensing is the first step of the on-chip experiments. A smaller working droplet is generated from a larger electrode which is a reservoir of the chemical liquid. The forwarding electrode should be activated first to drag a certain amount of liquid from the reservoir. While the size of the generated droplet becomes close to the desired volume, the electrodes in the middle of the reservoir and the targeting electrode are turned off to disconnect the dispensed droplet from the reservoir (Fig. 3.4).
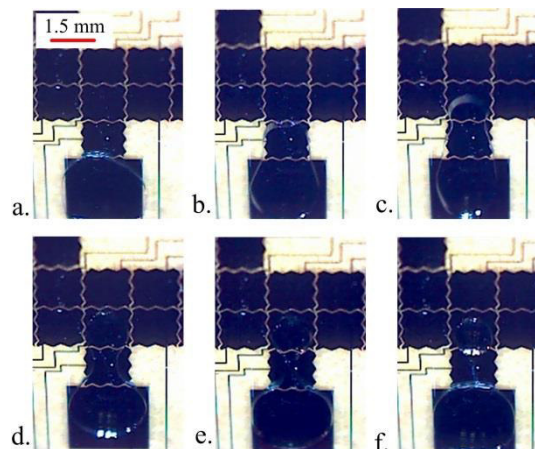
Fig. 3.4 The process of droplet dispensing from the reservoir.

The biggest issue with EWOD dispensing is the volume control. The dispensed droplet volume is hard to be controlled accurately. Adding capacitive sensors to a feedback control loop to manipulate the dispensed droplet volume in real time can improve the volume accuracy (Gong, 2008). But the droplet-electrode capacitive data is influenced by the droplet position substantially (Y. Li, Li, & Baker, 2014).

Dual electrode dispensing mode (DEDM) and single electrode dispensing mode (SEDM) are tested (Fig. 3.5 and 3.6). The droplet volume is calculated by multiplying the footprint area (calculated by ImageJ) by the gap height (200 µm). SEDM has a higher accuracy than DEDM. The standard deviations are 0.0467 µL for DEDM and 0.0303 µL for SEDM.
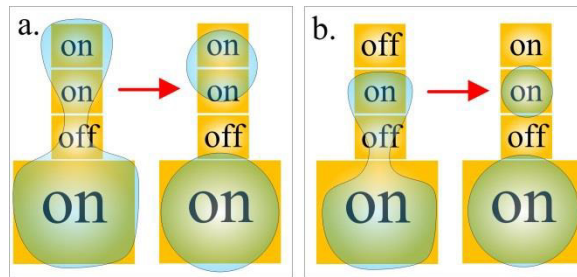
Fig. 3.5 Dual electrode dispensing mode (DEDM) (a) and single electrode dispensing mode (SEDM) (b).
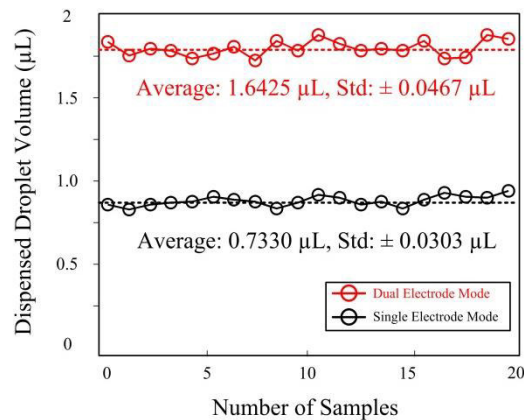
Fig. 3.6 Droplet dispensing accuracy.

Since the droplet volume affects the droplet actuation efficiency, when the dispensing is in process, the daughter droplets are much smaller than the reservoir. Varying the gap height (Yafia & Najjaran, 2013) can accommodate the optimized gap height of smaller droplets.

Mixing & merging two droplets are used for on-chip chemical reactions or dilutions. The purpose of on-chip mixing is to implement the conventional bench mixers used in biological labs. Mechanical shaking for a good chemical mix is not possible for the EWOD chip; so the merged droplets need to travel back and forth between two or three electrodes to insure the mix or reaction of the chemicals are completed. The droplet merging is fast, but the time spent on a sufficient mixing or reaction depends on the liquid types. Also gap height control and droplet movement control have been investigated for optimized mixing protocols (Paik, Pamula, & Fair, 2003; Yafia & Najjaran, 2013). It only takes less than 40 ms (after the droplets contacted with each other) to complete the droplet merging process in Fig. 3.7 and Fig. 3.8.
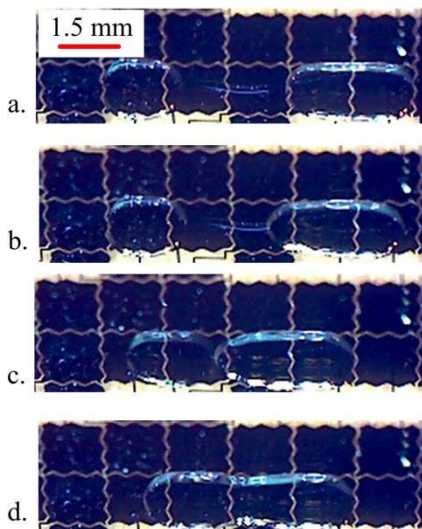
Fig. 3.7 Process of droplet merging.
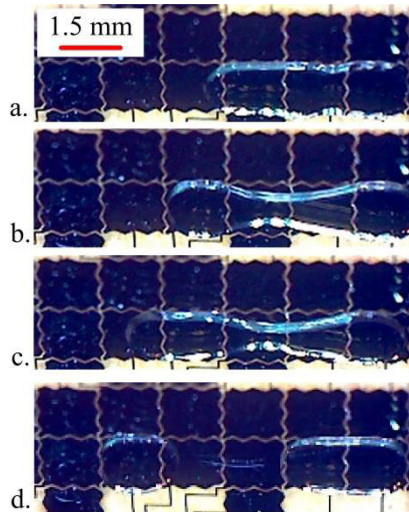
Fig. 3.8 Process of droplet splitting.

While doing the splitting experiment, the droplet is stretched by the electrodes at both the left and the right ends of the droplet. And then all the electrodes in the middle are turned off (Fig. 3.8). When the necking (Cho et al., 2003) appears, the droplet is further stretched resulting in two sister droplets. However there is one problem of open loop splitting. The electrodes at the two ends are competing against each other strength to drag the droplet to their side. When the activated electrodes are driven by the same voltage, the larger footprint area (the position) of the droplet will get more electrostatic force by the electrode underneath. In this case, unsymmetrical splitting may happen. So the success of splitting also depends on the initial position of the droplet. The same as dispensing, fast feedback capacitive sensing or an image processing controlled system may help balance the droplet position during the splitting experiment.

Larger droplets require larger splitting voltages. Splitting a 2.3 µL droplet needs 45 V more than splitting a 1.5 µL droplet (Fig. 3.9). The largest deviation on the minimum splitting voltage is 12.09 V occurs at the 1.5 µL droplet which shows a good repeatability of the tests.
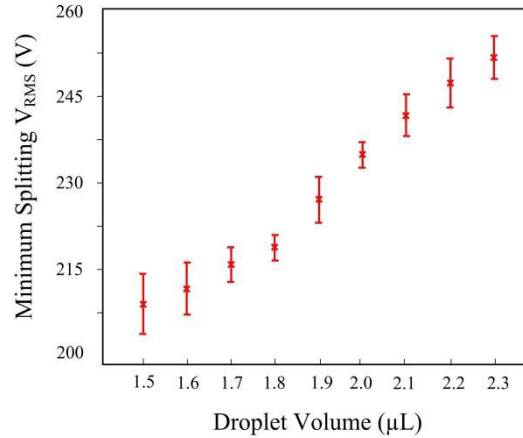
Fig. 3.9 Minimum splitting V_{RMS} for different sizes of droplets.

3.1.4 Conclusion

An efficient and reliable EWOD DMF chip is proposed in this study. During the dielectric layer coating process, extra vapor-phase silane (VPS) is introduced into the chamber and acts as an aerosol primer to enhance the chemical adhesion to the parylene C surface. The parylene C layer is robust and has a high break down voltage (more than 600 V). With the robust dielectric layer and the hydrophobic surface, all the droplet operations are conducted in an air ambient. Without using conventional oil filler, the EWOD chip is compatible with more chemical reactions.

The EWOD chip can perform droplet dispensing, merging and splitting. DEDM and SEDM are tested for the dispensing volume accuracy. Small deviations (0.0467 µL for DEDM and 0.0303 µL for SEDM) are observed using the dispensing operation with the EWOD chip. A lower desired droplet volume can be dispensed more accurately by the chip. Minimum splitting voltages are tested for various droplet volumes. Larger droplets require larger splitting voltages. Splitting a 2.3 µL droplet needs 45 V more than splitting a 1.5 µL droplet.

56

A simplified EWOD electrode driving circuit is introduced to avoid bench instrumentations. The proposed EWOD DMF chip is promising for future point-of-care clinical diagnostics.

3.2 Computer vision assisted measurement of the displacements of a bimorph piezoelectric cantilever beam

3.2.1 Introduction

A cantilever beam is a rigid structure which has only one end anchored and another end is used to support the load. Cantilever structures can be found in large size constructions (such as bridges, buildings and aircrafts) (Cruz, Mari, & Roca, 1998; Salawu & Williams, 1995) and small microelectromechanical systems (MEMS) (Beaulieu, Godin, Laroche, Tabard-Cossa, & Grütter, 2007; Kranz et al., 2001). Techniques used to measure the cantilever displacements (deflection) depend on the target dimension. Computer vision based displacement measurement techniques have been used for large cantilever structures (H. Choi, Cheung, Kim, & Ahn, 2011; Fukuda, Feng, Narita, Kaneko, & Tanaka, 2013; Ribeiro, Calçada, Ferreira, & Martins, 2014; Sładek et al., 2013). In these cases, the measurements are based on monitoring the displacements of the markers labelled on the structure by a digital camera. But for measuring the displacements of micro-structures, a higher resolution measurement technique is required.

Magnetic sensors can detect nanometer displacements (Curtis et al., 2013; Fleming & Leang, 2014). The magnetic sensor usually consists of a magnetic component and a sensor. The magnet portion has to be fixed onto the target object when doing the measurements. Small cantilever structures such as the STEMINC bimorph piezoelectric chip (PZT-5H) are not capable of holding the magnet part. Measuring the displacements of small cantilever structures therefore require non-contact measurement techniques. Ultrasonic and optical detection techniques can do

high resolution non-contact displacement measurements, but these approaches are expensive and hard to calibrate (Sun, Zhang, Liu, & Zhang, 2013; Vappou et al., 2015).

Recently, a computer vision based technique was used to measure small structure displacement (Qiu, Zhang, & Zhang, 2014). The measurement resolution is degraded by the low resolution camera and the limited image processing techniques. Using these techniques it is impossible to get good resolution when using big markers and regular cameras. To measure micrometer displacements a high resolution camera and a sharp micro-marker are required.

A new concept of PZT-5H displacement measurement is proposed in this study. By using a sharp micro structure as the marker, the PZT-5H displacements can be accurately represented by the number of pixels spanning the micro-marker. The voltage-to-displacement linearity and repeatability are reported in this paper. Potential applications of this technique are also discussed.

3.2.2 Materials and methods

The bimorph piezoelectric actuator (SM 311, PZT-5H) is purchased from Steiner & Martins, INC, which has a maximum actuation of 2 mm with a 200 Hz bandwidth. A regular laboratory power supply is used to trigger the high voltage module (EMCO F40, Schweiz, Switzerland) (Fig. 3.10).
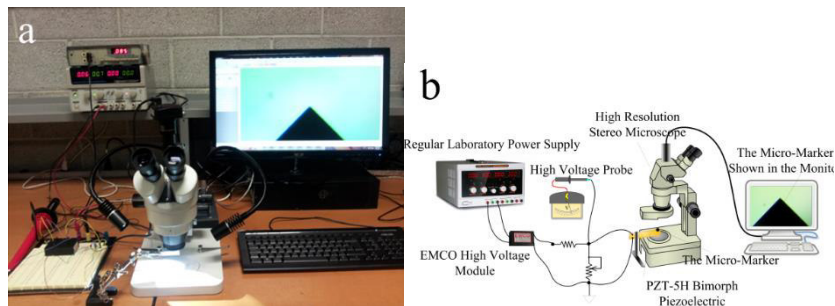
Fig. 3.10 (a) The PZT-5H displacement measurement system. (b) The diagram of the PZT-5H displacement measurement system.

EMCO F40 can provide DC voltages up to 2000 V. An adjustable resistor is used to modify the output voltages. A multimeter is used to monitor the voltage changes. A high resolution stereomicroscope (SM-1TSW2-L6W-10M, AmScope, CA, USA) (2748 × 3584 pixels) is used to track the micro-marker displacements. Microscopic captures are documented for every 2 V increase of the driving voltage applied to the PZT-5H chip.

A triangle shaped and Chromium prototyped structure (Fig. 3.11a) is fabricated using photolithography. Figure 3.11b shows the smallest black dot printed out by an HP Officejet Pro 8610 inkjet printer. The dot is invisible to the naked eye. Figures 3.11a and Fig. 3.11b are captured with the same microscopic magnification. The printed dot in Fig. 3.11b can be compared with the micro-marker shown in Fig. 3.11a. Compared to the micro-marker, the edges of the printed dot are rough. Clear and sharp edges are important for the vertex extraction in this study.
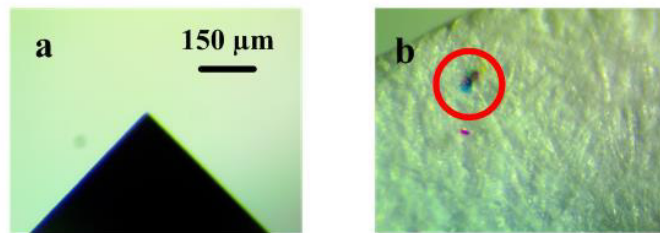
Fig. 3.11 a. The fabricated micro-marker with ×10 magnification. b. The smallest printable black dot (20 µm in diameter) printed by an inkjet printer on a regular paper (marked by a red circle. ×10 magnification). The mixed colors (RGB) of the printed black dot can be seen under microscope.

The use of photolithography can pattern a shape which is highly desired in this experiment. Since the fabricated edges of the triangle structure are clear and sharp, the vertices of the triangle

structure are easy to detect. The displacement of PZT-5H can be better reflected by the number of pixels spanning the vertex (Fig. 3.12).

The micro-marker used in this study is fabricated in the cleanroom facility of Nevada Nanotechnology Center at University of Nevada, Las Vegas. The fabrication reagents includes Schott Boro Float glass substrate with Chrome coated (100 nm) microfluidic blank slides (with positive photoresist coated, Telic, Valencia, CA, USA), photoresist developer RD6 (Futurrex, INC., Franklin, NJ, USA), Chromium etchant (Sigma-Aldrich, Co., MO, USA) and photoresist remover (Microposit Remover 1165, Rohm and Haas Electronic Materials LLC, MA, USA). Open source integrated circuit (IC) layout tools Electric VLSI is used to pattern the mask of the electrode array. GDSII output files from Electric VLSI were sent to Infinite Graphics INC. (MN, USA) for plotting (25,000 dpi resolution) on a plastic photolithography film.
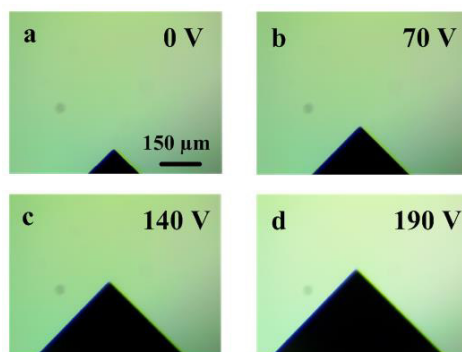
Fig. 3.12 The micro-marker spans over about 1029 pixels as the voltage applied to PZT-5H increased from 0 to 190V.

The substrates are covered by the patterned photomask and exposed to a UV light source for 45 seconds and then developed for 1 min in RD6. Substrates are then immersed in the Chromium etchant for about 15-20 seconds. Then the substrates are washed by DI water and dried out using nitrogen gas. The remaining photoresist is removed by Microposit Remover 1165. If the remover

doesn't remove all of the photoresist Kimwipes (Uline, WI, USA) (wetted by Microposit Remover or DI water) can be used to remove the remaining photoresist.

The glass substrate micro-markers are cut into 1 cm by 1 cm pieces and attached to PZT-5H with double sided tape as depicted in Fig. 3.13.
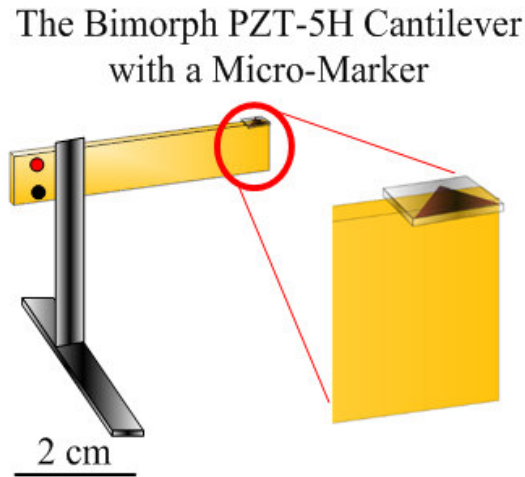
Fig. 3.13 The bimorph PZT-5H cantilever structure and the micro-marker.

The high resolution microscopic images are captured and saved. They are then converted to binary maps using MATLAB. The threshold for the MATKAB 'im2bw' function is 0.45. Due to the sharp edges of the micro-markers, the binary zoomed-in figures have clean edges as seen in Fig. 3.14. The zoomed-in binary maps are the vertices of the triangle shape. It is easy to locate the point (points) which has the largest Y axis values. The PZT-5H actuation is represented by the pixel value of the vertex of the triangle.
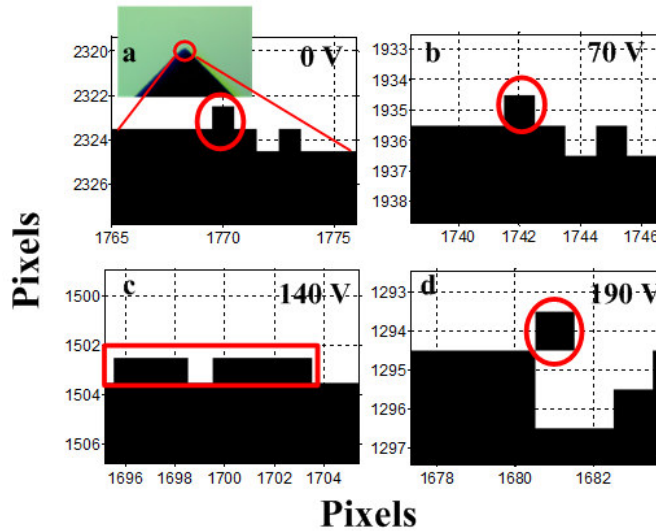
Fig. 3.14 The binary map of the vertex of the micro-marker. Each black square box is a pixel. The vertex pixels are marked with red circles in subfigures a, b and d. In subfigure c, there are 7 pixels (marked by a red box) have the same Y value.

As shown in Fig. 3.14, the vertex pixel value at 190 V is 1294 (Fig. 3.14d). The vertex pixel value at 0V is 2323 (Fig. 3.14a). The real distance between the two pixel values is approximately 300 µm. So the apparent size of each pixel is (2323-1294)/300 µm = 248 nm.
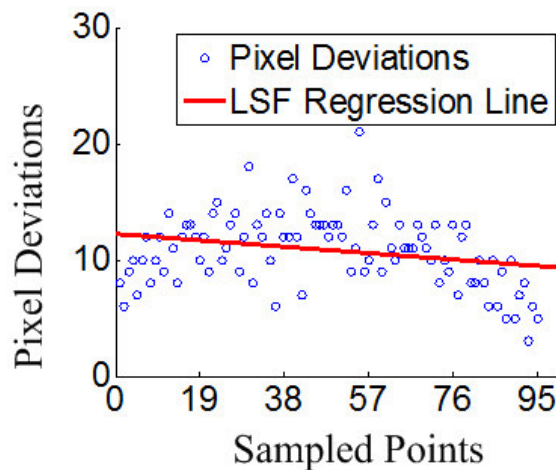
Fig. 3.15 Pixel deviations for every 2 V increase in the applied driving voltage.

PZT-5H driving voltages ranges from 0 to 190 V with an interval of 2 V. To reach 190 V, there are totally 95 samples in the experiment. The pixel deviations are shown as scattered values in this figure.

3.2.3 Results

By adjusting the voltage divider seen in Fig. 3.10, displacements for every 2 V increase in the voltage applied to the piezoelectric cantilever are recorded. The pixel deviations between every two neighboring input voltages are then plotted in Fig. 3.15. Within a certain range of input voltages, the micro-marker moves about 8-13 pixels for every 2 V increase in applied voltage potential.

The linearity of the PZT-5H is investigated by subtracting the pixel value at 0 V from the pixel values at other input voltages (see Fig. 3.16).
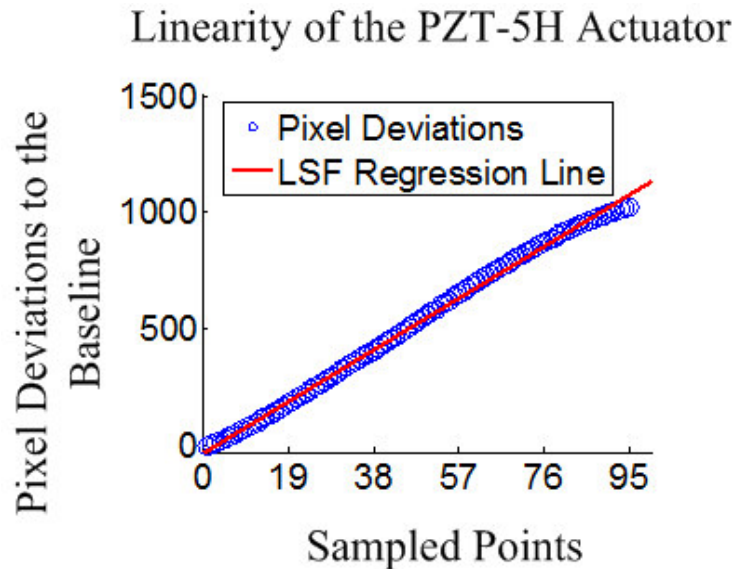
Fig. 3.16 Linearity of the pixel deviations at different input voltages.

Figure 3.17 shows the probability of the pixel deviations for each 2 V increase. The driving voltages ranges from 0 to 190 V, so there are totally 190 V / 2 V = 95 samples. For each 2 V

increase, the actuation of the PZT-5H chip is not consistent (not linear). Figure 3.17 shows that in the 95 samples, the actuation of 10, 12 and 13 pixels have the biggest probability (near 15% for each). The dip at 11 is due to the small sample size (Fig. 3.17). More accurate sampling during 0 to 190 V can be achieved by using a digital to analog converter instead of using the voltage divider in this study (Fig. 3.10).
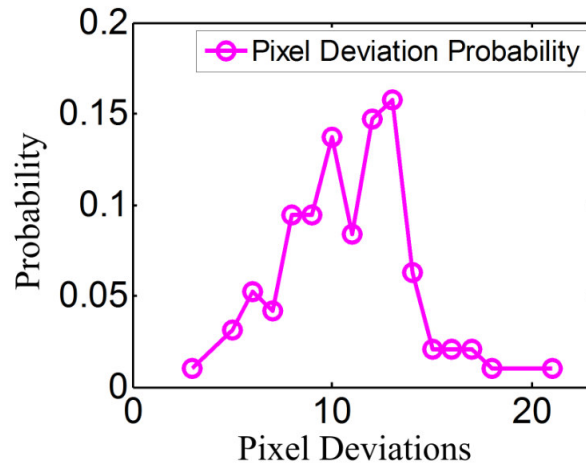
Fig. 3.17 The probability distributions of the pixel deviations for every 2 V increase.

The pixel deviations are directly calculated from the pixel values of the vertices in the binary map (Fig. 3.14). Several factors may affect the result including the vibrations of the experiment bench, subtle vibrations introduced by the manually voltage adjustment process and the light source variations in the environment. A variation of 8-13 pixels corresponds to roughly 2 to 3 µm which indicates the proposed technique has good resolution.
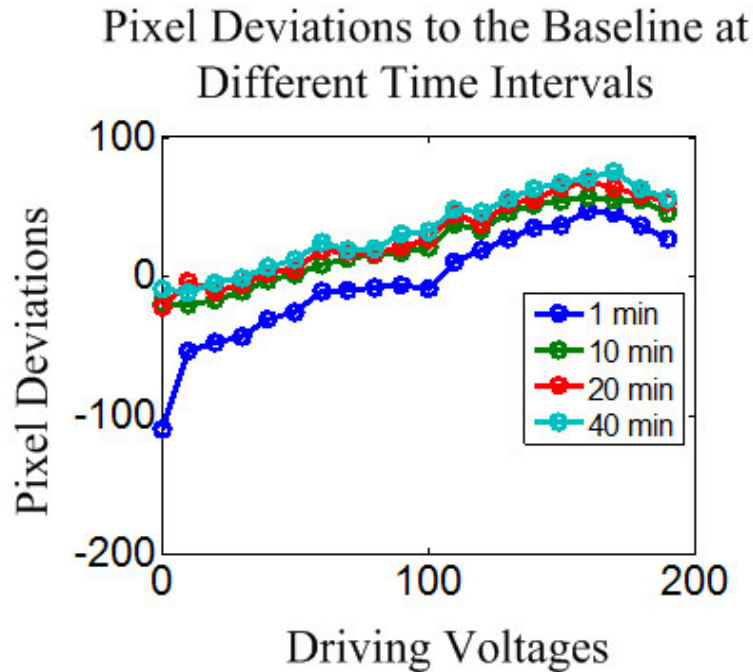
Fig. 3.18 The pixel deviations to the baseline (0 V pixel value) with different time intervals are obtained by subtracting the 0 V pixel value from the pixel values of other input voltages with different time intervals (1 min, 10 min, 20 min and 40 min).

The repeatability of the PZT-5H actuations were also investigated in this study. When the first voltage sweep was done, repetitive tests were conducted with time intervals of 1 min, 10 min, 20 min and 40 min respectively. The test results are shown in Figs. 3.18 and 3.19. The sampled voltages are from 0 to 190 V in 10 V intervals. Experiment results show the repeatability is bad if there is almost no break during two experiments. The PZT-5H chip needs at least 20 min to recover the mechanical properties after the first test.

The pixel deviations are relatively small if the PZT-5H driving voltages are between 10 and 90 V. Smaller and higher driving voltages have bigger pixel deviations.
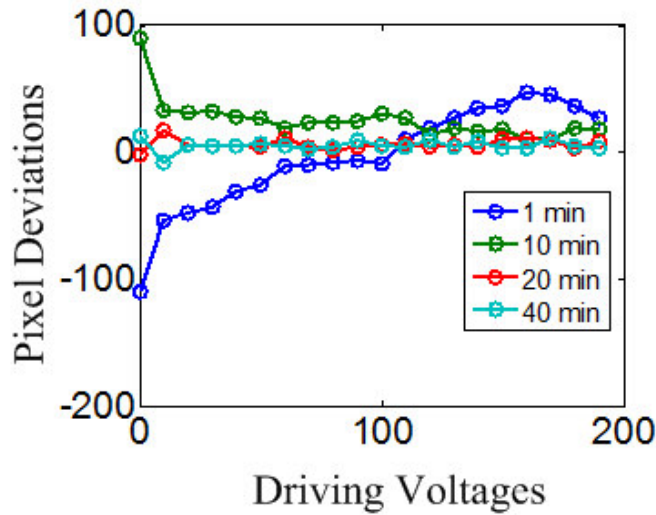
Fig. 3.19 The pixel deviations between each two applied driving voltages with different time intervals (1 min, 10 min, 20 min and 40 min).

The pixel deviations for each 2 V driving voltage increase become stable after 20 minutes following the previous experiments. The pixel deviations at low and high cantilever deflection voltages are relatively large. The PZT-5H has the best linearity with driving voltages between 10 and 90 V. At low and high driving voltages, the linearity and the repeatability are poor even with a break time between experiments longer than 40 min.

3.2.4 Conclusion

A bimorph piezoelectric cantilever displacement measurement technique is proposed and developed in this study. Sharp micro-markers are fabricated using photolithography. High resolution stereoscope imaging is used to monitor the micro displacement of the micro-marker. Clear edges are obtained by using the high resolution stereomicroscope. The vertices of the triangle-shaped micro-marker are tracked to measure the displacement of the PZT-5H chip.

66

Experiments show that the PZT-5H chip works in good linearity from 10 V to 90 V. At least 20 min break is required to recover the mechanical properties (repeatability) of the PZT-5H chip.

All actuators that can fit into the microscope slot with micrometer actuations can be measured by this technique. The displacement measurements can be conducted without any laser equipment. Manually adjusting the voltage divider seen in Fig. 3.10 may introduce deviations into the experiments. A pre-programmed microcontroller working with a digital to analog converter can reduce these deviations. The data presented in this study can be used to calibrate the PZT-5H displacement measurements.

3.3 Precise ewod top plate positioning using inverse preisach model based hysteresis compensation

3.3.1 Introduction

There are mainly two types of EWOD topologies. One is the single-plate topology; the other one is the dual-plate topology. The evaporation of the liquid in the single-plate system is a big problem. The droplet is in micro-liter or nano-liter level, so evaporation during the experimental process is significant. The dual plate system is more robust and versatile because of less evaporation and the capability of operating more droplet behaviors such as dispensing, merging, actuating and splitting (Cho et al., 2003). With a global grounded top plate, only the target electrode needs to be activated for actuation and all the other unused electrodes are floated. The single plate configuration requires the neighboring electrodes to be grounded, which leads to low usage efficiency of the electrode array. The switch-like control of the electrodes in the dual plate configuration is more interface-friendly to digital electronics. However, the gap height (top plate height) has a great influence on droplet manipulation (Yafia & Najjaran, 2013) in a dual plate system and thus a height adjustable top plate is desirable. In this paper a precise top plate

positioning technique is achieved by using two bimorph piezoelectric cantilever beams (PZT material). The PZT plate is capable of delivering sub-micron displacements with several millivolts of applied control voltage. Because of the outstanding performance in resolution, stiffness and bandwidth, piezoelectric actuators are widely used for accurate positioning tasks (Walters et al., 1996). Because of the displacement-to-voltage nonlinearity of the PZT plate (Mayergoyz, 1986), an intelligent control model is required for accurate positioning. Modeling the displacement based on history measurements can predict future displacements (Ge & Jouaneh, 1995) and shorten the convergence time. There are several popular modeling techniques such as Maxwell Model (Goldfarb & Celanovic, 1997), Jiles-Atherton model (Dupre, Van Keer, & Melkebeek, 1999), Duhem model & Prandtl-Ishlinskii model (Bashash & Jalili, 2007) and Preisach model (G. Song, Zhao, Zhou, Abreu-García, & Alexis, 2005). The Preisach model is the most successful method for modeling a system's magnetic hysteresis (Chi, Jia, & Xu, 2014). By using the hysteresis models, the physical hysteresis is partially compensated and the piezoelectric actuations are linearized versus with the input voltages.

In this section, an inverse Preisach model is developed for the PZT mounted EWOD top plate displacement tracking system. Experimental first order reversal curves are used for the model. Potential applications of the proposed model are discussed.

3.3.2 Materials and methods

The top plate is mounted to two PZT plates which are fixed by two binding posts on the other end. The top plate ITO (indium tin oxide) side is grounded all the time for proper droplet operations. A high voltage module purchased from EMCO (EMCO F40, Schweiz, Switzerland) is used as the high voltage source to provide the driving voltages to the PZT chip and the EWOD electrodes. The great benefit of using EMCO driving circuit is saving the space of using bench

function generators & amplifiers. A laser displacement sensor (Z4M-S40, Kyoto, Japan) and its manufactural amplifier (Z4M-W40, Kyoto, Japan) are used to monitor the PZT displacement. The laser displacement sensor can perform high resolution (100 nm), high bandwidth (1 kHz) and non-contact displacement measurement. Fast and precise displacement data can be achieved without affecting the mechanical vibration properties of the structure.

Instead of using a bench signal generator and amplifier, an MCU (PIC24fJ96, 16 bits) and a DAC (MCP4921, 12 bits, SPI interface) module are used to generate the high voltage triangle waves (Fig. 3.20). The output voltage of Z4M-W40 is 0-200 mV, so a second stage inverting amplifier is required to levitate the voltage level for the ADC (ADC, 0-3.3 V) (Fig. 3.20). To avoid op-amp saturation, the gain of the inverting op-amp is set less than 10; so another noninverting op-amp is needed as the third stage amplifier. Offset voltages for these two op-amps should be tuned with potentiometers in series with the resistors (Fig. 3.20b).

A desktop PC (ASUS, Intel i5 2.53 GHz, RAM 8 GB) is used for data collection and sending driving voltages to the DAC & MCU module. The DAC translates the digital driving voltages to 0-2.7 V. An additional linear high voltage amplifier is developed to modulate the 0-2.7 V to 0-200 V to drive the PZT plates (Fig. 3.20). Figure caption should be on the same page as figure
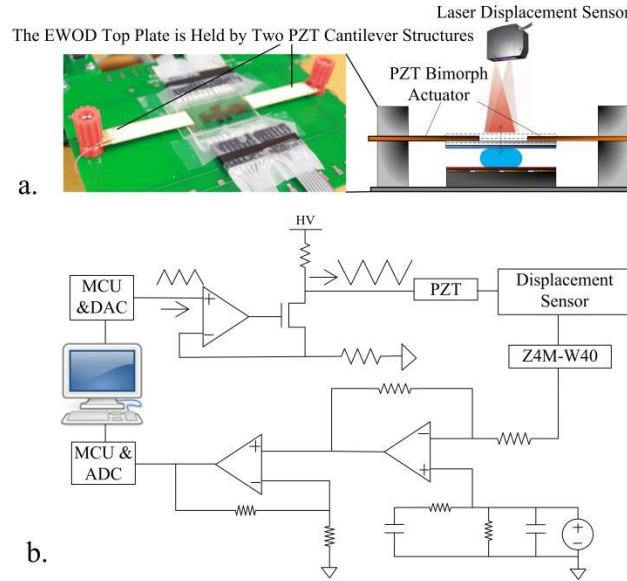
Fig. 3.20 (a) The experiment setup of the EWOD system and the cross section of the PZT cantilever structure with the EWOD system. (b) The proposed portable EWOD top plate positioning system.

Mathematical models for PZT can predict the displacement output and compensate for the nonlinearity. With a set of linear voltage input (reversal), the hysteresis of the PZT displacement has nonlinearity curves that are similar to an ascending exponential curve and a descending logarithmic curve. The mathematical model based on the interaction of the charges and the polarization of the internal dipoles is highly dependent on different types of PZT chips (Bazghaleh, Grainger, Mohammadzaheri, Cazzolato, & Lu, 2013). Preisach hysteresis model is independent of the physical properties of the PZT chips. The extremum of the ascending (α) and the descending (β) curves are set as the x and y limit respectively. Different (α, β) pairs can be tested. The (α, β) pairs are also called hysterons of the system. For multiple first order reversal curves, the memory curve structure for the Preisach operator is formed by different hysteron pairs. P+ and P− are the regions on the Preisach plane where the corresponding hysteron outputs

are positive and negative respectively. The corners of the memory curve remember the dominant maximum and minimum values of the input in the past (Fig. 3.21).

It is obviously that when α increases, the area of the shaded parts in Fig. 3.21 increases exponentially; when β decreases, the shaded area decreases logarithmically. The shaded areas in the triangle model behave very similar to the displacement hysteresis of the PZT chips. With this geometrical model and a proper weighting value for each hysteron pair, the voltage to displacement hysteresis loops can be predicted.
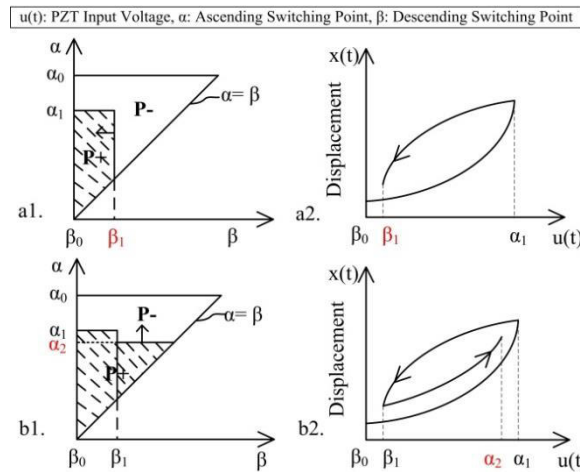
Fig. 3.21 The multiple first order reversal curves and their corresponding representations in the Preisach triangle.

It is obviously that when α increases, the area of the shaded parts in Fig. 3.21 increases exponentially; when β decreases, the shaded area decreases logarithmically. The shaded areas in the triangle model behave very similar to the displacement hysteresis of the PZT chips. With this geometrical model and a proper weighting value for each hysteron pair, the voltage to displacement hysteresis loops can be predicted.

The first order reversal curve in the Preisach model is used for the PZT displacement test. The experimental input voltage and the corresponding output is shown in Fig. 3.22a. This curve

is the result of the integral of the input voltage in both ascending and descending directions. The result of the input integration is a dimensionless parameter. The actual PZT displacement curve looks similar to this curve but needs to be fitted by the curve in Fig. 3.22a by dividing the weighting function (Fig. 3.22b) for each sampled points.

The Preisach model is given as:

$$x(t) = \iint_{P+} \mu(\alpha, \beta) \gamma_{\alpha\beta}[u(t)] d\alpha d\beta$$

$$- \iint_{P-} \mu(\alpha, \beta) \gamma_{\alpha\beta}[u(t)] d\alpha d\beta \tag{3.1}$$

$$\mu(\alpha'\beta') = \frac{\partial x(\alpha', \beta')}{\partial \alpha' \partial \beta'} \tag{3.2}$$

where $\gamma_{\alpha\beta}[u(t)]$ is the operator which has a value of 1 or 0. $d\alpha d\beta$ defines the unit area of each hysteron pair in the Preisach triangle. $\mu(\alpha, \beta)$ is the weighting function which is a coefficient matrix to model the dynamic triangle area hysteresis curves to the real displacement hysteresis curve. In other words, the integral of the dynamic triangle areas has a similar shape with the real PZT displacement curves; the weighting function $\mu(\alpha, \beta)$ is used to project each element in the model matrix to the real displacement matrix. Since the PZT chip displacement has a good repeatability, the previous experimental data can be used to create this weighting function matrix; so future nonlinear displacements can be predicted.

To discretize the Peisach model, Eq. 3.3 can be treated as a summation of the P+ and the P-triangle areas (Fig. 3.21). Using the double differentiation in Eq. 3.4 to solve the weighting function $\mu(\alpha, \beta)$ is not acceptable for the numerical computation. The weighting function matrix is obtained using a set of experimental displacement curves divided by the integration of the input voltages.

When the input is increasing monotonically, the discretized algorithm is introduced as:

$$x(\mathrm{n})_{P+} = \sum_{n=1}^{K}[(\alpha_n - \alpha_0)^2/2] \tag{3.3}$$

$$x(\mathrm{n})_{P-} = \sum_{n=1}^{K}[(\beta_k - \beta_n)^2/2] \tag{3.4}$$

where K is the number of the total input voltage values. α_n is the current ascending element, α_0 is the start ascending hysteron, β_n is the current descending sample, β_k is the start descending hysteron. The integration of the Preisach triangle area can be represented as:

$$x(\mathrm{n}) = x(\mathrm{n})_{P+} - x(\mathrm{n})_{P-}$$

$$= \sum_{n=1}^{K}[(\alpha_n - \alpha_0)^2/2] - \sum_{n=1}^{K}[(\beta_k - \beta_n)^2/2] \tag{3.5}$$

A typical Preisach modeling curve obtained from the experimental data is shown in Fig. 3.22a. The corresponding weighting function is shown in Fig. 3.22b. The first order reversal hysteresis loop shown in Fig. 3.22a has a similar shape to the real PZT hysteresis loops.
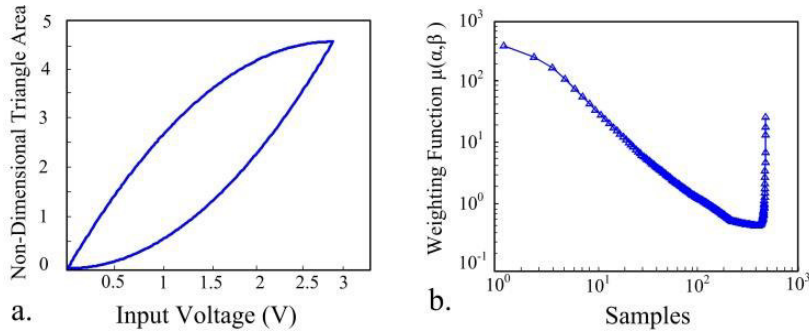
Fig. 3.22 (a) Integration of the linear voltage input (not real displacement). The ascending curve represents the increasing area of the Preisach triangle. The descending curve represents the decreasing area of the Preisach triangle. (b) The weighting function (coefficient matrix) used to project the obtained integration values to the predicted PZT displacement curves.

The ascending curve is below the linear curve 'x=y'; so if the desired output is 2 V, the input should be larger than 2 V. The exact value for the desired output is extracted from the model. Based on the previous experimental dataset, the corresponding input for the 2 V output can be found. If the desired voltage is not in the dataset, the closest matched data should be used as the predicted input.

For example, the model is designed as $\alpha_k = \beta_k$, which means the linear model is the same as y=x, and the output range should be the same as the input range. In this case, the desired output has the same values to the input. When the input values are sampled by the ADC and integrated by the Preisach model, the software in the PC starts searching the closest output values in the previous experimental hysteresis curves and their corresponding input. Then a feedforward loop is used to compensate the initial input to linearize the output. Using the feedforward compensation, the PZT system can be treated as a linear system, and then eliminate the remaining errors using a PID (proportional-integral-derivative) or a PI (proportional-integral) controller.

3.3.3 Results

The differential nonlinearity (DNL) of the high voltage DAC was tested, Fig. 3.23. The input voltage to the DAC is increased from 0 V to 2.7 V. For the 12 bit DAC, one LSB is 0.65 mV in theory. In the real test, an 11 bit DAC is used. For each 8 digits increase in the input to the DAC can cause 1 V increase at the high voltage DAC; so the real LSB is 1.3 mV and the gain of the DAC amplifier is 1 V / 8×1.3 mV = 96.15. The worst DNL is around 5/8 LSB, which is 0.8125 mV, which is good enough for our hundred-volts level applications (Fig. 3.23).
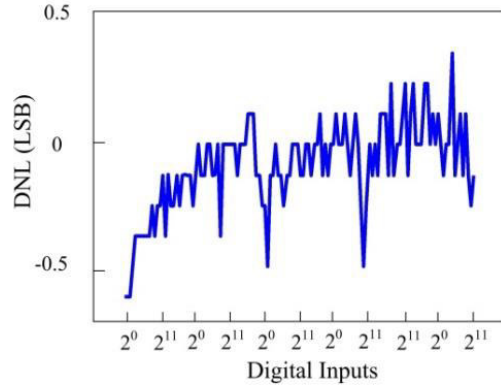
Fig. 3.23 The DNL of the high voltage DAC.

The first order reversal curve is shown in Fig. 3.24a. The input is 0-2.7 V, 0.067 Hz triangle waves. The inverse Preisach model of the hysteresis is shown in Fig. 3.24b. The summation of the two curves is shown in Fig. 3.24c, which has a very good linearity.
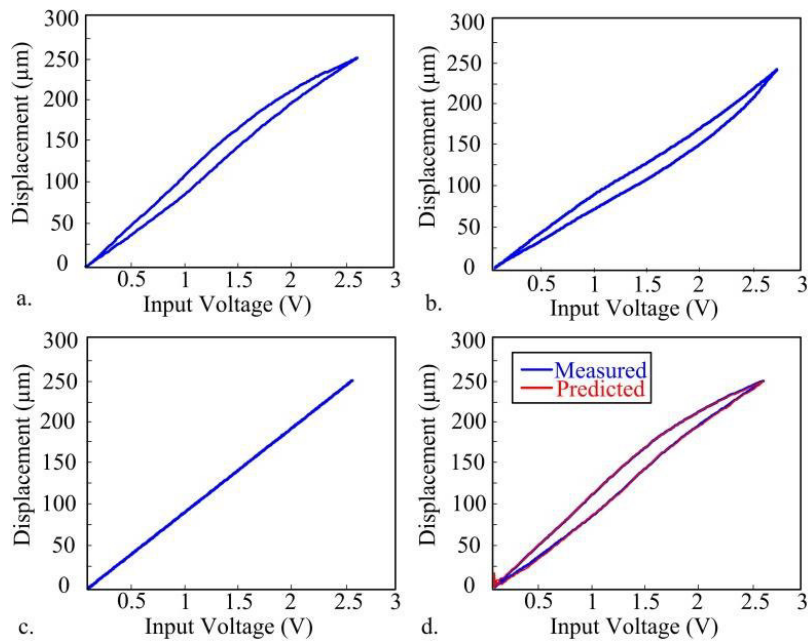
Fig. 3.24 (a) The experimental first order ascending and descending curves. (b) The inverse Preisach model. (c) The linearized result. (d) The measured and the predicted displacement hysteresis loop.

The first period of the triangle wave is used to build the Preisach model (Fig. 3.25a); the sampled four periods are tested in the tracking experiment. The largest error shown in the tracking experiment is less than 5 µm (Fig. 3.25b) without using any feedback controller. The most significant errors happened at small ascending hysterons (Fig. 3.25b). This can be improved by interpolating the modeling curves in Fig. 3.22a so that the phase differences of the modeled curves and the real time input voltages have less influence on the displacement.
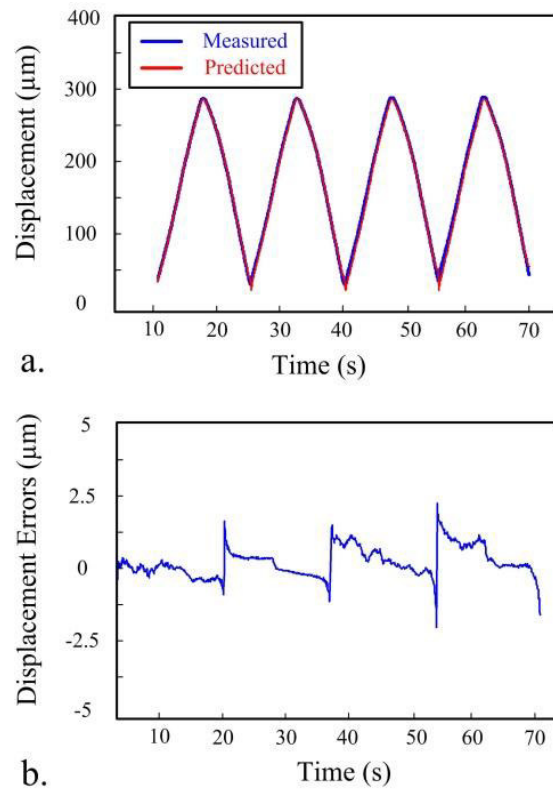
Fig. 3.25 (a) EWOD top plate displacement tracking. (b) Tracking errors between the real displacement and the prediction.

3.3.4 Conclusion

A feedforward compensated PZT controlled EWOD top plate system is proposed in this study. The PZT cantilever structure is used to position the top plate in an EWOD system. A first

order Preisach reversal curve is used to model the nonlinearity of the PZT displacements. The Preisach model is used to predict the deflection of the PZT-mounted EWOD top plate. The proposed linear high voltage DAC has a worst-case DNL of 0.8125 mV, which works well as a submicron PZT driver. The tracking error for a 0.067 Hz triangle wave input is less than 5 µm. The top plate control system is modeled in this study. Results show the inverse classic Preisach model can be used to precisely control the gap height in an EWOD system.

3.4 Improving the performance of electrowetting on dielectric microfluidics using piezoelectric top plate control

3.4.1. Introduction

Electrowetting on dielectric (EWOD) digital microfluidics (DMF) is one of the most promising lab-on-a-chip techniques. With friendly interfaces to computers and microcontrollers, batch processing of droplet actuation (W. C. Nelson & Kim, 2012), merging (Paik et al., 2003), splitting (Cho et al., 2003), position detection, droplet composition identification (Y. Li et al., 2014; Schertzer et al., 2010) and even volume controlled dispensing are all possible on a DMF chip (Gong, 2008; Ren et al., 2004). EWOD DMF chips can be fabricated on low-cost substrates such as glass (Ng et al., 2012; Ng et al., 2015), printed circuit board (PCB) (Abdelgawad & Wheeler, 2007; Abdelgawad & Wheeler, 2008; Gong, 2008; Y. Li et al., 2014), polyimide film (Kirby & Wheeler, 2013) and paper (Fobel et al., 2014). As the cost and size of the DMF chip decreases, the EWOD system can be integrated with portable electronics for point-of-care diagnostics (Ng, Uddayasankar, & Wheeler, 2010; Ng et al., 2012; Ng et al., 2015). Generally, a robust and clinically practical DMF device should have properties such as disposable DMF electrode card, efficient droplet actuation, low actuation threshold voltage and high electrode break down voltage.

Efforts have been made to lower the threshold voltage and speed-up droplet actuation. These efforts include reducing the liquid-dielectric interfacial tension (Moon et al., 2002), using the materials that has larger dielectric constant (Lin et al., 2010; Moon et al., 2002), using an oil environment (Berthier et al., 2007; Cooney et al., 2006; Lin et al., 2010; Moon et al., 2002; M. Pollack et al., 2002; M. G. Pollack et al., 2000) and decreasing the dielectric insulator thickness (Lin et al., 2010; Moon et al., 2002). However, using an oil environment may contaminate the diagnostic chemicals; thinner dielectric layers are vulnerable to pinholes and dielectric break down. The droplet actuation velocity is mainly dependent on the roughness of the hydrophobic surface, the composition of the droplet, and the strength of the electric field. The droplet actuation velocity can be improved by using a single-plate topology to avoid the extra friction from the top plate (Banerjee et al., 2011). Also, it can be improved using a silicone oil environment in a chamber to eliminate the contact angle hysteresis (Brassard et al., 2008). Additionally, modulating the driving voltages are reported to increase the actuation velocity such as using a single pulse (J. Hong et al., 2013), pulse train (Koo & Kim, 2013), AC waves (Abdelgawad & Wheeler, 2008) and pulse-width modified voltages (T. Chen et al., 2014; Dong et al., 2014; Murran & Najjaran, 2012a).

The top plate introduces more frictions and therefore requires a higher actuation threshold voltage. Another uncertainty introduced by the top plate is the aspect ratio (DeVoria & Mohseni, 2015), which is the ratio of the gap height to the droplet pitch. The aspect ratio has been reported in its significant influence on droplet kinetics (C. Chen, Tsai, Chen, & Jang, 2011; Yafia & Najjaran, 2013). Homogeneous gap height cannot provide optimized droplet operation if the droplets have various volumes. Conventionally, a double sided tape is used as the spacer for the dual-plate configuration (Gao et al., 2013; Ng et al., 2012; Ng et al., 2015). The thickness of a

layer of the standard commercially available double sided tape is roughly 50 µm - 75 µm. Adjusting the gap height by adding or removing the tape layers is too coarse for optimizing the system's performance. Thus, a continuously adjustable gap height is desired. So far the finest gap height control using a DC motor (Yafia & Najjaran, 2013) suffers from a low resolution (50 µm). In this study, the traditional DMF system is optimized using a quasi-static top plate to accurately adjusting the gap height and gently adding top plate vibrations. A precise top plate positioning technique is achieved by using two bimorph piezoelectric (PZT) cantilever beams. A cantilever beam is a rigid structure which has only one end anchored and another end is used to support the load. Cantilever structures can be found in both large construction (such as bridges, buildings and aircraft) (Cruz et al., 1998; Salawu & Williams, 1995) and small microelectromechanical systems (MEMS) (Beaulieu et al., 2007; Kranz et al., 2001). The PZT plate can resolve sub-micron displacements. Piezoelectric actuators are widely used for accurate positioning tasks (Fairbairn & Moheimani, 2013; Walters et al., 1996). Controlled by the PZT actuator, the top plate can be precisely positioned and vibrated.

In this study, a PZT controlled DMF top plate is used to accurately define the gap height and provide harmonic vibrations to optimize the droplet operations on the proposed DMF system. The droplet actuation threshold voltage and velocity are tested with various top plate heights and top plate vibration magnitudes and frequencies.

3.4.2. Materials and methods

Precise gap height control can be realized using two PZT cantilever beams. The EWOD chip (37.5 mm × 37.5 mm with 27 electrodes) is fixed on a PCB platform (Fig. 3.26 (a) and (b)). The top plate is mounted to two PZT plates which are fixed by two binding posts. The on-chip chromium pins are connected to stranded wires using silver conductive epoxy. The top plate ITO

(indium-tin-oxide) side is grounded all the time for proper droplet operations. A high voltage module purchased from EMCO (EMCO F40, Schweiz, Switzerland) is used as the high voltage source to provide the driving voltages to the PZT chip and the EWOD electrodes. The great benefit of using EMCO and the simple CMOS gate arrays as the EWOD driving circuit is saving the space of using bench function generators & amplifiers. Laser displacement sensor (Z4M-S40, Kyoto, Japan) and its manufactural amplifier (Z4M-W40, Kyoto, Japan) are used to monitor the PZT displacement. The laser displacement sensor can perform high resolution (100 nm), broad bandwidth (1 kHz) and contactless displacement measurement. Fast and precise displacement data can be achieved without affecting the mechanical vibration properties of the structure. The output voltage from Z4M-W40 is 0-200 mV, a second stage amplifier is required to levitate the voltage level for the ADC (ADC, 0-3.3 V) (Fig. 3.26 (c)). A desktop PC (ASUS, Intel i5 2.53 GHz, RAM 8 GB) is used for data collection and sending feedback driving voltages to the DAC & MCU module. The DAC translates the digital driving voltages to 0-2.54 V. An additional linear DC high voltage amplifier is developed to modulate the 0-2.54 V to 0-200 V to drive the PZT plates. The feedback loop can be automatically controlled by the software built in the PC, or visually controlled by a person if needed.

A novel modular design is introduced to the EWOD system. The EWOD electrode control system is integrated into two portable modules (Fig. 3.26 (b)); one is the relay array, the other one is the control hub. The EWOD chip is mounted on a PCB platform and connected to the relay array module with standard flexible flat cables (FFC). EWOD electrode driving voltages are obtained from the drains of the high-voltage CMOS transistors (Fig. 3.26 (d)). Various frequencies of the actuating voltage can be obtained by toggling the gates of the transistors with different rates (DC pulses at 10 kHz and various voltages).

80
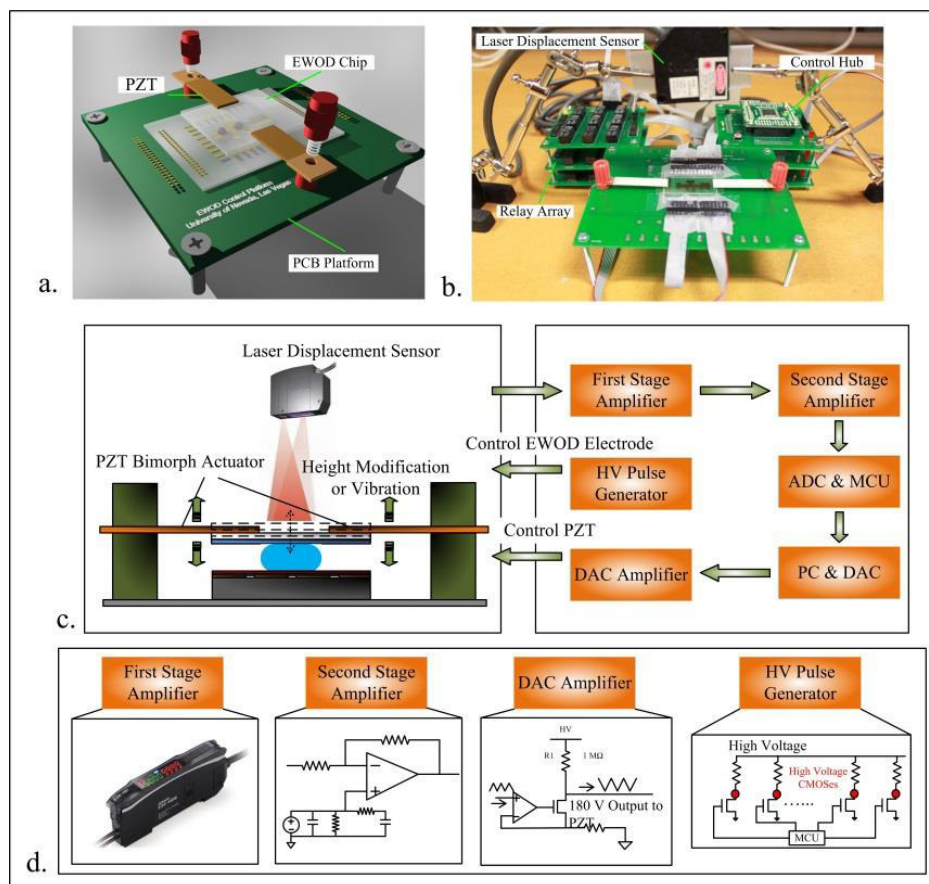
Fig. 3.26 (a and b) The 3D model and the experiment setup of the EWOD platform. (c and d) The system overview of the DMF and the PZT top plate control module.

Devices were fabricated in the cleanroom facility of Nevada Nanotechnology Center at University of Nevada, Las Vegas. The fabrication reagents includes Schott Boro Float glass substrate with Chrome coated (100 nm) microfluidic blank slides (with positive photoresist coated, Telic, Valencia, CA, USA), Teflon-AF solution (amorphous fluoroplastic resin in solution, 400S2-100-1, DuPont, Mississauga, ON, CA), photoresist developer RD6 (Futurrex, INC., Franklin, NJ, USA), Chromium etchant (Sigma-Aldrich, Co., MO, USA), photoresist remover (Microposit Remover 1165, Rohm and Haas Electronic Materials LLC, MA, USA), indium tin oxide (ITO) coated glass (Adafruit INC., NYC, USA). Open source integrated circuit (IC) layout tools Electric VLSI (Http://Cmosedu.com/cmos1/electric/electric.htm.) is used to

pattern the mask of the electrode array. GDSII output files from Electric VLSI are sent to Infinite Graphics INC. (MN, USA) for plotting (25,000 dpi). During the photolithography process, the substrates are covered by the patterned photomask and exposed to a UV light source for 45 seconds and then developed for 1 min in RD6. Substrates are then immersed in the Chromium etchant for about 15-20 seconds. Then the substrates are washed by DI water and dried out using nitrogen gas. The remaining photoresist is removed by Microposit Remover 1165.

It is more challenging to realize the droplet actuation, merging and splitting in an air environment rather than in an oil environment. The oil environment in the EWOD chip, to some extent, is more tolerant to dust. Also, without an oil environment, the two major microfluidic kinetic resists, the contact line pinning and contact angle hysteresis (CAH), become much more significant to prevent the droplet from being actuated. To realize a smooth actuation in air, larger electrostatic force is required. A morphological representation of the electrostatic force is the contact angle change. Obviously, the driving voltage has to be limited within the dielectric material break down voltage. Among all the candidate insulator materials, parylene C stands out for its high dielectric constant and the high break down voltage. In order to make the surface more robust for higher voltages, an 8 µm parylene C is coated to the EWOD chip by a chemical adhesion process. Prior to parylene C coating, the chips were cleaned using a Plasma Etch process. The Plasma etch process utilizes Oxygen and an inert gas (Argon or Nitrogen) to increase surface wettability and clean away any oils or fiber-molecules. Then, the chips are fixed on the masked areas. The chips are loaded into the CVD chambers. Vapor-Phase Silane (VPS) is introduced into the chamber and acts as an aerosol primer to enhance the chemical adhesion to the parylene C surface. The parylene dimer is loaded into the pyrolizer and enters the chamber with the EWOD chips as a monomer gas. The gas polymerizes on any surface area that remains

at room-temperature. The gas flow is manipulated and deposit in such a way that the thickness and the uniformity of the coating can be controlled. 250 nm Teflon AF solutions are then spin coated on the chip as the hydrophobic top layer.

A high speed camera (up to 1000 fps, Casio ZR200, Japan) and a handled digital microscope (Celestron, CA) are used to capture the droplet motion and measure the instantaneous velocity. The actuation velocity and the minimum threshold voltage depend on the droplet volume, top plate height, top plate vibration magnitude and frequency. The top plate height and vibration are controlled by the commands sent from the PC. Feedback signals of the real top plate height are displayed on the PC in real time so the top plate can be adjusted to the desired height by adjusting the PZT driving voltages. Open source software ImageJ and Tracker are used to measure the droplet displacement and volumes.

The droplet driving voltage is controlled by a potentiometer and monitored by an oscilloscope. The minimum threshold voltage is recorded as the minimum voltage to actuate the droplet. The data presented in each discrete box in this figure is an average of six repeated tests. To avoid the voltage and velocity deviations caused by different electrodes, the minimum actuation voltage and the maximum instantaneous velocity are measured with the same starting electrode and target electrode. The droplet velocity is analyzed using Camtasia (Okemos, MI) ($dv=ds/dt$, v is the velocity, s is the displacement, t is the time spent for the movement).

3.4.3. Results

In this study, it is assumed that vibrating the top plate instead of vibrating the substrate can lower the actuation threshold voltage, release the pinned droplet, and decrease the failure rate of the experiments. This gentle intervention added to the EWOD system will not harm normal EWOD operations. Here, PZT bimorph piezoelectric plates are employed as the vibration source

for the top plates. The PZT chip displacement and vibration behavior have been extensively studied (Fairbairn & Moheimani, 2013; Robert, Damjanovic, Setter, & Turik, 2001; X. Zhao & Tan, 2006). Sub-milimeter vibration can be well controlled by a computer system, which makes it a perfect candidate to be the EWOD top plate holder and actuator.

In Fig. 3.27, the subfigures are consecutive snapshots of the droplet actuation with top plate vibration at 200 µm and 25 Hz (Droplet 1) and 100 µm, 25 Hz (Droplet 2). The vibration baseline is at 100 µm away from the bottom plate; the vibration goes from "100 µm + *0 µm*" to "100 µm + *100 µm*" or "100 µm + *200 µm*" but never goes below the baseline (100 µm). The droplet under stronger top plate vibration has a significantly higher instantaneous velocity while the droplet travels through the three electrodes (Fig. 3.27 (a)). The maximum droplet instantaneous velocity is around 9.3 mm/s which is almost 3 times faster than the droplet velocity without top plate vibration (Fig. 3.27). The droplet velocity improvements are more significant under stronger top plate vibrations.
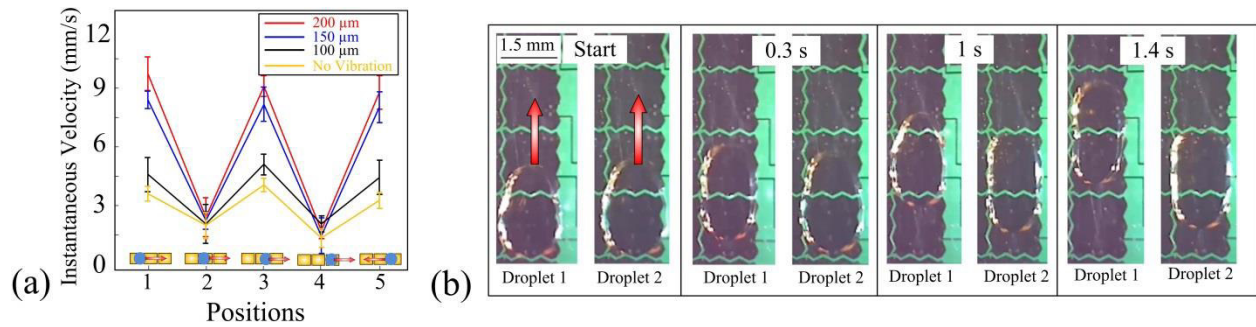
Fig. 3.27 Top plate vibrations speed up the droplet velocity. (a) Droplet instantaneous velocity at five different positions while the droplet travels through three electrodes. (b) Consecutive snapshots of water droplets with 200 µm (Droplet 1) and 100 µm (Droplet 2) top plate vibrations.

The minimum actuation voltage is the threshold voltage to trigger the droplet to move. First, a droplet was dispensed from the reservoir at a certain gap height. The droplet driving voltage was adjusted using a potentiometer. To avoid the deviations caused by different electrodes, the minimum actuation voltage is measured with the same starting electrode and destination electrode for six times. The six tests were conducted continuously with the same vibration magnitude and the same droplet position.

The vibration magnitude dependent actuation enhancement is investigated (Fig. 3.28). Using low driving voltages around threshold voltage can activate the droplet but the movement is not smooth and prone to contact line pinning. Top plate vibration can overcome the contact line pinning issue while using low driving voltages. If the top plate vibration can expedite the droplets at lower driving voltages, the threshold voltage is reduced by the vibration as well. No top plate vibration and 200 µm top plate vibration are tested (Fig. 3.28 (c) and (d)). A failed actuation is observed (Fig. 3.28c at 0:04 sec). While in Fig. 3.28(d), the droplet is activated and smoothly transported to the target electrode at 205 V_{RMS}. The contact line pinning is eliminated by the top plate vibration.
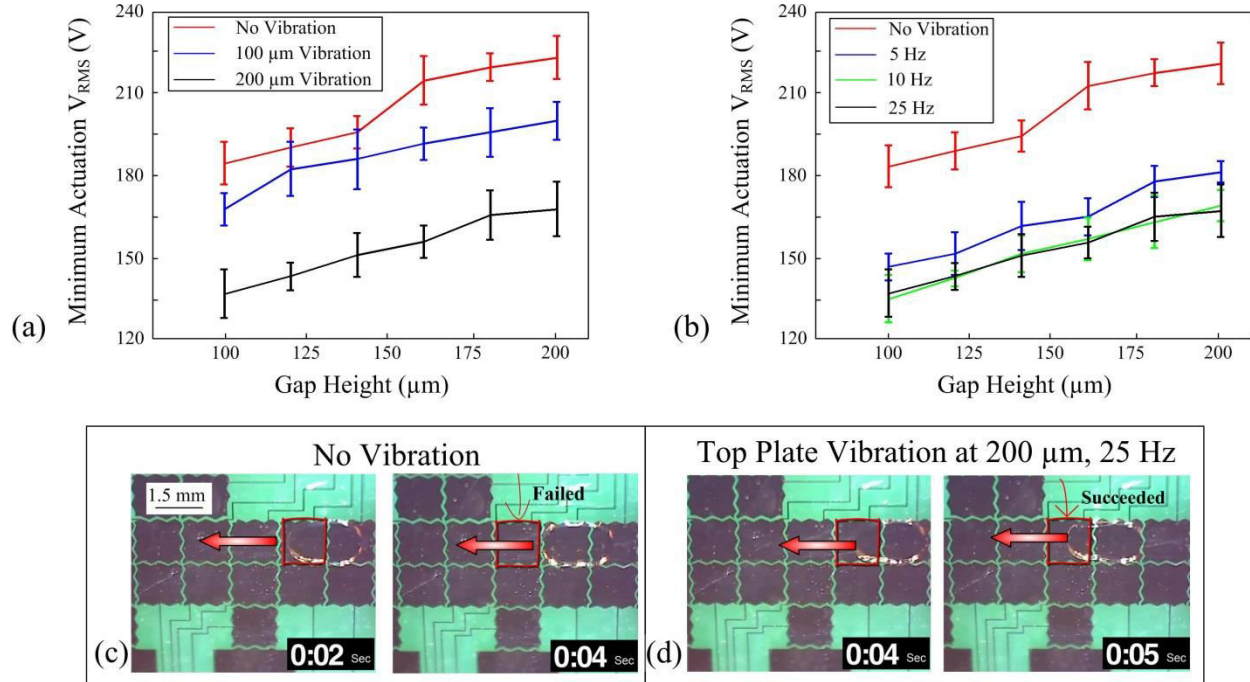
Fig. 3.28 Comparison of the minimum actuation voltages of a droplet (2.0 µl) under various top plate vibration magnitudes (a) and frequencies (b). (c) Consecutive snapshots of a failed actuation without top plate vibration and a succeeded actuation with a 200 µm, 25 Hz vibration under the same driving voltage.

For a better understanding of the underlying mechanism for the velocity and threshold voltage improvements, the droplet contact line dynamics are analyzed by observing the cross-sectional view of the droplet under top plate vibrations (Fig. 3.29, no voltage applied). The liquid-solid contact angle changes with top plate vibrations due to the continuous squeezing and relaxing operations of the droplet even when there is no voltage applied (Fig. 3.29). When squeezing the droplet, the contact line is pinning at the same location with an increasing contact angle until it reaches the advancing angle θ_a (Fig. 3.29 (a1)); when relaxing the droplet, the contact line keeps pinning at the same location until the contact angle reaches the receding angle θ_r (Fig. 3.29 (a2));. Therefore, a strong enough top plate vibration that induces sufficient contact

angle changes can depin the contact line. A sequential squeezing and relaxing operation allows the droplets to experience various metastable states that results in easier actuation towards the minimum global energy (Daniel, Sircar, Gliem, & Chaudhury, 2004; Longley et al., 2012). Once an asymmetrical voltage gradient is applied to the surface, the droplet contact angle at the higher voltage side drops substantially which results in an unbalanced electrostatic force that drags the droplet forward.
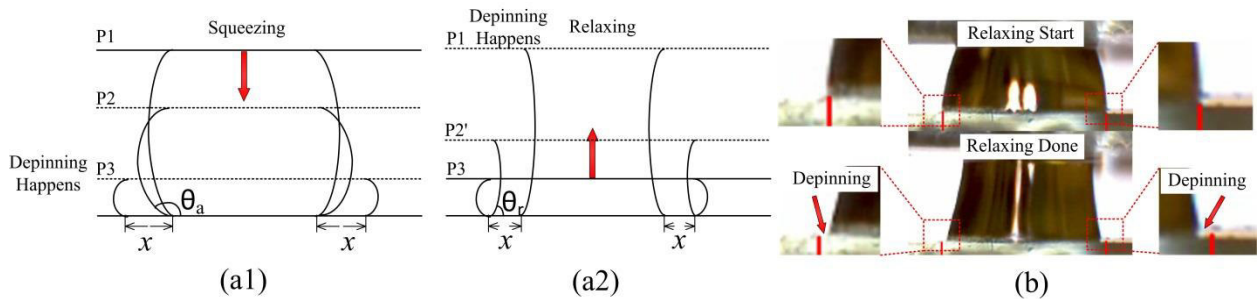
Fig. 3.29 A cross-sectional view of a DI water droplet that is sandwiched in a DMF system with a 5 Hz, 200 µm top plate vibration (no voltage is applied to the electrode). (a1) Squeezing a droplet and the depinning happens at P3. (a2) Relaxing a droplet and the depinning happens at P1. In (a1-a2), droplet contact line moves a distance of "*x*" along the surface. (b) Experiment shows the contact line depins when relaxing the water droplet.

Low frequency top plate vibration (< 25 Hz) depins the droplet contact line and makes the droplet actuation easier. One typical study using bottom substrate vibrations (30 – 1100 Hz) found 37 resonance modes of sessile droplets (C. Chang, Bostwick, Steen, & Daniel, 2013). The droplet vibration patterns are observed indirectly through analyzing the deformation of a meshed background (C. Chang et al., 2013). In this study, we use top plate vibration instead of using substrate vibration for the EWOD device. The top plate vibration platform can be developed with mounted PZT chips which are friendly to external electronics. However, the disadvantage of this

PZT is its limited bandwidth. In order to overcome the contact angle hysteresis for the actuation, the vibration magnitude has to be large (> 100 µm). The PZT chip vibration magnitude attenuates significantly at high frequencies. According to the studies in the bottom plate vibration (Daniel et al., 2004), significant velocity amplification was observed when the substrate vibration matched the natural harmonics of the drop oscillation. However, the natural harmonic oscillation of the droplet in micro liter level is usually > 300 Hz (varies with droplet mass). The PZT chip used in this study has a manufactural bandwidth of 200 Hz which is much smaller than the droplet's natural oscillation harmonics (the bandwidth goes even smaller when the PZT is loaded with the top plate).

The target electrode is applied with a voltage that changes the wettability of the surface, which is known as "electrowetting". It was first identified by Greenspan (Greenspan, 1978) that a liquid droplet placed on a chemically heterogeneous surface moves to the region of higher wettability to reduce the interfacial free energy, and experimentally demonstrated by Daniel (Daniel et al., 2004; Daniel, Chaudhury, & Chen, 2001) on a vibrated substrate with a chemical wettability gradient. It was reported that low frequency bottom substrate vibration (1 Hz) induced a droplet ratchet-like motion toward the more wettable region because of the successive pinning and depinning of contact lines allows the drop to sample various metastable states and thereby setting it to the path of global energy minima (Daniel et al., 2004). Similarly, "electrowetting" modifies the wettability of the surface with a voltage gradient instead of using a chemical gradient. If the voltage gradient is weak (low voltages), the actuation won't happen. The "top plate vibration" used in this study can trigger the droplet actuation even with a weak voltage (Fig. 3.30, using a 3 µl water droplet for a good observation of the contact angles). The voltage gradient on the DMF chip developed in this study is a binary form which has only the

voltage "on" and voltage "off" status (wetting and de-wetting). The liquid that bridges both the "on" and the "off" electrodes has an asymmetric contact angle hysteresis (Fig. 3.30). θ_{aL}, θ_{rL}, θ_{aR}, and θ_{rR} are the left advancing angle, the left receding angle, the right advancing angle, and the right receding angle. In Fig. 3.30, $\theta_{aL} > \theta_{aR}$, when squeezing the droplet, the right contact angle reaches θ_{aR} earlier and moves to the right before the left contact angle reaches θ_{aL}, which causes the left contact line to stay at the same location while the right contact line moves; when relaxing the droplet ($\theta_{rL} > \theta_{rR}$), the left contact angle reaches θ_{rL} earlier and moves to the right before the right contact line can get a chance to recede (Fig. 3.30 (c)). The asynchronous contact line movement on the left and the right side of the droplet forges a ratchet-like motion which overcomes the contact angle hysteresis on the liquid-solid interface. This enables the liquid to move under lower voltages or move quicker with a normal driving voltage.
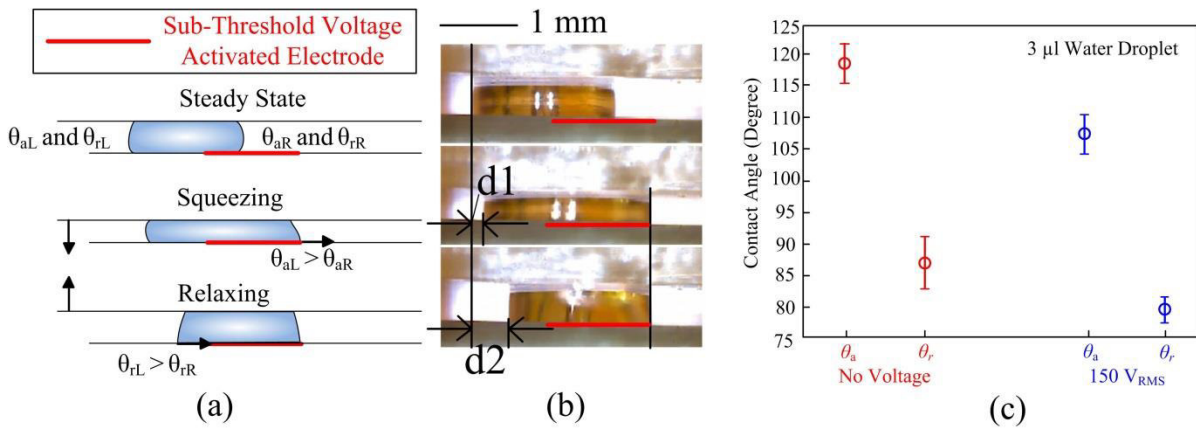
Fig. 3.30 (a) θ_{aL}, θ_{rL}, θ_{aR} and θ_{rR} are the left advancing angle, the left receding angle, the right advancing angle, and the right receding angle. The voltage applied to the electrode (using 150 V_{RMS} here) is lower than the actuation threshold voltage. The droplet has an asymmetric contact angle hysteresis at the left and the right contact line. Because $\theta_{aL} > \theta_{aR}$, when squeezing the droplet, the right contact angle reaches θ_{aR} earlier and moves to the right before the left contact angle reaches θ_{aL}; similarly, $\theta_{rL} > \theta_{rR}$, when relaxing the droplet, the left contact angle reaches

89

θ_{rL} earlier and moves to the right before the right contact line can get a chance to recede. (b) Top plate vibration triggers a ratchet-like movement of a 3 µl water drop under sub-threshold actuation voltages. (c) The advancing and receding contact angles with no voltage and with a subthreshold voltage (150 V_{RMS}) applied.

In Daniel's study (Daniel et al., 2004), a promoted droplet motion on a chemical gradient surface is realized by vibrating a sandwiched structure that is similar to the popular DMF topology. In Daniel's study, a droplet ratchet-like motion is observed by continuously squeezing and relaxing the droplet, and the droplet motion velocity increases linearly with the vibration magnitude. In Electrowetting a double layer of charges near the liquid-solid surface is formed by the electric field applied to the electrode (Quinn et al., 2003). The charge double layer lowers the surface energy, which helps spread the liquid on the surface. When the right contact line is depinned by squeezing the droplet, not only the right contact line moves but the left contact line also gets a small displacement ("d1" in Fig. 3.30 (b)), which manifests a stronger force than the chemical gradient can provide that propels the droplet forward.

Acetonitrile, which is well-known for its low viscosity (0.37 m^2 / s) and negligible contact angle hysteresis, is used as a control for the droplet velocity test under top plate vibrations. If the contact angle hysteresis is small, $\theta_a \approx \theta_r$, the vibration will not add any displacement to the droplet as indicated by the following equation (Daniel et al., 2004):

$$x = \frac{\alpha V^*}{4\omega}[(cos\theta_{rR} + cos\theta_{aR}) - (cos\theta_{rL} + cos\theta_{aL})] \qquad (3.6)$$

in which x is the droplet displacement, $V^* = Y/\eta$, Y and η are the surface tension and the viscosity of the drop. If the contact angle hysteresis is negligible, $(cos\theta_{rR} + cos\theta_{aR}) - (cos\theta_{rL} + cos\theta_{aL}) \approx 0$. Our experiment shows droplets with a high concentration of acetonitrile

is very difficult to be moved on the EWOD surface with normal actuating voltages (> 250 V$_{RMS}$), even there is a top plate vibration. The contact angle change is very small for high concentrated acetonitrile (Fig. 3.31), which indicates a weak electrostatic force. A pure acetonitrile droplet is not moveable in an EWOD DMF device. Only aqueous solutions of acetonitrile with low concentrations (< 25%) are movable.
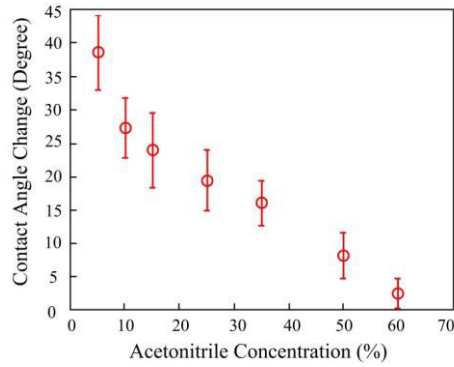
Fig. 3.31 Contact angle changes of a 3 µl acetonitrile droplet with varying concentrations. 250 V$_{RMS}$ pulses are applied to the electrode.

However, for a sessile water droplet, the droplet-substrate contact angle varies with the electrowetting number (η):

$$cos\theta = cos\theta_Y + \frac{\varepsilon_0 \varepsilon_d}{2 d \sigma_{lv}} U^2 = cos\theta_Y + \eta \qquad (3.7)$$

in which θ_Y is Young's equilibrium contact angle, ε_d is the dielectric constant of the insulation layer, d is the thickness of the insulation layer, σ_{lv} is the liquid-vapor surface tension, U is the applied voltage. When the applied voltage increases, the contact angle decreases very quickly until it is saturated. The electrowetting property of a sessile droplet is shown in Fig. 3.32 (for typical values: $\sigma_{lv} = 0.072 \, J \cdot m^{-2}$ and the dielectric material layer thickness is $d = 8 \, \mu m$).
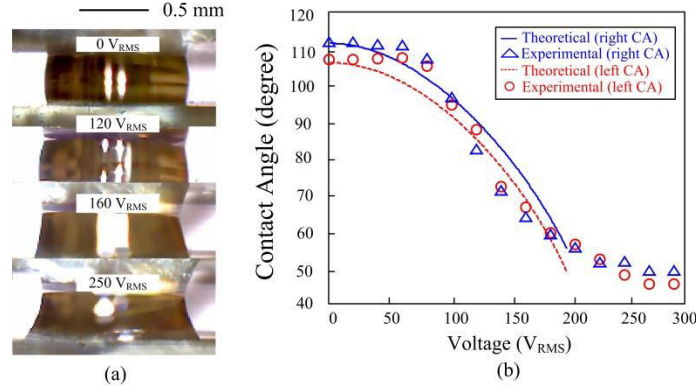
Fig. 3.32 (a) Contact angle versus applied voltage (V_{RMS}) for a DI water droplet that sandwiched between two Teflon (250 nm) coated substrates in an air ambient. (b) Experimental and theoretical contact angle changes of both the left and the right side of droplet.

The decreasing rate of the contact angle (Fig. 3.32 (b)) slows down when the driving voltage is larger than 250 V_{RMS}. This indicates the contact angle is getting saturated at higher voltages.

The purpose of the gap height optimization is to decrease the minimum actuation voltage and increase the actuation velocity. The droplet footprint area and volume have great influences on the actuation efficiency. The relationship of footprint area A, droplet volume V and gap height H can be estimated using the following equations:

$$V = A \times H \tag{3.8}$$

With the same droplet volume, the droplet footprint area can be controlled by adjusting the gap height. The droplet volume varies due to unequal dispensing, splitting or evaporation. The gap height should be adjusted to keep good footprint area for a smooth actuation. The relationship between the minimum threshold voltage and the gap height can be represented by the following equation:

$$V_{min} = \left[\left(\frac{\varepsilon_0 w}{4 d_2 \gamma} \times \frac{1}{\frac{d_1}{\varepsilon_T} + \frac{d_2}{|\varepsilon_w^*|} + \frac{d_3}{\varepsilon_T} + \frac{d_1}{\varepsilon_T}} - \frac{1}{\frac{d_1}{\varepsilon_T} + \frac{d_2}{1} + \frac{d_3}{\varepsilon_p} + \frac{d_1}{\varepsilon_T}}\right]^{-1/2} \tag{3.9}$$

and

$$\varepsilon_w^* = \varepsilon_w - j\frac{\sigma}{2\pi f \varepsilon_0} \tag{3.10}$$

where ε_0, ε_T, ε_p and ε_w^* represent the permittivity of vacuum, Teflon, parylene C and water. d_1, d_2, d_3 are the thickness of the Teflon, gap and parylene C. w is the width of the electrode. Y is the surface tension. Finally, σ is the fluid conductivity of water. The relationship between the top plate height and the minimum actuation threshold voltage can be approximated. However, in the real experiments, the diagram of the voltage and the gap height won't be monolithic (as shown in Eq. 3.9). If the top plate height is too low, the droplet is squashed to a random shape; the applied electrostatic force will not provide enough power for the actuation before the contact angle gets saturated.

Except for the gap height, there are several other environmental factors which will affect the minimum actuation voltage; such as the droplet volume, the footprint area, the droplet aspect ratio and the roughness of the surface. The minimum threshold voltage was tested with varying droplet volumes and gap heights in this study. Droplet volumes from 0.2 µl – 2.0 µl, gap heights from 50 µm – 200 µm are tested for the minimum actuation voltage.

The color-map shown in Fig. 3.33 is a 7 by 7 matrix, which has 49 points in total. There are 7 different heights and volume. The color-map using discrete colorful boxes shows the original data.

Droplets failed to move

Gap Height (μm)

(a) Minimum Actuation Voltage (V_{RMS})

Droplet Volume (μl)	50	80	100	120	150	180	200
0.2	144.9	157.7					
0.5	152.7	159.8	168.3	181.8	190.2		
0.8	166.2	171.1	179.0	192.4	203.7	206.5	211.4
1.2		177.5	181.8	193.1	204.4	215.7	217.1
1.5	181.0	186.7	196.6	207.9	216.4	219.9	
1.7		202.3	207.9	217.2	223.5	225.6	
2.0		204.4	208.6	215.0	220.7	227.1	

Droplets failed to move

Gap Height (μm)

(b) Maximum Instantaneous Velocity (mm/s)

Droplet Volume (μl)	50	80	100	120	150	180	200
0.2	4.63	3.85					
0.5	4.86	5.14	5.28	5.16	4.31		
0.8	4.58	4.96	6.27	6.32	6.08	5.78	4.87
1.2		4.47	5.36	6.59	6.21	5.19	5.08
1.5		3.74	4.58	5.62	6.14	6.05	5.23
1.7		3.15	4.92	6.19	5.54	5.19	
2.0		2.96	3.36	4.62	4.58	5.73	

Fig. 3.33 (a) The map of the minimum actuation voltage for various gap heights and droplet volumes and (b) maximum instantaneous droplet velocity with various gap heights and droplet volumes (at 300 V_{RMS} and 10 kHz).

The blue boxes in Fig. 3.33 (a) show the optimized gap heights for the droplets in 0.2 – 0.8 µl. The minimum actuation voltage overall is 144.9 V_{RMS} (50% duty cycle high frequency pulses are converted to RMS values) which occurs at 0.2 µl and 50 µm gap height. The droplets' volume ranges from 0.5 µL to 2.0 µl are more flexible to various gap heights. Large droplets with high gap heights will have larger minimum actuation voltage. Droplets with volumes less than 0.8 µl are easier to be actuated (Fig. 3.33 (a)). The droplet maximum instantaneous velocity (MIV) shows the fastest moment that the droplet travels through three continuous electrodes. Most of the fastest droplets are the ones that are close to the diagonal of the color map in Fig. 3.33 (b). While the droplet has a size of 0.6 – 1.7 µl, the gap height should between 100 – 170 µm.

A smaller working droplet is generated from a larger electrode which is a reservoir of the liquid. The forwarding electrode should be activated first to drag a certain amount of liquid from the reservoir. The electrodes in the middle of the reservoir and the targeting electrode are turned off to disconnect the dispensed droplet from the reservoir (Fig. 3.34). The biggest issue of

EWOD dispensing is the volume control. It is hard to control the dispensed droplet volume accurately. Adding capacitive sensors to a feedback control loop to manipulate the dispensed droplet volume in real time can improve the volume accuracy (Gong, 2008). But the droplet-electrode capacitive data is influenced by the droplet position as well (Y. Li et al., 2014).

A fast and accurate EWOD dispensing volume control method is proposed in this study. Once the size of the reservoir and the working electrodes are known, the dispensing droplet volume can be modified by changing the gap height. A high resolution gap height control method is desired for this modification. The gap height and the dispensed droplet volume look-up table can be obtained experimentally. Then setup of a proper gap height during the dispensing process is possible to generate a droplet with a certain volume (Fig. 3.34).

For the maximum instantaneous velocity shown in Fig. 3.34 (b), the droplet movement from one electrode to another electrode is an accelerating motion at the beginning followed by a decelerating movement. The six tests were conducted continuously with the same gap height and the same droplet position. For the threshold voltage, the SD ranges from ±1.7 V to ±8.6 V, the maximum velocity SD ranges from 0.05 mm/s to 0.37 mm/s.
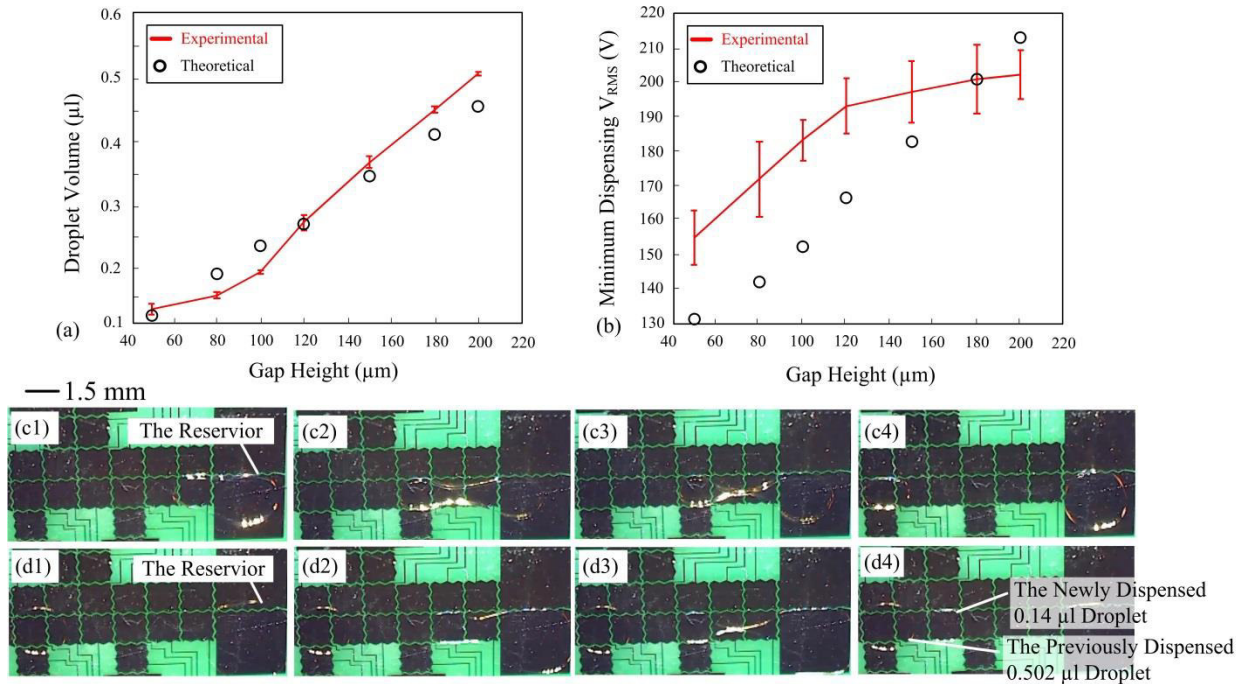
Fig. 3.34 (a) The relationship between the gap height and the dispensed droplets volumes. (b) The minimum dispensing voltage increases as the gap height increases. (c1-c4) Dispensing a 0.502 µl droplet at the gap height of 200 µm. (d1-d4) Dispensing a 0.14 µl droplet at the gap height of 75 µm.

As shown in Fig. 3.34, the theoretical dispensed droplet pitch is close to the droplet length (width). However, the experimental droplet pitch and footprint area is measured using ImageJ. The differences between the theoretical approximation and the experimental measurement are compared in Fig. 3.34a.

All the dispensing operations at the same top plate height were conducted six times. The theoretical dispensed droplet volume is calculated by assuming that the footprint area is the same as the electrode area (explained in Fig. 3.35), which is $1.5\ mm \times 1.5\ mm = 2.25\ mm^2$. The theoretical dispensed droplet volume can be calculated as: $V = A \times H$ (if there is a voltage applied to the rectangular electrode, when the droplet pitch is much larger than the gap height,

96

the droplet topology is close to a cuboid). V is the droplet volume, A is the electrode area which is a constant in this case, H is the gap height. The gap height is monitored by a laser displacement sensor. For example, a 0.1 µl droplet can be dispensed using a 50 µm gap height ($2.25 \text{ mm}^2 \times 50 \text{ µm} = 0.112 \text{ µl} \approx 0.1 \text{ µl}$).
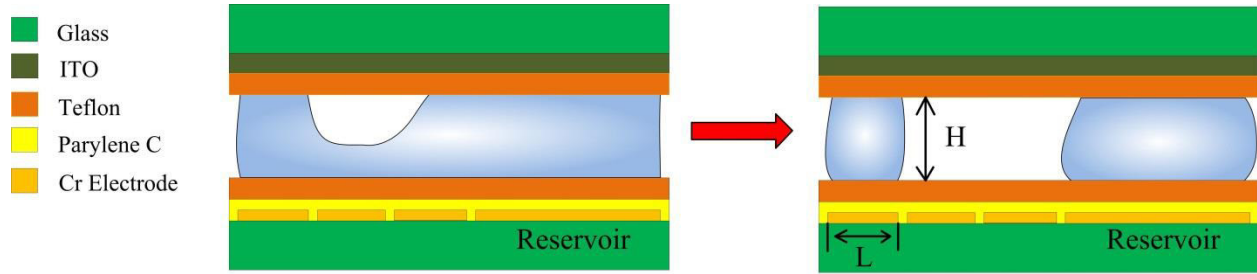
Fig. 3.35 The pitch of a dispensed droplet is similar to the electrode length L (and width).

The theoretical dispensing voltage is a little bit smaller than the splitting voltage but larger than the threshold voltage. The minimum dispensing voltage can be calculated by Eq. 3.11 (J. Song, Evans, Lin, Hsu, & Fair, 2009),

$$V = \sqrt{\frac{8\gamma_{lg} \cdot t \cdot d}{L \cdot \varepsilon_0 \cdot \varepsilon_r \cdot (N^2+1)} + V_T^2} \qquad (3.11)$$

in which V is the minimum dispensing voltage, γ_{lg} is the liquid-substrate interfacial tension, t is the dielectric layer thickness, d is the gap height, L is the electrode pitch, ε_0 is the vacuum permittivity, ε_r is the dielectric coating permittivity, N is the electrodes engaged in dispensing the droplet, V_T is the threshold voltage for droplet actuation. The theoretical and experimental minimum dispensing voltages are shown in Fig. 3.34 (b).

The deviations of the experimental data to the theoretical data in Fig. 3.34 (b) are caused by the following reasons: (1) the two variables, d and V_T, in Eq. 3.11 are obtained experimentally. Measurement errors caused by friction, contact angle hysteresis and shear force were not

considered in this equation. On the other hand, the contact angle hysteresis affects the reproducibility of the experimental dispensing voltages. From Fig. 3.34 (b), the experimental dispensing voltages increase with increasing gap height, the SD of dispensing voltages for each gap height ranges from 6 V to 11 V. We can also notice that the slope of the experimental minimum dispensing voltage decreases at higher gap heights. It is possible that the higher gap heights (< 200 µm) used in this experiment form a more favorable aspect ratio (d/L) for the dispensing operation.

The greatest benefit by using dual plate EWOD DMF chips is the ease of the splitting operation. Splitting is a critical step for concentration modification, immunoassay reaction and particle purification (Ng et al., 2012). The splitting process requires a strong body force which is related to the tradeoffs among the applied voltage, dielectric material and the hydrophobic surface coating quality. The contact line pinning and CAH of the droplet in the air environment EWOD DMF chips are much more significant than that in a silicone oil environment. Due to the liquid viscosity and the frictions of the droplet-substrate (both top and bottom) interfaces, the droplet splitting slows down or even fails. While doing the splitting experiment, the droplet is stretched by two electrodes until necking (Cho et al., 2003) appears. Stretching the droplet further results in two sister droplets. However, there can be a problem of open loop splitting. The electrodes at the two ends are competing against each other to drag the droplet forward. Due to the random unsymmetrical droplet position, the sister droplet with a larger footprint area (the position) will experience a larger electrostatic force. In this case, unsymmetrical splitting may occur. So the success of splitting also depends on the initial position of the droplet. Fast feedback capacitive sensing or an image processing controlled system may help balance the droplet position during the splitting experiment. Unsymmetrical droplet position can result in a failed

splitting operation when the droplet is small and the gap height is large. Maximum gap heights for splitting droplets ranging from 1.4 µl to 2.0 µl are investigated (Fig. 3.36a) in this study.
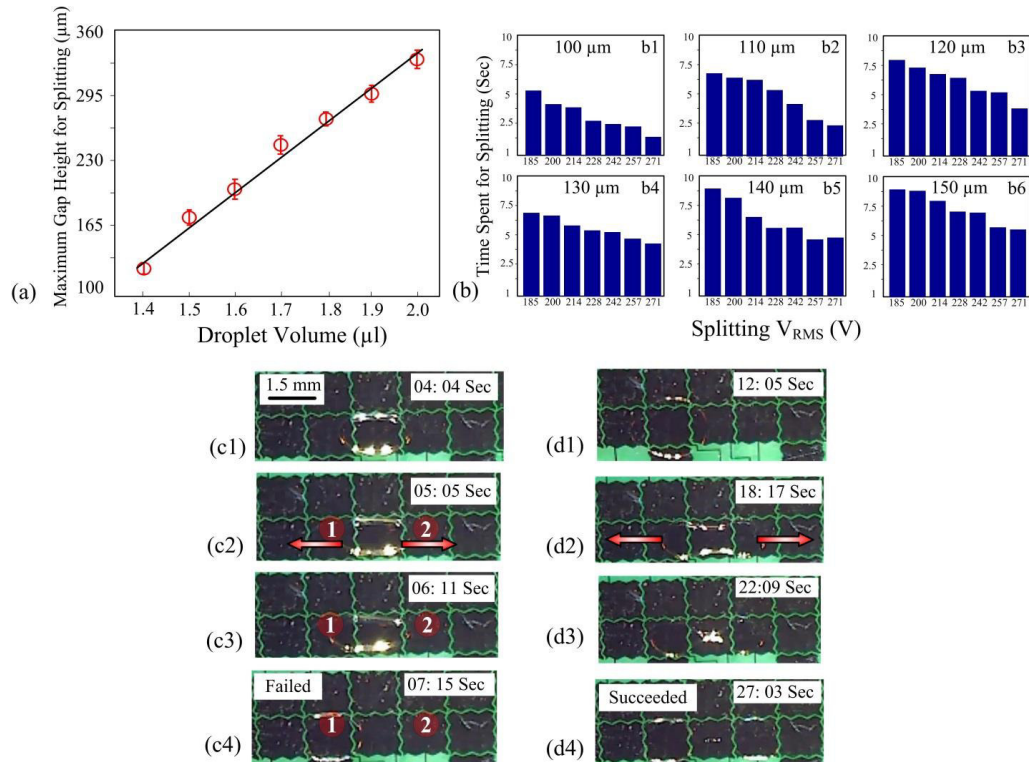
Fig. 3.36 (a) The largest splitting gap heights for the droplets ranging from 1.4 µl to 2.0 µl. (b) Various applied splitting voltages and their time spent for splitting a 1.5 µl droplet at $100 - 150$ µm gap height. (c1-c4) It failed to split a 1.5 µl droplet at 200 µm gap height. (d1-d4) It succeeded to split the same 1.5 µl droplet at 75 µm gap height.

The minimum gap height is set by a tape as the spacer (50 µm). The PZT plate is carefully attached onto the top plate at one end and fixed onto the bonding posts at the other end. This is the 50 µm displacement point that should be calibrated with the laser displacement sensor. The liquid is added to the big reservoirs externally from the left and the right edges of the chip using a pipette without moving the top plate. The smallest droplet that can be dispensed from the

reservoir is around 0.1 µl at the lowest gap height (50 µm). Double the gap height, the theoretical dispensed droplet volume is doubled as well.

When the to-be-split droplet is ready on the DMF chip, it is settled in the middle of an electrode and the left and right boundaries should overlap with the neighboring electrodes. First, the gap height is adjusted to a reasonable level for the splitting (make sure there are overlaps with the splitting droplet). If the splitting operation failed, then lower the gap height by 10 µm; if the splitting succeeded, then increase the gap height by 10 µm and try to split it again. To simplify this experiment, we have the splitting electrodes controlled by three external buttons so we can control the splitting and actuation and complete the test quickly. Since we found out low voltages require a longer time to split a droplet during the experiment, we tested the droplet splitting time with different voltages (185-271 V_{RMS}) and different gap heights. The splitting time was recorded.

The droplet shown in Fig. 3.36 (c1-c4) is small relative to the gap height (200 µm) for a proper split operation. After experiencing forces from each electrode the droplet is actuated by electrode '1' rather than split by electrode '1' and '2'. The reason of this failure is that the gap height is too large for the droplet and the footprint areas on the split electrodes (electrode '1' and electrode '2') are too small to be balanced. Decreasing the gap height can increase the footprint areas on electrode '1' and '2'. With a larger footprint area, the droplet is split successfully (Fig. 3.36 (d1-d4)).

A droplet in a certain volume can be split with multiple gap heights. However, larger gap heights may increase the splitting time. Increasing the applied splitting voltage may expedite the splitting process. A 1.5 µl droplet is tested for the splitting time with various applied voltages (Fig. 3.36 (b)). For a 100 µm gap height, using 271 V_{RMS} can save the splitting time for more

than 3 seconds than using 185 V_{RMS}. Using larger voltages for splitting can guarantee efficient splitting operations.

The peripheral hardware is implemented using integrated circuits and PCB boards. Therefore, the proposed system is portable. Compared to the conventional DMF peripheral hardware, the bench equipment such as the function generator and the high power voltage amplifier are avoided in this study. Instead, a portable MOSFET array is integrated into the control circuit. Other peripheral hardware such as the first and the second stage amplifiers, and ADC / DACs are all integrated circuits (IC chips) which are small in size. The system structure shown in Fig. 3.26 shows the modular design of the DMF control system. All the modules are simply integrated into PCB boards. The laser sensor is integrated in a 1.5 inches by 3 inches box (the manufactural design), which can be easily mounted to a fixture above the DMF chip. The DMF chip and the operated liquid can be accessible without touching the PZT mounted top plate once it is well calibrated. For the next generation, the system can be improved by adding a flexible microscopic stage and integrating all the hardware into a portable box.

There are some limitations about the vibration amplitude. It was reported that the voltage applied to the electrode makes the Teflon coated hydrophobic surface more wettable and indirectly holds the droplet downwards and detaches the droplet from the top plate (Gong, Cha, Ju, & Kim, 2008). The electrowetting-induced detachment happens when the top plate height is comparable to, or higher than the droplet pitch. We tested the droplet detachment in our EWOD system with different droplet volumes, which indicates the top plate vibration amplitude limitations in the future applications (Fig. 3.37). 250 V_{RMS} voltage pulses are used for the detachment test. The detachment gap height in Fig. 3.37 (b) shows both the detaching point with and without a voltage applied to the electrode. The droplet under electrowetting has a lower

detaching point. In the regular top plate vibration operations in this study, the gap height and vibration amplitude is much lower than the vibration limit presented in Fig. 3.37. For example, for a 0.5 µl droplet, the detachment happens at > 500 µm, but the largest possible gap height with vibration is 300 µm in our study (limited by the PZT material). High gap height lowers the aspect ratio of the droplet which impacts on the actuation velocity, so there is no motivation for the user to apply "large" vibration amplitude to the top plate.
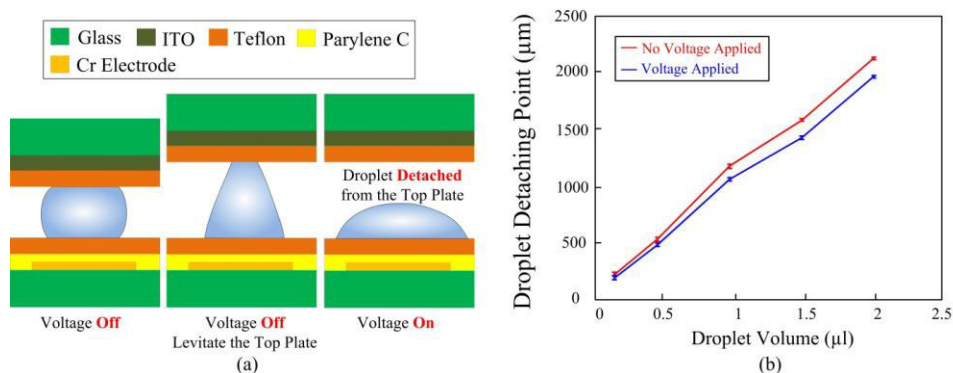
Fig. 3.37 The top plate vibration has limits in amplitude to avoid the droplet detaching from the top plate. The droplet spreads on the surface when there is a voltage applied, if the gap height is large, the bridge between the droplet and the top plate will be broken and the droplet will be detached from the top plate.

3.4.4. Conclusion

A new intelligent EWOD DMF top plates mounting technique is proposed and tested in this chapter. Through gap height control dispensing volume can be modified in real time. In addition, splitting into smaller droplets is possible. Compared to other micro liquids sensing and actuating techniques such as substrate vibration and SAWs, the top plate vibration technique is compatible with digital controlled EWOD microfluidic chips. The droplet actuation velocity can be sped up to 3 times faster than using static top plates. Much lower threshold actuation voltage is achieved

by using a vibrating top plate. With the dynamic control of the top plate, the droplet actuation in the air-filled EWOD DMF chips is more reliable, therefore no oil environment is needed for the real point-of-care diagnostics, which makes the EWOD DMF chips more practical for clinical applications.

Future work can focus on extending the techniques for high throughput automated micro droplet dispensing and transportation. Droplet volume can be tested by embedding a capacitive sensor in the system. The top plate height can then be automatically set depending on the droplet volume. Top plate vibrations and gap height control provide a way to efficiently optimize the droplet operations without introducing any nano-fabrication processes. By introducing mechanical vibrations, precise positioning of the top plate and capacitive sensing for feedback control into DMF, clinical point-of-care applications using EWOD DMF can be more accurate and useful.

Chapter 4 EWOD DMF chip surface characterization

Based on the studies in Chapter 3, we know that the contact angle hysteresis in the air ambient is significant. The hysteresis has been a major problem to achieve DMF's desired reliability (F. Li & Mugele, 2008). For more than 100 years, scientists have been fascinated with vibration induced droplet motions (Borcia, Borcia, & Bestehorn, 2014; Rayleigh, 1879). Vertical and horizontal harmonic vibration of the supporter can break the balance of the droplet and induce a liquid movement. The oscillating magnitude, frequency and phase dominate the vibration induced behaviors (Borcia et al., 2014). Different from the external substrate vibration, more powerful internal droplet oscillations can be created by surface acoustic waves (SAWs) (Alvarez, Friend, & Yeo, 2008; Alvarez, Yeo, Friend, & Jamriska, 2009; Bhattacharjee, McDonnell, Prabhakar, Yeo, & Friend, 2011; J. Friend & Yeo, 2011; J. R. Friend, Yeo, Arifin, & Mechler, 2008; Hodgson, Tan, Yeo, & Friend, 2009; H. Li, Friend, Yeo, Dasvarma, & Traianedes, 2009; Yeo & Friend, 2009). However, the major concerns of using SAWs as actuators are the unpredictable rapid fluid flow and integration issues of the vibration source with the silicon and glass substrates in EWOD (Yeo & Friend, 2014). Substrate vibration was used to actuate a droplet on a surface with chemically wettability gradient (Daniel et al., 2004). A promoted droplet motion on a chemical gradient surface is realized by controlling a sandwiched structure which is similar to the popular DMF topology. In Daniel's study, a droplet ratchet-like motion is observed by continuously squeezing and relaxing the droplet. The contact line was depinned during the vibration and moves to the surface with lower interfacial energy. In electrowetting, a double layer of charges near the liquid-solid surface is formed by the electric field applied to the electrode (Quinn et al., 2003). The charge double layer lowers the surface energy which helps spread the liquid on the surface. Therefore, it is possible to use top plate

vibration to overcome the surface hysteresis and lower the actuation voltage. In this chapter, the Teflon surface is characterized on its hysteresis. The mechanisms of the actuation velocity and the driving voltage improvements by using the dynamic top plate are discussed; Both parallel and non-parallel (beak-like) top plate are used for this study.

4.1 Droplet transportation in a beak-like EWOD DMF device

4.1.1 Introduction

It is known that phalaropes use water droplet surface tension to capture their prey particles by their beaks and get them to move up against gravity along the bill (Rubega & Obst, 1993). Phalarope's beak behaves similar to a tweezer that is tweezing a small droplet that is smaller than the typical capillary length (several millimeters). Continuously closing and opening the tweezer will propel the droplet into the wedge. Inspired by this bionic technique, a droplet self-propelled artificial bill was developed (Bush, Peaudecerf, Prakash, & Quéré, 2010; Heng & Luo, 2014; Luo, Heng, & Xiang, 2014; Prakash, Quere, & Bush, 2008). It was denoted that the droplet bounded in the tweezer has a front contact angle (θ_{front}, into wedge) larger than the receding contact angle (θ_{rear}, out of wedge). While squeezing the bounded droplet, the front contact angle reaches the advancing angle θ_a first, so the front contact line advances into the wedge while the receding contact line is still pinned. When the tweezer relaxes the receding contact angle reaches the receding contact angle θ_r while the advancing contact line is pinned. The result is ratchet-like droplet movement. This movement is also called rectified droplet movement (Buguin, Talini, & Silberzan, 2002; Noblin, Kofman, & Celestini, 2009). A sequential squeezing and relaxing of the droplets releases the front and rear contact line and allows the droplets to experience various metastable states resulting in easier actuation (Daniel et al., 2004; Longley et al., 2012). Generally, the artificial bill is nothing but a chamber that has non-parallel boundaries. The front

edge of the bounded droplet is bearing a larger Laplace pressure than the rear edge. This differential pressure pushes the droplet into the wedge. Similar structures such as a tapered tube (Renvoisé, Bush, Prakash, & Quéré, 2009) and a wedge-like vertical container (Baratian et al., 2015) have behaviors dominated by this feature. Interestingly, to provide more propulsive force, more perturbations have been added to this beak-like structure using AC voltages (Baratian et al., 2015; J. Hong, Park, Koo, Kang, & Suh, 2013). The voltages are applied to the two homogeneous plates (all-in-one electrode) at the same time. The applied voltage breaks the balance of the contact line friction and the net forces, and thereby the droplet dynamic states can be controlled by turning on/off the applied voltage instead of vibrating the two plates. However, using homogeneous electrode can only achieve two states, 'on' and 'off', which are open-loop binary states and the droplet movements and positions cannot be controlled and predicted. Another possible perturbation to the non-parallel chamber is adding chemical gradient to the surface to continuously grade the wettability along the actuation path (Daniel et al., 2004; Daniel et al., 2001; Longley et al., 2012). The gradient surface and substrate vibrations lead to a droplet ratchet-like motion toward the region of higher wettability (Longley et al., 2012). However, the heterogeneous gradient is unchangeable once fabricated on the surface, which means the droplet motions are passively directed to the pre-designed gradient.

Electrowetting on dielectric (EWOD) digital microfluidics (DMF) is one of the most promising lab-on-a-chip techniques that have friendly interfaces to computers and microcontrollers. EWOD DMF chips can be fabricated on low-cost substrates such as a glass (Ng et al., 2012; Ng et al., 2015), a printed circuit board (PCB) (Abdelgawad & Wheeler, 2007; Abdelgawad & Wheeler, 2008; Gong, 2008; Y. Li et al., 2014), a polyimide film (Kirby & Wheeler, 2013) and paper (Fobel et al., 2014). As the cost and size of the DMF chip decreases,

the EWOD system can be integrated with portable electronics for point-of-care diagnostics (Ng et al., 2010; Ng et al., 2012; Ng et al., 2015). Complex droplet operations such as splitting (Cho et al., 2003), position detection (Y. Li et al., 2015), droplet composition identification (Y. Li et al., 2014; Schertzer et al., 2010) and volume controlled dispensing are all possible on a DMF chip (Gong, 2008; Ren et al., 2004). Droplet motion in an EWOD device filled with an oil environment is smooth and fast (T. Chen et al., 2014). It is much more challenging to realize the droplet actuation, merging and splitting in an air environment rather than in an oil environment. Dust particles randomly deposited onto the chip may increase the chance of contact line pinning of the droplet during the operation. The oil environment in the EWOD chip, to some extent, is more tolerant to dust. Also, without an oil environment, the two major microfluidic kinetic resists, the contact line pinning and contact angle hysteresis (CAH), become much more significant to prevent the droplet from being actuated. However, the clinical diagnostics requires a clean environment for chemical reactions. Once the droplet is operated in air, the contact line pinning and contact angle hysteresis (CAH) becomes significant and can even result in actuation failure. Increasing the driving voltage can overcome the hysteresis and trigger the droplet motion; however, the dielectric material can breakdown with a high voltage before the droplet gets actuated. A gentler perturbation is required to release the pinned contact line during experiments.

A beak-like structure and top plate vibrations look promising for this purpose. The vibrations can be added to the top plate of the EWOD system to stretch and squeeze the droplet to cancel the pinned contact line. The non-parallel beak-like substrates can provide a Laplace pressure gradient to propel the droplet along the path. The well-controlled EWOD device may get more power by the pressure gradient and a speed up during actuation.

To demonstrate this hypothesis, an EWOD substrate is developed using both parallel and non-parallel top plate. Droplet actuation speed is measured under these different circumstances. An optimized configuration using these speed-up techniques is discussed.

4.1.2 Materials and methods

The DMF chip is fabricated at the cleanroom facility of Nevada Nano Technology Center. The lithography process is the same as previously described (section 3.4.2).

The on-chip chromium pins are connected to stranded wires using silver conductive epoxy. The top plate ITO side is grounded all the time for proper droplet operations. A high voltage module purchased from EMCO (EMCO F40, Schweiz, Switzerland) is used as the high voltage source to provide the driving voltages to the PZT chip and the EWOD electrodes. The great benefit of using EMCO and the simple CMOS gate arrays as the EWOD driving circuit is saving the space of using bench function generators & amplifiers. A modular design is introduced to the EWOD system. The EWOD electrode control system is integrated into two portable modules; one is the relay array, the other one is the control hub. The EWOD chip is mounted on a PCB platform and connected to the relay array module with standard flexible flat cables (FFC). EWOD electrode driving voltages are obtained from the drains of the high-voltage CMOS transistors. Various frequencies of the actuating voltage can be obtained by toggling the gates of the transistors with different rates (pulses at 10 kHz and various voltages). A high speed camera (1000 fps, Casio ZR200, Japan) and a handled digital microscope (Celestron, CA) are used to capture the droplet motion and measure the instantaneous velocity. Open source software ImageJ and Tracker are used to measure the droplet contact angles.

4.1.3. Results

A two dimensional geometrical model of a droplet bounded between a beak-like EWOD device is shown in Fig. 4.1. l_x is the length of the droplet, l_a is the distance of the front contact line to the vertex of the angle. Keeping the bottom plate flat α is the top plate angle. The non-parallel EWOD device is not drawn in scale for clearly presenting the angles. The contact line becomes slippery during continuous compression and extension of the droplet body by the top plate. It is assumed that both the front and the rear contact lines are wetting the substrate surface (Fig. 4.2).
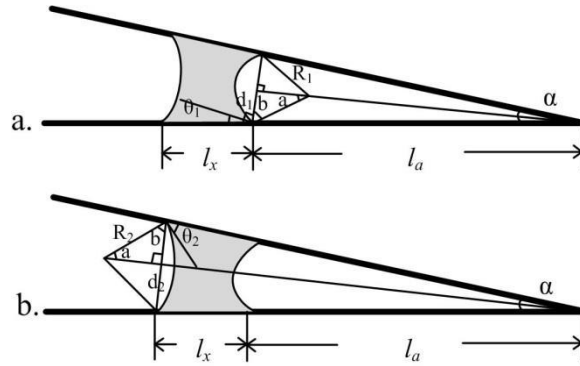
Fig. 4.1 A two dimensional geometrical model of a droplet bounded between a beak-like EWOD device.

$$l_a \cdot sin\frac{\alpha}{2} = d_1 \tag{4.1}$$

$$R_1 \times cosb = d_1 \tag{4.2}$$

$$\frac{\pi}{2} - \theta_1 = c \tag{4.3}$$

$$a = c + \frac{\alpha}{2} \rightarrow a = \frac{\pi}{2} - \theta_1 + \frac{\alpha}{2} \tag{4.4}$$

$$b = \frac{\pi}{2} - a \rightarrow b = \theta_1 - \frac{\alpha}{2} \tag{4.5}$$

$$l_a \times sin\frac{\alpha}{2} = R_1 \times \cos(\theta_1 - \frac{\alpha}{2}) \tag{4.6}$$

using the similar method, we get:

$$(l_a+l_x) \times sin\frac{\alpha}{2} = R_2 \times \cos(\theta_2 + \frac{\alpha}{2}) \tag{4.7}$$

then the Laplace pressure is:

$$P_{l1} - P_a = \frac{\gamma \times \cos(\theta_1 - \frac{\alpha}{2})}{l_a \times sin\frac{\alpha}{2}} \tag{4.8}$$

$$P_{l2} - P_a = \frac{\gamma \times \cos(\theta_2 + \frac{\alpha}{2})}{(l_a+l_x) \times sin\frac{\alpha}{2}} \tag{4.9}$$

We have very small α in the experiments seen in Fig. 4.1 so the differences between θ_1 and θ_2 are negligible. If follows that $P_{l1} - P_a > P_{l2} - P_a$, which results in an unbalanced net force that pushes the droplet into the wedge. However, the droplet is not necessarily going to move in such a non-parallel structure. Viscous friction and Poiseuille resistance prevents the droplet from moving (Bush et al., 2010).

Note that this study is different from the EWOD device with homogeneous electrodes (J. Hong et al., 2013; Luo et al., 2014). The bottom substrate developed here is an array of digital EWOD electrodes. Droplet positions can be well controlled by the electrodes. If $\alpha \rightarrow 0$, which means the two substrates are parallel with each other, the droplet won't move if there is no wettability gradient on the bottom substrate. An inclined PZT cantilever structure can be used to control the beak-like top plate vibration. The cantilever structure has one end fixed and the other end loaded with the top plate. A 0-200 V triangle wave can be used to drive the PZT vibration. The opening angles can be measured using ImageJ.
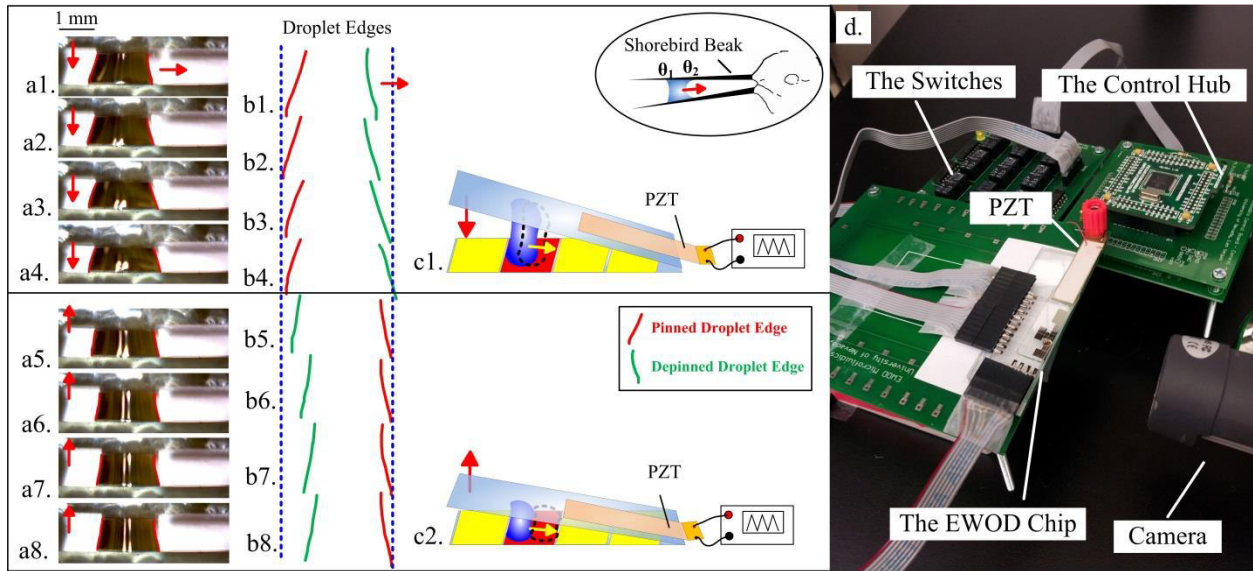
Fig. 4.2 A ratchet-like motion cycle of a 4 µL droplet in a non-parallel EWOD device. (a1-a8) A droplet bounded by a shorebird's beak and moves into the wedge with non-parallel top plate vibration. (b1-b8) The corresponding left (rear) and right (front) edges of the droplet in a1-a5. (c1 and c2) Illustrations of the EWOD system with non-parallel substrates and the EWOD model to mimic the shorebird beak to bound a droplet. A PZT chip is used to create a beak-like vibration (not drawn to scale). (d) The system setups.

Note that for a hydrophobic surface (Teflon AF coated) in this study, the advancing angle θ_a' of a DI water droplet is larger than the advancing angle θ_a on a hydrophilic surface. The 4 µL sessile droplet initially bounded into these two Teflon AF coated surfaces has a front contact angle of 120°. It is not easy to form a ratchet-like motion on a hydrophobic surface. When the surface becomes slippery, the contact angle hysteresis is small, so the differences between advancing and the recedeing contact angles are small. When squeezing the droplet using the top plate the advancing and the receding contact angles increase at the same time and reach the advancing angle θ_a' almostly at the same time. So the front and the rear contact lines are depinned almost simultaneously. The droplet will oscillate at the same position but without

111

moving into the wedges or out of the wedges. While the droplet is on the wetting the surface the front contact angle reaches θ_a much earlier than the rear contact angle. In this case, the front contact line advances while the rear contact line remains pinned in the same position. When relaxing the droplet the rear contact line advances and the front contact line remains pinned (Fig. 4.2 b1-b8). This is a ratchet-like motion. In a digital EWOD device, the substrates surface are coated with hydrophobic materials to increase the contact angle changes when voltages are applied. Even the free ratchet motion induced by the top plate vibration is not desirable during opearation. This physical phenomenon is also demonstrated in this study. The ratchet motion is tested with a droplet confined to one electrode. When the electrode under the droplet is turned on the droplet starts wetting the surface and has a large contact angle change ($< 25^{°}$ at 400 V). At this time the top plate compression depins the front contact line but not the rear contact line. Inversely, the extention of the top plate actuates the rear contact line but not the front contact line (Fig. 4.2). Since the next electrode is not activated, no more motion is created. However, the droplet moves from the left side of the electrode to the right side. This subtle motion is demonstrated by extracting the outlines of the droplet in one vibration period and putting them in a vertically aligned column (Fig. 4.2 (b1-b8)). If the droplet is not wetting the surface there is no horizontal displacement observed (Fig. 4.3). Instead, the droplet oscillates in the same spot.
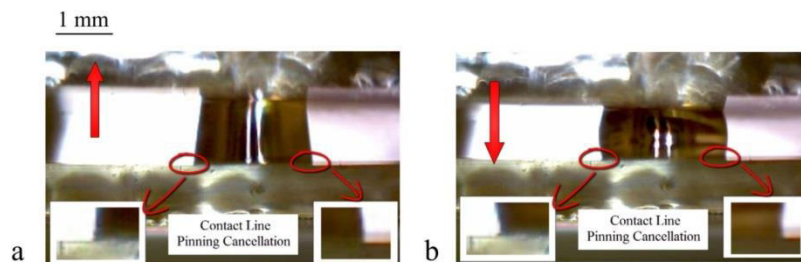
Fig. 4.3 A 4 µL DI water droplet in a non-parallel EWOD device. Zoomed-in subfigures show the evidences of the depinned contact line.

An interesting hysteresis of the contact line depinning is observed (Fig. 4.3). When the droplet starts being squeezed by the top plate, the contact line does not move immediately. It remains pinned on the substrate surface. Squeezing the droplet further will depin both the front contact line and the rear contact line. It's been shown that a sessile DI water droplet on a slippery surface is hard to form a ratchet-like motion with top plate beak-like vibrations; however, on a wetting surface (wetted with voltages), the droplet is depinned by the beak-like vibration and moves toward the path of global energy minima. Note that the wetting voltage is applied only to the electrode underneath the droplet in this study (Fig. 4.4). If the neighboring electrode is activated, a dramatic asymmetrical wetting is induced at the front and the rear contact line, which will cause a conventional digital EWOD actuation which has been extensively studied (Fair, 2007). In this study, we implement the beak-like top plate vibration during the actuation in order to reduce the impact of the contact line friction on the droplet and increase the propulsive energy.

The total force that dominates the droplet motion can be described as (C. Chen et al., 2011; Yafia & Najjaran, 2013):

$$F_t = F_d - F_s - F_f = F_d - 2\pi r^2 \frac{6\mu U}{h} - 4\pi r U \tag{4.10}$$

where F_t, F_d, F_s, F_f and F_c are the total force, driving force, shear force (from the two plates), the friction force and the contact line friction; r, μ, U and h are the droplet radius, viscosity, velocity and height. Low gap height increases the opposing forces F_s and F_f. The driving force F_d is a variable which will be introduced later. For the same droplet, while stretching the droplet by increasing the opening angle, the droplet radius decreases and the opposing forces may decrease. As a result, a larger gap height due to an increased opening angle will increase the

minimum actuation voltage (the threshold) and also speeds up the droplet at the same time. Four different top plate angles are tested in this experiment (Fig. 4.4).
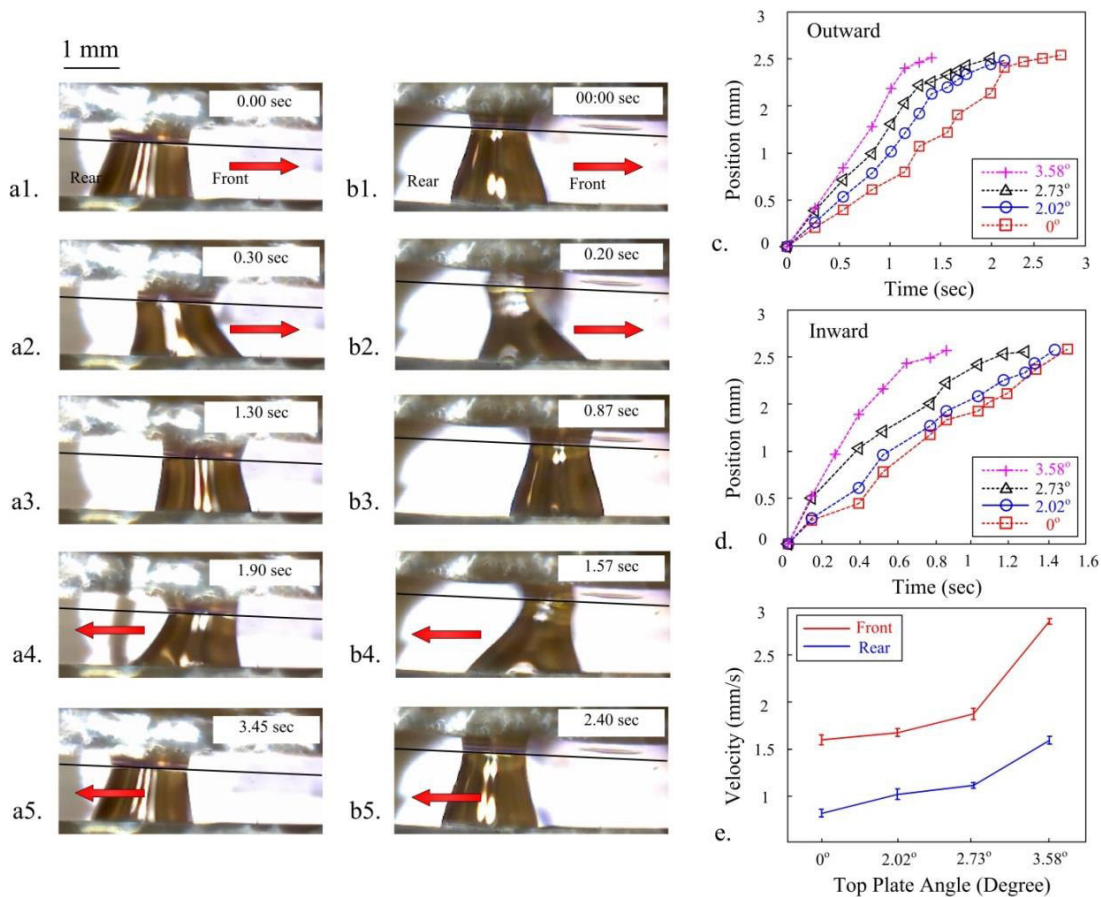
Fig. 4.4 A 4 µL DI water droplet is actuated between two EWOD electrodes at a top plate opening angle of 2.02^o (a1-a5), 3.58^o (b1-b5). No vibrations added to the top plate.

In the inclined top plate device, the droplet moves into the wedge much faster than it moves out of the wedge (Fig. 4.4 c and d) which indicates Laplace pressure gradient accelerates the droplet while it is being actuated. The droplet velocity profile is in a similar shape to a logarithmic diagram. This makes sense because the droplet gains an increasing acceleration at the beginning and arrives at a velocity peak in a short time. As the displacement to the target electrode increases, the opposing forces in Eq. 4.10 increases and the droplet slows down. The

average velocity is calculated by dividing the massive center displacement by the time consumed. As shown in the beginning of this study, the beak-like vibration can depin the droplet contact line of sessile droplets. So we hypothesize the droplet velocity can be improved further by introducing the top plate beak-like vibration.

The droplet net force can be represented by the capacitive energy stored in the dielectric material coatings (Baird, Young, & Mohseni, 2007). The capacitance distribution and the geometric structure are modeled in Fig. 4.5.
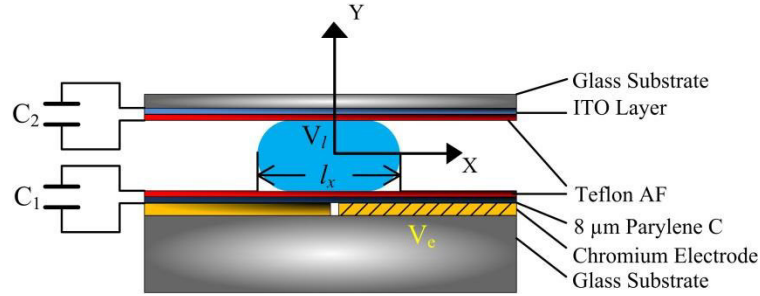
Fig. 4.5 Capacitance and geometrical model of a droplet in EWOD device.

C_1 and C_2 are the bottom and top dielectric material capacitances while V_1 and V_2 are the liquid voltage and the electrode voltage. The length l_x is the length of the droplet and x is the distance that the droplet moves to the right side of the device. Then the liquid voltage can be described as:

$$V_1 = \frac{C_1 V_2}{C_2 + C_1}\left(\frac{x}{l_x} + \frac{1}{2}\right)$$ (4.11)

$$E = \frac{1}{2}C_2 l_x V_1^2 + \frac{1}{2}C_1\left(x + \frac{l_x}{2}\right)(V_2 - V_1)^2 + \frac{1}{2}C_1\left(\frac{l_x - x}{2}\right)(-V_1)^2$$ (4.12)

substituting Eq. 4.11 into Eq. 4.12, we get:

$$E = \frac{1}{2}V_2^2\left(\frac{x^2(C_2 - C_1)}{l_x} + C_2 x + \frac{l_x(C_2 - C_1)}{4}\right)$$ (4.13)

115

The net force is obtained from differentiating the system energy in the x direction:

$$F_x = \frac{\partial E}{\partial x} = 2l_x V_2^2 (8(C_2 - C_1)x + l_x^2 C_1 + (l_x + 4)C_2) \qquad (4.14)$$

where $C_2 \ll C_1$, so $C_2 - C_1$ is negative. From the equation above, we know that the net force is created linearly with the distance x. The droplet jumps out from the original spot and reaches an acceleration extremum. Then it slows down as moving to the target electrode because the net force F_x becomes smaller than the frictions that pulling the droplet backwards.

As the ratchet-like motion is random and uncontrollable, digital microfluidics is used to avoid this issue. There is no horizontal displacement under beak-like top plate vibration if no voltages applied. The top plate vibration amplitude is large enough to create contact line pinning and depinning cycles. The droplet gets more chances to adjust its states to move forward in the direction that has a minimum global energy. At the same time, the droplet motion is still controlled by the digital activation. When the top plate is vibrating at low frequencies (~1Hz) which are comparable to the droplet velocity, it is possible to optimize the operation velocity further by modify the vibration phase. As previously demonstrated, the front contact line advances when squeezing the droplet. If the advancing electrode is triggered while the top plate starts squeezing the drop, then the squeezing behavior will help moving forward the front contact line and speeding up the actuation. While the front contact line of the droplet reaches the advancing electrode the relaxation of the top plate will help pull the rear contact line forward. However, for high-throughput droplet operations in our EWOD chip, the droplet can move very fast in an air environment. It is more practical to turn on the top plate vibration at all times during the operation and at a relatively higher frequency (5-20 Hz). The angle between the top plate and

the bottom plate should be in the range of $0^o - 5^o$ (with a 4 µL DI water droplet). A larger opening angle will disconnect the bridge of the droplet and the top plate.
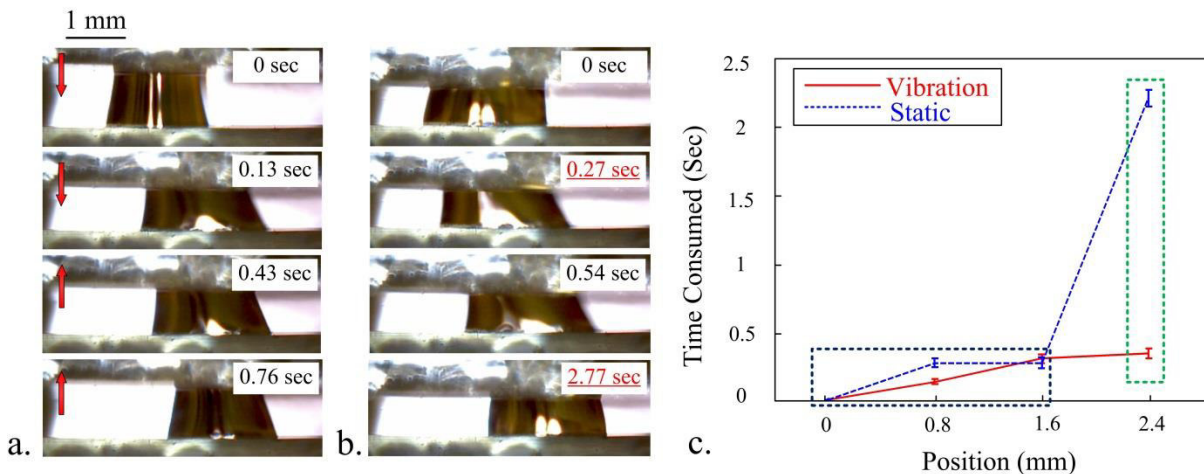
Fig. 4.6 a. Droplet actuation under a top plate vibration in low frequencies (1 Hz). b. Droplet actuation under a static top plate. c. Time consumed between the four positions on the EWOD chip.

When the top plate frequency and the droplet actuation velocity are comparable with each other, the squeezing behavior expedites the front contact line. The opening top plate speeds up the rear contact line to move the droplet into the wedges (Fig. 4.6). The sequential snapshots of the droplet positions show the most significant velocity improvement occurs at the beginning and the ending of the actuation. The red font seen in the right top corner of the four subfigures in Fig. 4.6 b indicates the significant slower movements compared to the subfigures in Fig. 4.6 a. This experiment reveals that the exact phases of the droplet are sped up by the top plate vibration (Fig. 4.6 c). When the Maxwell stress pushes the droplet forward, the front contact line is actively dragged by the advancing electrode underneath; however, the rear contact line does not have any overlap with the activated electrode. The surface tension at the rear contact line resists the rear edge to move forward. The relaxing of the top plate translates the surface tension at the droplet-

top plate interface to a body force which depins the rear contact line. So a very significant velocity improvement is observed in Fig. 4.6 c at the position of 2.4 mm. The liquid droplet with a large viscosity will leave a long tail when moving on a surface. In dynamic top plate system, the passive movement of the tail is pulling into the wedge due to the body force created by relaxing the droplet.

4.1.4. Conclusion

A brand new EWOD DMF device droplet perturbation method is developed in this study. Different from the previous contact line pinning cancellation methods, such as vertical and horizontal substrate vibrations (Borcia et al., 2014; Rayleigh, 1879) and surface acoustic waves (SAWs) (Alvarez et al., 2008; Alvarez et al., 2009; Bhattacharjee et al., 2011; J. Friend & Yeo, 2011; J. R. Friend et al., 2008; Hodgson et al., 2009; H. Li et al., 2009; Yeo & Friend, 2009), PZT deflection induced top plate vibration can be well controlled by electronics. For a DI water droplet on a Teflon coated hydrophobic surface, the beak-like vibration does not create any undesired ratchet motion. Rather, it is capable of depinning the droplet contact line. The beak-like top plate opening angle affects the droplet velocity by changing the gap height and the droplet effective length. The droplet moves about 2 times faster into the wedge than it moves out of the wedge. The non-parallel top plate structure creates a Laplace pressure deviation between the droplet front edge and the rear edge which accelerates the droplet further during EWOD voltage triggered actuation. When the top plate is vibrating in a comparable (or larger) velocity with the droplet, the details of how the vibration improves the actuation can be observed. The most significant velocity improvements occur at the beginning and the end of the one-step actuation.

The beak-like top plate montage is implemented using a PZT plate cantilever structure. A gentle perturbation is introduced without adding any nano-fabrication process. This newly developed technique may be used for EWOD DMF device droplet movement optimization and further for the point-of-care clinical diagnostics.

4.2 Droplet transportation under subthreshold voltages in digital microfluidics with top plate vibrations

4.2.1 Introduction

The electrowetting on dielectric (EWOD) digital microfluidic (DMF) chip is popular as a droplet level versatile lab-on-a-chip solution for actuating, merging, dispensing, and splitting droplets with fine-time resolution (K. Choi, Ng, Fobel, & Wheeler, 2012; Gong, 2008; Wheeler et al., 2005). However, in an air ambient occasionally a droplet is 'stuck in place' during actuation. This issue has been a limiting factor in the commercialization of DMF chips using EWOD. The surface heterogeneity of an EWOD system results in droplet contact angle (c.a.) hysteresis at the liquid-solid interface (F. Li & Mugele, 2008; Mugele, 2009; Murade, van den Ende, & Mugele, 2011). Contact angle hysteresis induces undesired pinning forces that resist the droplet actuation. In a DMF (digital microfluidics) lab-on-a-chip system, a minimum threshold voltage V_{TH} (the critical voltage) is required to provide sufficient electrostatic forces to overcome the drop's pinning force. However, c.a. saturation and the dielectric material physical property limit the effectiveness of simply increasing the magnitude of the driving voltage (Mugele & Baret, 2005) for a stronger driving force. Some successes have been achieved to reduce the resistive force, such as using bottom substrate mechanical vibrations (Brunet, Eggers, & Deegan, 2007; Daniel & Chaudhury, 2002; Daniel et al., 2004; Daniel, Chaudhury, & De Gennes, 2005), AC-induced droplet oscillations (J. Hong et al., 2013; F. Li & Mugele, 2008), oil fillers (Baratian

119

et al., 2015; T. Chen et al., 2014), tapered chambers (Baratian et al., 2015; J. Hong et al., 2013; Renvoisé et al., 2009), and surface acoustic waves (Y. Li, Fu, Brodie, Alghane, & Walton, 2012; Yeo & Friend, 2014). In this section, we propose a new freedom of perturbation using top plate vibrations. In a EWOD DMF device, the target electrode is applied with a voltage that changes the wettability of the surface, which is known as "electrowetting". It was first identified by Greenspan (Greenspan, 1978) that a droplet placed on a chemically heterogeneous surface moves to the region of higher wettability to reduce the interfacial free energy, and experimentally demonstrated by Daniel (Daniel et al., 2004; Daniel et al., 2001) on a vibrated substrate with a chemical wettability gradient. Electrowetting modifies the wettability of the surface with a voltage gradient instead of using a chemical gradient (Daniel et al., 2004; Daniel et al., 2001). If the voltage gradient is weak (subthreshold voltages), the droplet actuation won't occur. The "top plate vibration" used in this study can trigger the droplet actuation under a subthreshold voltage. The voltage gradient is applied to the start and the target electrodes; the droplet bridges the two electrodes has an asymmetrical c.a. hysteresis at the front and the rear contact line. The surface above the front electrode is more wettable and the successive pinning and depinning of the contact line allows the drop to sample various metastable states and setting it to the path of global energy minima (Daniel et al., 2004).

4.2.2 Materials and methods

The DMF electrodes used in this study are patterned on a Chromium coated glass slide. The dielectric layer is an 8 µm parylene C that is coated onto the EWOD chip by a chemical adhesion process. The top plate is an ITO (Indium-Tin-Oxide) coated glass slide followed by a 250 nm Teflon AF layer. This layer is spin coated onto the chip so that the top plate is hydrophobic. Piezoelectric (PZT) bimorph actuators are used to control the top plate height; Laser

displacement sensor (Z4M-S40, Kyoto, Japan) and its manufactural amplifier (Z4M-W40, Kyoto, Japan) are used to monitor the PZT deflection and the top plate displacement. MOSFET toggling circuits are used to generate the EWOD driving voltages. Contact angles are measured using ImageJ and curve fitting.
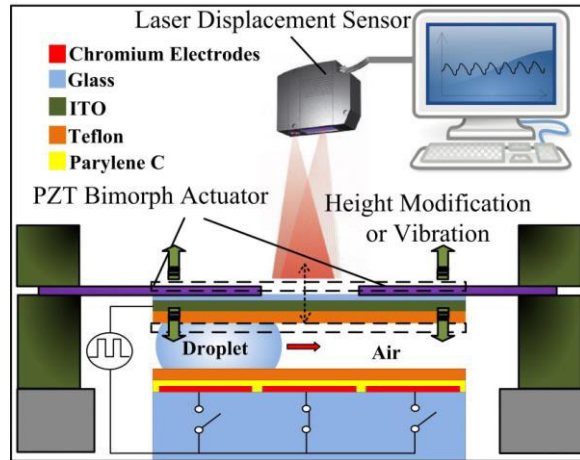
Fig. 4.7 The proposed EWOD DMF system is mounted with a PZT cantilever controlled dynamic top plate and its displacement measurement system.

The gap height is monitored using an in-house GUI software coded with MATLAB. The deflection of the PZT chip is controlled by a potentiometer. A high speed camera (1000 fps, Casio ZR200, Japan) and a handled digital microscope (Celestron, CA) are used to capture the droplet movement. The droplet motion is analyzed by tracking the displacement of the front and the rear contact lines in the time-domain using Tracker (NSF Open Source Physics).

In an open system, the c.a. hysteresis can be measured by gradually injecting/ejecting small amounts of liquids into/from a sessile drop on the surface (F. Li & Mugele, 2008). If the droplet is confined between two plates, the c.a. may vary with the gap height (S. Hong, Chou, Chan, Sheng, & Tsao, 2012). We assume the advancing c.a. and the receding c.a. can be measured by compressing and relaxing the droplet using the top plate. The voltage-dependent c.a. that

measured in both single plate and dual plate systems are presented in Fig. 4.8. The theoretical c.a. is calculated from the classic electrowetting equation: $cos\theta = cos\theta_Y + \varepsilon_0\varepsilon_d U^2/2d\sigma_{lv} = cos\theta_Y + \eta$. θ_Y is Young's equilibrium contact angle, ε_d is the dielectric constant of the insulation layer, d is the thickness of the insulation layer, σ_{lv} is the liquid-vapor surface tension, U is the applied voltage. When the applied voltage increases, the c.a. decreases very quickly until it is saturated. For typical values: $\sigma_{lv} = 0.072\, J \cdot m^{-2}$ and the dielectric material layer thickness is $d = 8\, \mu m$. Using DC voltages, the experimental contact angle agrees very well with the theory until the electrowetting number is greater than 0.8, which indicates the c.a. saturation. The c.a. measurement using the conventional sessile drop method agrees well with the proposed dual-plate confined droplet method seen in Fig. 4.8 (a). Additionally, the differences between the advancing c.a. and the receding c.a. under AC voltages gradually diminish as the electrowetting number increases. It is shown in Fig. 4.8 (a) that the c.a. hysteresis is eliminated when the electrowetting number is greater than 0.3. Voltage magnitude dependent c.a. hysteresis is shown in Fig. 4.8 (b) (f = 1 kHz). The c.a. hysteresis decreases to a small level (< 5°) when the applied voltage is greater than 120 V$_{\text{RMS}}$. When the voltage is smaller than 40 V$_{\text{RMS}}$, the c.a. hysteresis doesn't change significantly. The voltage within the pink zone in Fig. 4.8 (b) can maintain a proper asymmetrical c.a. hysteresis for the ratchet-like motion described below.

4.2.3 Results

The experimental results shown in Fig. 4.8 are used to characterize the c.a. hysteresis of a confined droplet in a dual-plate DMF system. If the c.a. hysteresis at the front and the rear contact line is asymmetrical, when compressing the droplet, the contact line on the more wettable side will advance earlier. When relaxing the droplet, the contact line on the less wettable side will recede earlier (Buguin et al., 2002; Daniel & Chaudhury, 2002; Daniel et al., 2004; Daniel et

al., 2001; Noblin et al., 2009). A digital microfluidic chip with discrete electrodes is used to verify this hypothesis.
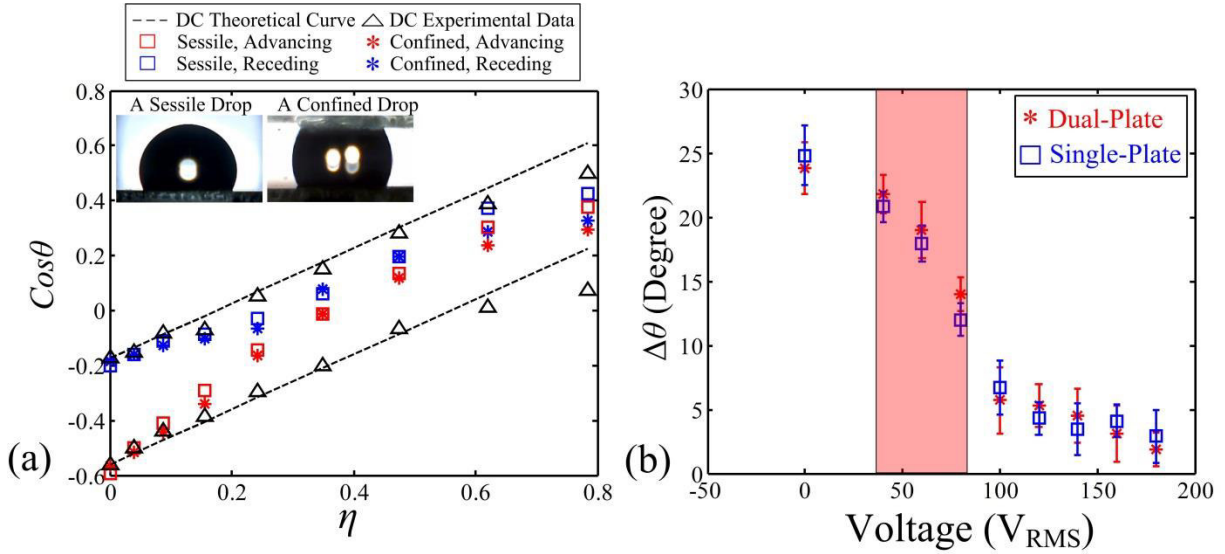
Fig. 4.8 (a) The c.a. of a sessile droplet and a confined droplet applied with various electrowetting numbers. Red square marker: advancing c.a. of a sessile drop; red asterisk: advancing c.a. of a confined drop; blue square marker: receding c.a. of a sessile drop in an open environment; blue asterisk: receding c.a. of a confined drop; dashed lines: dc theoretical advancing (bottom) and receding (top) curves of a sessile drop in an open environment; black triangle: dc experimental advancing and receding c.a. data of a sessile drop in an open environment. (b) Contact angle hysteresis as a function of applied voltages in both the single-plate and dual-plate systems.

The droplet is initially pipetted onto the chip surface to bridge the rear electrode and the front electrode (Fig. 4.9). A typical droplet actuation can be completed by applying a sufficient voltage ($V > V_{TH}$) to the front electrode, and at the same time, turning off the rear electrode. The minimum voltage to trigger the droplet movement is the threshold voltage (V_{TH}). The droplet cannot be actuated by sub-threshold voltages without external perturbations. Here, top plate

vibrations are used to trigger droplet movements under subthreshold voltages. A sub-threshold voltage V_{sub} is applied to the front electrode. A subtle c.a. change can be observed at the contact line of the front side (Fig. 4.9). θ_{aL}, θ_{rL}, θ_{aR}, and θ_{rR} are the left (rear) advancing angle, the left receding angle, the right (front) advancing angle, and the right receding angle. In Fig. 4.9 (a), $\theta_{aL} > \theta_{aR}$, when squeeze the droplet, the right c.a. reaches θ_{aR} earlier and advances to the right before the left contact angle reaches θ_{aL}; when stretching the droplet ($\theta_{rL} > \theta_{rR}$), the left c.a. reaches θ_{rL} earlier and recedes to the right before the right contact line can have a chance to recede. The asynchronous movement of the left and the right contact lines of the droplet forge a ratchet-like motion.
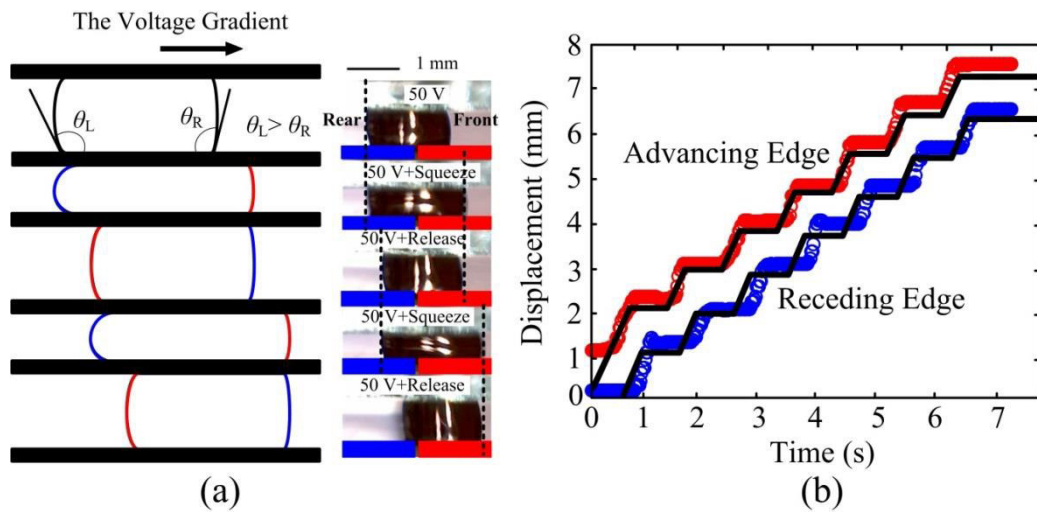
Fig. 4.9 The cross-sectional view of a droplet ratchet-like motion under AC voltages. (a) Droplet ratchet-like motion in an EWOD digital microfluidic chip. (b) Trajectory of the ratchet-like motion of the advancing (red) and receding (blue) edges. The black solid lines are the theoretical trajectories derived from the model. The driving voltage is 50 V_{RMS}, 1 kHz pulses.

The droplet profile shown in Fig. 4.9 (a) indicates the asynchronous ratchet-like motion. The blue arc in this figure indicates that the contact line is pinning in place during the top plate movement; the red arc indicates a moving contact line.

When the front contact line starts to advance, the time-variant gap height dominates the advancing step size (assume there is no front contact line recede). To model the droplet movement under top plate vibrations, we assume the arc of each side (left and right) of the droplet can fit into a radius-varying circle (Fig. 4.10).
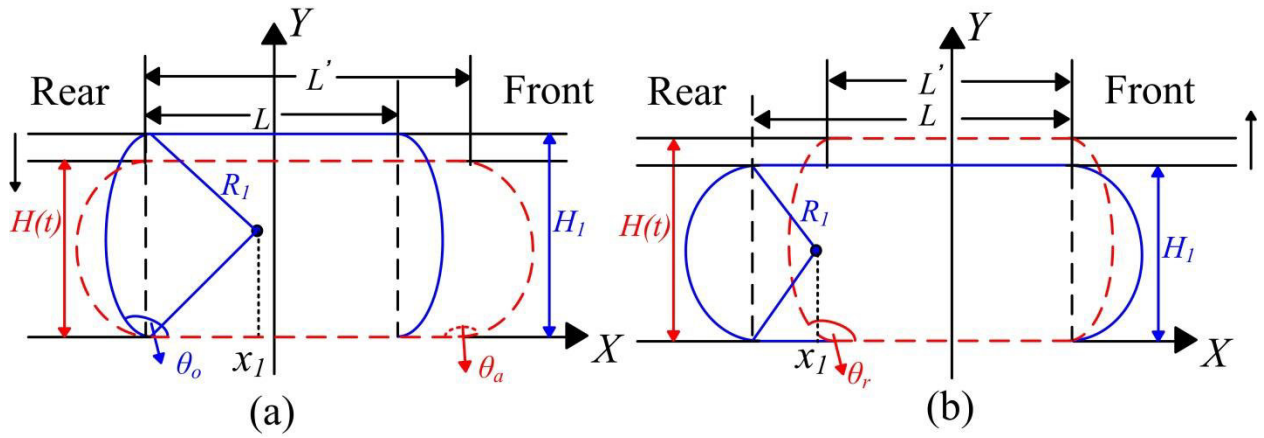
Fig. 4.10 (a) The geometrical model of a droplet with an advancing front contact line during the compressing regime. (b) The geometric model of a droplet with a receding rear contact line during the stretching regime. The blue solid outline is the initial droplet profile; the red dashed outline is the moving droplet profile.

The time variant gap height can be described as:

$$H(t) = H_1 - 2D_{PZT}ft \tag{4.15}$$

in which H_1 is the initial gap height, D_{PZT} is the PZT vibration magnitude, f is the PZT vibration frequency, t is the time variable. Therefore, the front contact line displacement is:

125

$$D_{front} = L' - L \tag{4.16}$$

in which D_{front} is the droplet front contact line displacement, H_2 is the gap height that the droplet contact line starts to advance, L' is the new droplet pitch, L is the original droplet pitch (Fig. 4.10 (a)). Based on the geometrical model in Fig. 4.10 (a), we can get:

$$R(t) = (H(t)/2)/\cos(180° - \theta) \tag{4.17}$$

$$x_1 = R_1 \times \sin\theta_o - \frac{L}{2} \tag{4.18}$$

$$(x - x_1)^2 + (y - \frac{H_1}{2})^2 = R_1^2 \tag{4.19}$$

$$\tilde{R}_1 = x = \sqrt{R_1^2 - \left(y - \frac{H_1}{2}\right)^2} - (R_1 \times \sin\theta_o - \frac{L}{2}) \tag{4.20}$$

$$\check{R}(t) = \sqrt{R^2(t) - \left(y - \frac{H(t)}{2}\right)^2} - (R(t) \times \sin\theta_a - \frac{L'}{2}) \tag{4.21}$$

in which the circle center: $R(t)$ is the time variant radius, $H(t)$ is the time variant gap height, the initial fitting circle center O (x_1, $H_1/2$), θ_o is the equilibrium c.a., θ_a is the advancing c.a., $\tilde{R}_1$ is the circle radius used in the method of revolution to calculate the volume. Similarly, in the receding regime, use $H(t) = H_1 + 2D_{PZT}ft$ in Eq. 4.15, θ_r in Eq. 4.21.

Use the method of revolution to calculate the volume:

$$V_I = \int_0^{H1} \pi \tilde{R}_1^2 dy = \int_0^{H(t)} \pi \check{R}^2(t)\, dy = V(t) \tag{4.22}$$

The time variant droplet pitch L' can be calculated from Eq. 4.21, and then use Eq. 4.16 to obtain the droplet advancing distance. The trajectory of a 3 µL droplet under 200 µm 1 Hz top plate vibrations travels through 3 electrodes as shown in Fig. 4.9 (b). Both the advancing and the

receding contact lines are moving in a ratchet manner by using a proper voltage magnitude indicated in Fig. 4.8 (b). The experimental trajectory agrees well with the model (Fig. 4.9 (b)).

For a EWOD DMF confined drop, the equilibrium contact angle (c.a.) has an average of 114.8° (Fig. 4.11 (a1)). In the compression regime (Fig. 4. 12 (a1-a3)), the c.a. increases to the advancing c.a. until the contact line starts advancing. After that, the c.a. keeps an almost constant c.a. while the contact line is advancing (Fig. 4. 12 (a2-a3)).
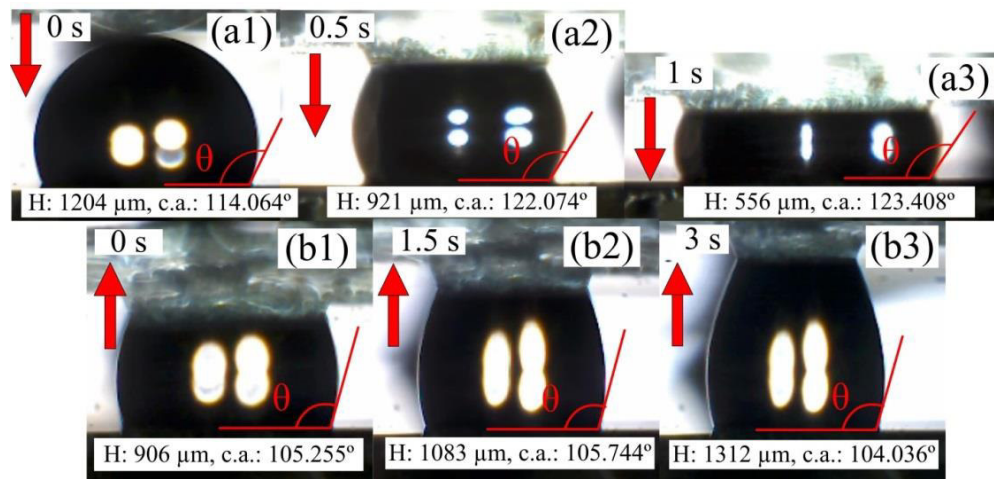
Fig. 4.11 A 3 µL water droplet under continuously compressing (a1-a3) and relaxing (b1-b3) operations from the top plate.

During the stretching regime (Fig. 4. 12 (b1-b3)), the c.a. decreases to the receding c.a. until the contact line starts receding. After that, the c.a. keeps a constant value during the receding movement until the left and right profile of the droplet is no longer fitting with an arc (Fig. 4. 12 (b3)). The theoretical fitting radius is calculated using a linear space of H ranges from 100 µm to 1.1 mm and an experimental average advancing c.a. of $\theta_a = 123.02°$. The experimental radius is measured using ImageJ by adjusting the gap height from 200 µm to 1 mm. The Teflon coated hydrophobic surface has an advancing contact angle around 120°, which means the gap height will be very close to the radius of the fitting circle as shown in Fig. 4.12, and the triangle ΔOAB

shown in Fig. 4.12 (a) should be close to an equilateral triangle when the c.a. equals to $120°$.

Similarly, the receding c.a. is analyzed using the average of $\theta_r = 103.12°$ in Eq. 4.23.

$$R = (H/2)/\cos(180° - \theta) \qquad (4.23)$$

The c.a. changes with the gap height in a highly nonlinear manner due to the pinning condition, the top plate moving direction, and its velocity. When continuously compressing the droplet in a low frequency (200 µm / s), once the top plate touches the droplet, the droplet will be forced to spread on the top surface very quickly due to the surface tension. Then start compressing the droplet to advance the contact line. The contact angle increases from $114.8° \pm 2.18°$ (arbitrary condition) to the advancing angle $123.02° \pm 2.37°$ and keeps the advancing c.a. while the contact line is moving (Fig. 4.11 (a1-a3)); when relaxing the drop from a small gap height, the c.a. decreases to the receding c.a. ($103.12° \pm 2.12°$) and keeps this value while the contact line is receding.
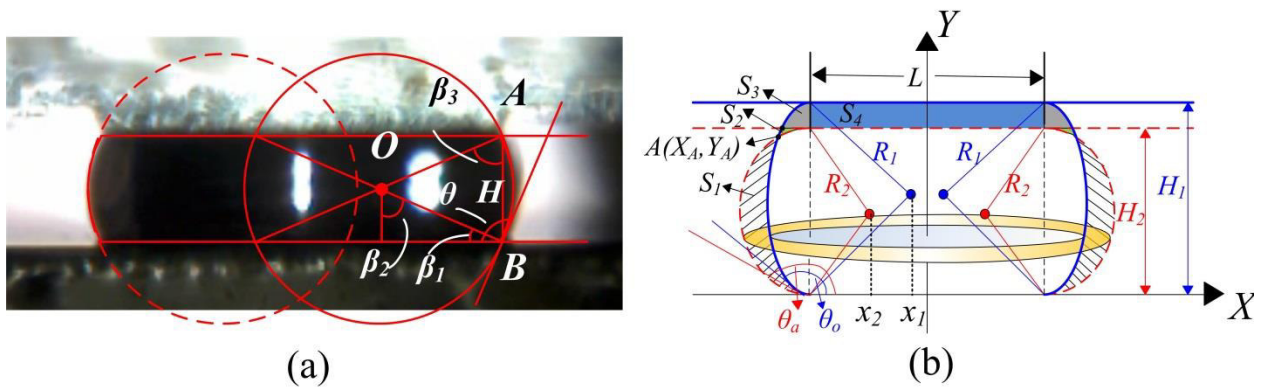
Fig. 4.12 (a) The fitting circular model. (b) The geometric model for calculating the droplet dynamic volume.

There are no significant c.a. variations when the droplet is being compressed or relaxed once the c.a. hysteresis has been overcome (Fig. 4.11). This is consistent with the time-domain c.a.

plot when measuring the c.a. hysteresis (F. Li & Mugele, 2008) and the sampled c.a. values when compressing the top plate (S. Hong et al., 2012). The abrupt c.a. changes only happen when the contact line starts depinning. It has been shown that the droplet shape in an equilibrium condition is spherical (Baratian et al., 2015). When experiencing unbalanced external pressures, the droplet cannot be treated as one single truncated sphere. The cross sectional view of a droplet confined between two substrates is shown in Fig. 4.12 (a). Two equivalent circular fits are applied to both sides of the droplet. Once the droplet cross-sectional profile is treated as these two circles, the radius of the fitting circle can be predicted by the gap height and the advancing/receding c.a. using: $\beta_1 = \theta - 90°, \beta_1 + \beta_2 = 90°, \beta_3 = \beta_2; R = (H/2)/\cos(\beta_3)$.

When starting to squeeze the droplet to the point that the contact line is about to advance, the curvature increases and there is no displacement along the X axis. Therefore, the geometrical model can be represented as seen in Fig. 4.12 (b). The initial droplet profile is marked in a blue outline; the squeezed droplet is marked by the red dashed outline. R_1 and R_2 are the fitted circle radius of the initial droplet and the squeezed droplet respectively. The method of rings and the typical revolution method are used to calculate the volume of the liquid. Given that the droplet volume is a constant during this slight compression, the extruded shaded part in Fig. 4.12 (b) marked by S_1 has the same volume as the summation of volumes marked by S_2, S_3, and S_4.

$$(x - x_1)^2 + (y - \frac{H_1}{2})^2 = R_1^2 \tag{4.24}$$

$$(x - x_2)^2 + (y - \frac{H_2}{2})^2 = R_2^2 \tag{4.25}$$

in which x_1 and x_2 are the x axis values of the centers of circle 1 and circle 2. Then we can get the coordinators of the centers of the two circles:

$$x_1 = -(\frac{L}{2} - R_1 \times \sin(180 - \theta_o)) \tag{4.26}$$

129

$$x_2 = -(\tfrac{L}{2} - R_2 \times \sin(180 - \theta_a)) \tag{4.27}$$

therefore, the ring's external radius can be represented by a function of the 'y.' The 'x' boundaries in circle 1 and circle 2 are:

For circle 1:

$$x = x_1 - \sqrt{R_1^2 - \left(y - \tfrac{H_1}{2}\right)^2} = \tilde{R}_1(y) \tag{4.28}$$

For circle 2:

$$x = x_2 - \sqrt{R_2^2 - \left(y - \tfrac{H_2}{2}\right)^2} = \tilde{R}_2(y) \tag{4.39}$$

using $A_1(y)$ and $A_2(y)$ to represent the area of the external circle and the internal circle of the ring:

$$A_1(y) = \pi \times (\tilde{R}_1(y))^2 \tag{4.30}$$

$$A_2(y) = \pi \times (\tilde{R}_2(y))^2 \tag{4.31}$$

using the volume of revolution method, the volume of droplet 1 (the original droplet) is:

$$V_I = \int_0^{H_1} A_1(y)dy \tag{4.32}$$

the volume of droplet 2 (the squeezed droplet) is:

$$V_{II} = \int_0^{H_2} A_2(y)dy \tag{4.33}$$

given that the volume of the droplet is a constant,

$$V_I = V_{II} \tag{4.34}$$

$$V_I = \pi \int_0^{H_1} [x_1 - \sqrt{R_1^2 - \left(y - \tfrac{H_1}{2}\right)^2}]^2 dy \tag{4.35}$$

$$x_1 = -\left(\frac{L}{2} - R_1 \times \sin(180 - \theta_o)\right) = R_1 \times \sin(\theta_o) - \frac{L}{2} \qquad (4.36)$$

$$R_1 = \frac{-H_1}{2\cos\theta_o}, H_1 = 2R_1\cos\theta_o \qquad (4.37)$$

Similarly, for circle 2:

$$V_{II} = \pi \int_0^{H_2} [x_2 - \sqrt{R_2^2 - \left(y - \frac{H_2}{2}\right)^2}]^2 dy \qquad (4.38)$$

$$x_2 = -\left(\frac{L}{2} - R_2 \times \sin(180 - \theta_o)\right) = R_2 \times \sin(\theta_o) - \frac{L}{2} \qquad (4.39)$$

$$R_2 = \frac{-H_2}{2\cos\theta_a}, H_2 = 2R_2\cos\theta_o \qquad (4.40)$$

To verify the theoretical model, we started from pipetting a droplet on the surface. We then pushed down the top plate using the PZT chips. Once the top plate touches the droplet and forms a vertically symmetrical system we measure the gap height as H_1 and find out the fitting circle's contact angle and radius. The theoretical value of H_2 can be used as a reference for the top plate displacement control in order to create an efficient ratchet-like motion under sub-threshold voltages. Given the initial gap height H_1, the equilibrium c.a. θ_0 is the average value from the empirical data. Typical values of θ_0 and θ_a are the averages of 6 tests on the Teflon coated surface. The fitted circle radius can be calculated from Eq. 4.23. Therefore, Eq. 4.40 can be used to predict H_2 (Fig. 4.13), which is the smallest gap height needed to depin the droplet.

When H_1 is large, the experimental H_2 is larger than expected Fig. 4.13 (a)). This is because the droplet profile cannot be fitted into the circular model for large H_1, and the radius of the fitting circle is not increasing with the gap height any further.
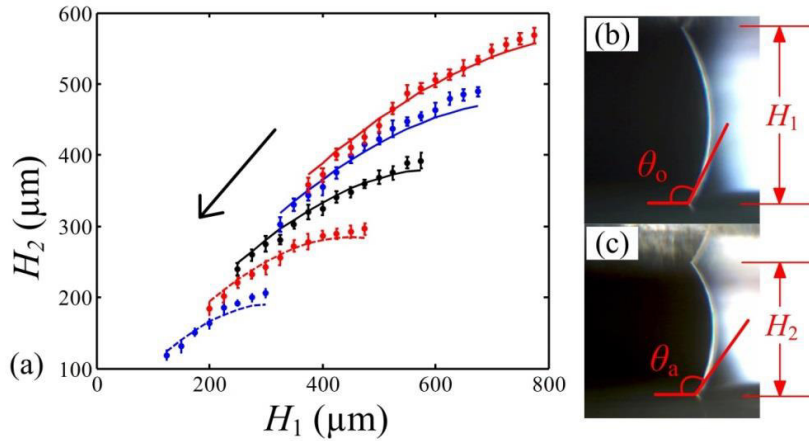
Fig. 4.13 (a) Droplet height required for advancing the contact line. H_1: the initial gap height; H_2: the gap height when the contact line starts advancing. The arrow shows the decreasing droplet volumes: 3 µL, 2.5 µL, 2 µL, 1.5 µL, and 1 µL. (b and c) A droplet edge profile changes during a compression regime. The gap height is decreased from H_1 to H_2, and the c.a. increases from θ_o to θ_a and the contact line is still pinning in place.

In Fig. 4.14, however, both the front and the rear contact lines are moving at the same time (marked by asterisks). This indicates that the 100 V AC eliminates too much c.a. hysteresis. The front contact line is very easily depinned during the top plate movement (as indicated in Fig. 4.9 (b)). The undesired contact line recede slows down the droplet ratchet displacement. We call this behavior 'semi-ratchet-like motion.' Apparently, the droplet under semi-ratchet-like motion needs more top plate vibration cycles to reach the target electrode. Interestingly, the undesired recede only happens during the stretching regime. When compressing the droplet, the rear contact line is always anchored in place (blue profile, Fig. 4.14 (a)). This is because the front contact line is experiencing a much smaller c.a. hysteresis and resistive force than the rear contact line.

The step size for each ratchet movement is limited by the hysteresis 'level' at the front contact line in addition to the vibration magnitude. If AC subthreshold voltage is being used, compressing the droplet hard will push the front contact line further during the compressing regime, but the front contact line will recede back with the rear contact line during the relaxing regime (Fig. 4.14). Under AC subthreshold voltages, the hysteresis at the front contact line is not large enough to tolerate the contact angle variations during the stretching regime. We can imagine that if the front contact line has a very small receding c.a. and the rear contact line has a very large advancing c.a., then the ratchet step size will only depend on the magnitude of the top plate vibration, and the undesired front contact line recede will not happen. The 3 µL water droplet in Fig. 4.9 (a) under 50 V_{RMS} driving voltage needs at least two top plate vibration cycles (1 Hz) to reach the target electrode. However, the 'semi-ratchet-like motion' needs more cycles to create the same horizontal displacement due to the undesired recedes during the stretching regime.
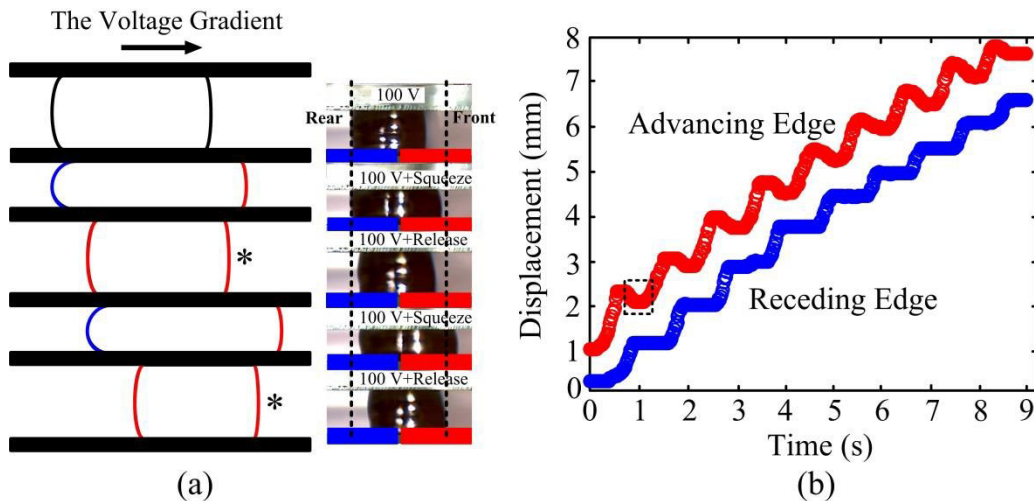
Fig. 4.14 (a) The cross-sectional view of the semi-ratchet-like motion of the advancing and the receding edge of a water droplet. The driving voltage is 100 V_{RMS}, 1 kHz. The blue and the red boxes are used to mark the positions of the rear electrode and the front electrode respectively.

(b) Trajectory of the semi-ratchet-like motion of the advancing and receding edges. The dashed square in (b) marks the first undesired recede.

While increase the voltage magnitude to 100 V_{RMS}, as indicated by Fig. 4.8, the c.a. hysteresis will decrease to less than 7˚. The experimental contact line trajectory won't follow the geometrical model developed in this study. The front contact line recedes back a little when relaxing the top plate (Fig. 4.14, red trajectory; the first undesired recede is marked with a dashed square). This indicates that the advancing c.a. at the rear edge is much larger than the advancing c.a. at the front edge. Apparently, additional top plate vibration cycles are needed for the semi-ratchet-like moving of the droplet to travel across 3 electrodes (Fig. 4.14).

Both AC and DC voltages can change the surface wettability, but AC can eliminate the c.a. hysteresis as well (F. Li & Mugele, 2008). Using sub-threshold AC voltages and a top plate vibration to create droplet movements must have a well-tuned voltage amplitude to maintain a moderate c.a. hysteresis at the front contact line. Given that an applied DC voltage can decrease the advancing angle and the receding angle at the same time while not changing the hysteresis significantly, it is very likely that the droplet under subthreshold DC can have a larger step size. The top plate is decreased to 515 µm to advance the front contact line over the target electrode (Fig. 4.15 (a)). As a result, only one top plate vibration cycle is required to actuate the drop to the target electrode. A continuous ratchet-like movement in time domain is plotted in Fig. 4.15 (b). Only a subtle undesired recede (Fig. 4.15 (b)) is observed at the front contact line during the relaxing regime. The rear edge still has a clean ratchet-like motion as expected.
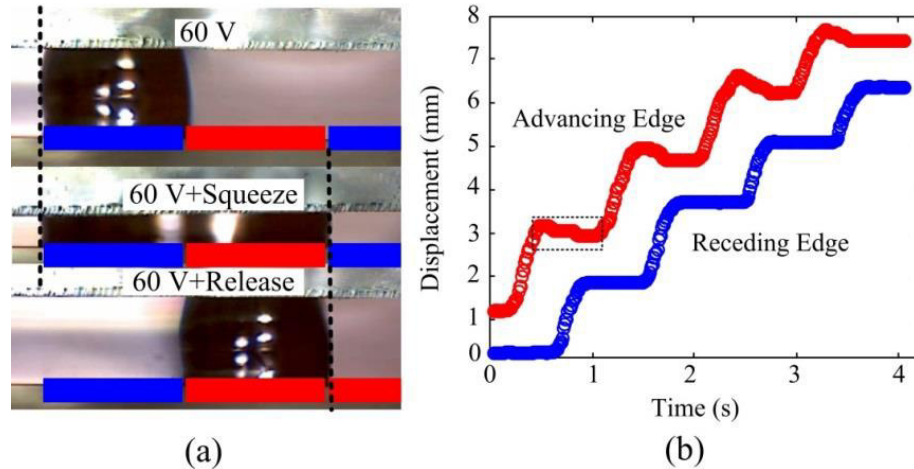
Fig. 4.15 Driving a 3 µL water droplet under 60 V_{RMS} DC sub-threshold voltages. (a) Using 60 V_{RMS} (sub-threshold) DC to drive a droplet under 1 Hz top plate vibration. The red box indicates the positions of activated electrodes; the blue box shows the positions of the inactivated electrodes. (b) Trajectory of the semi-ratchet-like motion of the advancing and the receding edge of this water droplet.

It has been reported that the density matching of aqueous droplets with bromohexadecane (Baratian et al., 2015) and with silicone oil (T. Chen et al., 2014) ambient results in a very small bond number, which makes the c.a. hysteresis negligible. In the liquid filler environment, both DC and AC have efficient actuating capabilities (T. Chen et al., 2014). However, the oil environment is undesired for practical applications. The c.a. hysteresis in an air ambient is significant even on a Teflon coated hydrophobic surface (Mugele, 2009). When the voltage is not strong enough to overcome the c.a. hysteresis, the top plate vibration introduced in this study can trigger the 'stuck in place' droplet for a ratchet-like movement, which is called 'sub-threshold actuation' in this study. The AC voltage increases the wettability of the target electrode, and at the same time, eliminates the c.a. hysteresis. A proper c.a. hysteresis is required to anchor the front and rear contact lines asynchronously for a ratchet-like motion. Applying DC voltages can

modify the surface wettability and maintain a proper c.a. hysteresis at the activated electrode surface. Therefore, for sub-threshold droplet actuation, DC is preferred.

Because the droplet front contact line advances only when the top plate is compressing, droplet transportation velocity under subthreshold voltages depends on the frequency of the top plate vibration (at low frequency, for example 1 Hz in this study). The step size during each vibration cycle is dominated by the asymmetrical c.a. hysteresis of the front and the rear electrodes. Both the advancing and the receding contact c.a. at the front contact line should be smaller than their counterparts at the rear contact line, and at the same time, a proper c.a. hysteresis at the front contact line is desired to tolerate the c.a. changes during the top plate stretching operation. This is a special requirement for subthreshold voltage actuation, because any c.a. hysteresis in the traditional EWOD droplet actuation ($V > V_{\text{TH}}$) is treated as a resistive force that should be minimized.

The droplet ratchet-like motion under subthreshold voltages only happens at low frequency top plate vibrations. Under subthreshold voltages, the droplet ratcheting motion slows down when the frequency is larger than 10 Hz with both AC and DC driving voltages. But differently, using regular EWOD driving voltages at $V > V_{\text{TH}}$, the actuation velocity increases with the top plate vibration frequency, and this improvement saturates at about 50 Hz. Relatively high frequency (> 100 Hz) vibration creates fast droplet body fluctuations and even resonance which leads to a faster movement on a chemical gradient surface (Daniel et al., 2004). However, high frequency and large magnitude vibration is not applicable to the passively vibrated top plate, and the mechanisms for high frequency vibration induced droplet fluctuations are beyond the scope of this study.

4.2.4 Conclusion

This gently external perturbation extends the conventional dimension of optimizing the EWOD chip with surface treatment, and breaks the bottleneck due to c.a. saturation and dielectric breakdown under high voltages. This method allows the droplet movement being controlled without adding any post-fabrication to the EWOD chip. The pinned contact line is released by continuously compressing and stretching the droplet, which allows the droplet to move to the direction with minimum interfacial energy. The subthreshold actuation also means a lower actuation voltage is applicable to the EWOD DMF device, which indicates a new method for low voltage design in EWOD. Furthermore, the dynamic top plate positioning system provides a potential solution for the critical problems of EWOD DMF devices such as contact line pinning and poor volume control.

Chapter 5 On-chip cell cultures for anti-biotic resistant bacteria detection

5.1 Introduction

EWOD digital microfluidics is a promising technology in immunoassay reactions (Ng et al., 2015), electrochemistry measurement (Rackus, Shamsi, & Wheeler, 2015), and on-chip PCR (T. Chen et al., 2016). These reported developments are contributing significantly to the state-of-the-art of using EWOD DMF to solve practical problems. For clinical diagnostics, the patients' blood sample is usually in several milliliters, but the concentration of the pathogen sometimes is really low. It has been very challenging to capture the low concentrated pathogens with biosensors in the blood samples. Therefore, 24-72 hours culturing to let the pathogen or bacteria to grow to the detectable level is required. Bio-affinitive filters and membranes (Orlandi & Lampel, 2000; Wigginton & Vikesland, 2010) have been used to isolate the targeted pathogen and shorten the pre-culturing period. An alternative way to isolate the pathogen is using magnetic beads. Integrating magnetic beads for isolating targeted pathogens in the mixture makes the EWOD system more versatile being used for the filtering purpose. From the clinical point of view, if the mixture is a blood sample from a patient, the micro magnetic beads can be automatically mixed with the sample. The interested pathogen, if any, will be bonded to the micro beads after several mixing operations (Ng et al., 2010). Then use a magnet below the bottom substrate to fix the beads while the waste solution is being removed. The pathogens are captured by the beads and will be released from the beads by a following chemical reaction. The magnetic beads sorting technique has been very popular. However, using big tubes and beakers to conduct this experiment requires large amount of blood samples which introduces significant ambient noise.

Our approach will use digital microfluidics (DMF) electrowetting on dielectric (EWOD) chips to carry out on-chip electrochemistry measurements instead of using magnetic beads and PCR. We passively dispense a micro-liter droplet into the "virtual microwell" (Fig. 5.1) to a hydrophilic area on a DMF chip (Eydelnant, Uddayasankar, Liao, & Wheeler, 2012; Ng et al., 2015). The microwell environment can provide an ultra-low noise isolated culture ambient and enables cyclic voltammetry measurements. DMF EWOD chips have discrete actuation electrodes which are a friendly interface with external digital integrated circuits and are capable of manipulating liquid droplets (Y. Li et al., 2016; Y. Li et al., 2015) in a gentle manner for one-step media exchange.
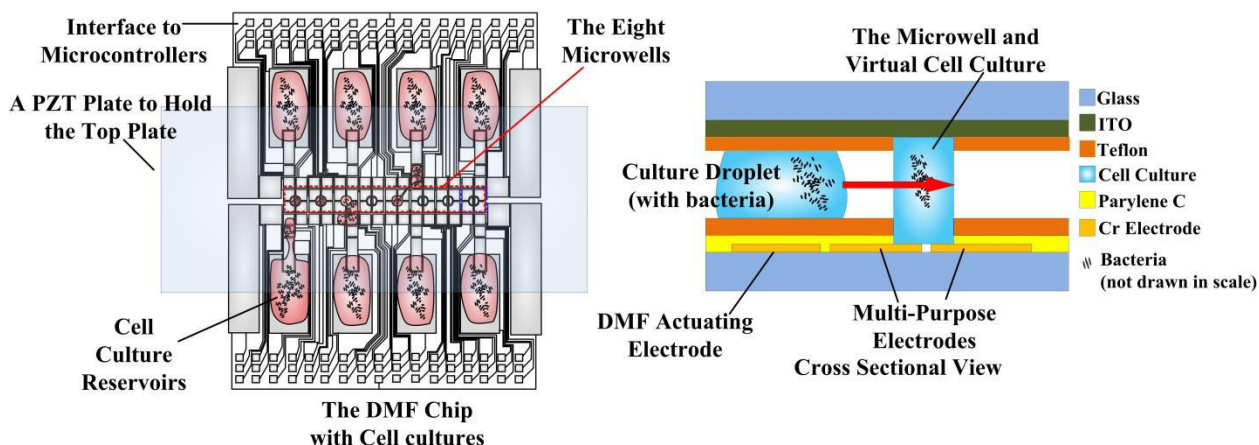
Fig. 5.1. The proposed topology of the DMF chip. The top plate is an ITO coated transparent glass, held by a PZT plate. The microwell area is hydrophilic, when a droplet is actuated through this area, a part of the droplet will be passively dispensed at the microwell. The working electrode (4 µm × 100 µm), reference electrode, and the counter electrode are patterned at the microwell. The volume of the cell culture in the microwell can be 0.1 µL to 5 µL.

The electrode array topology of the DMF devices can be easily customized by CAD tools and fabricated by photolithography available at UNLV. Nanoelectrodes for fundamental

electrochemical measurements such as cyclic voltammetry have been realized on the DMF chip recently (Dryden, Rackus, Shamsi, & Wheeler, 2013), making it possible to use DMFs for bacteria metabolic analysis. In this chapter, the anti-biotic resistant *E. coli* is prepared; ampicillin is used to sort the bacteria community which has the implanted anti-biotic gene. The viability of the bacteria is tested with electrochemistry measurement using resazurin as the redox marker.

5.2 Anti-biotic resistant *Escherichia coli* (*E. coli K-12* Strain) preparation

In molecular biology, transformation means a certain genetic change that the genes inside individual cells are alternated by external mutant DNA sources. Genetic transformation has been used for creating good bacterial mutant and makes them to be 'biological factory'. For example, the cost of insulin has been reduced significantly because of the mutant bacteria can produce enough insulin for human beings. The genotype of *E. coli* is relatively simple and well understood. The GFP gene to be transferred to the cells is from bioluminescent jellyfish *Aequorea victoria*. GFP allows jellyfish to glow in the dark. If this gene is transferred in the *E. coli*'s cells, the same fluorescent gene will be produced too.

The regular *E. coli K-12* strain (Carolina Biological Supply Company, Burlington, NC) doesn't have anti-biotic resistant genes, for example, anti-ampicillin genes. The purpose of this experiment described in this section is to transfer anti-biotic resistant genes to the regular *E. coli K-12* strain. Therefore, the anti-biotic drugs (ampicillin used here) won't be able to kill the bacteria. Green fluorescent protein gene will be transferred together with the antibiotic genes to make the mutant distinguishable from the regular types (Fig. 5.2a). The pGREEN transformation kit purchased from Carolina Biology Supply is shown in Fig. 5.2b.
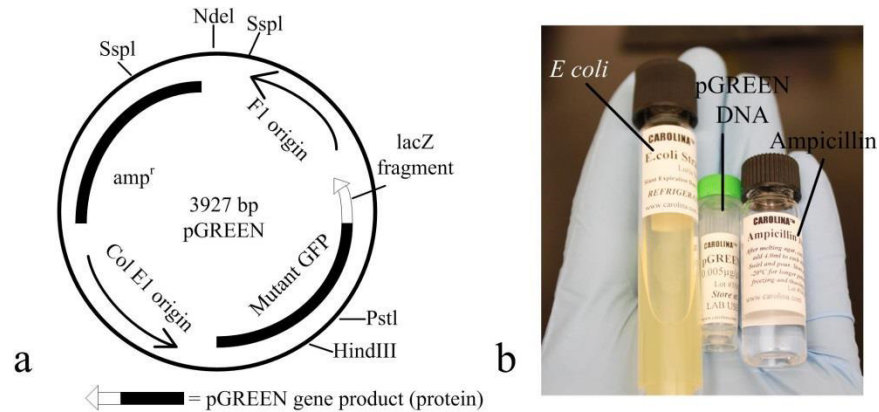
Fig. 5.2 The pGREEN plasmid gene.

The pGREEN plasmid contains GFP linked to beta-galactosidase. This combination of genes was selected for this study because the protein product from this combination makes the bacteria in a green color in the natural light ambient. When exposed to UV light, fluoresce is visible.

There are two types of agar plates used in this experiment, one has ampicillin (Amp+, 2 µL in 250 µL melted agar); the other one is pure agar culture. The ampicillin agar plate only allows the transformed *E. coli* to grow. Other bacteria will be killed.

First, put 4 a loop-full (about 10 µL) of bacteria to a 250 µL LB broth for 7 hours to make more competent bacteria, which are able to take the external gene inside the bacteria more efficiently. Centrifuge the tube and remove the top suspension. Inject 250 µL $CaCl_2$ into the bacteria mixture and vertex them. Then Centrifuge the tube again, and remove the surface suspension. The bacteria is washed by ice cold $CaCl_2$ for 4 times, 30 seconds for each. 10 µL pGREEN plasmid DNA is added to the tube and recover for 5 minutes in ice cold environment. Then give the cell suspension a 42 ˚C heat shock for 90 seconds. Heat shock transformation is conducted in a calcium rich environment (calcium chloride) to reverse the electrostatic repulsion between the DNA molecules and the bacteria. The heat shock creates more pores in the plasma membrane of the bacteria and makes the cells accessible to the external DNAs.

141

The cell suspension is put in room temperature and culturing for 30 minutes. Evenly divide the suspension into four tubes, and centrifuge them separately. Streak the cells in the four tubes to four agar plates respectively: Amp-, GFP-; Amp-, GFP+; and two Amp+, GFP+ plates. Culture the four plates at 37 ˚C for 24 hours (Fig. 5.3).
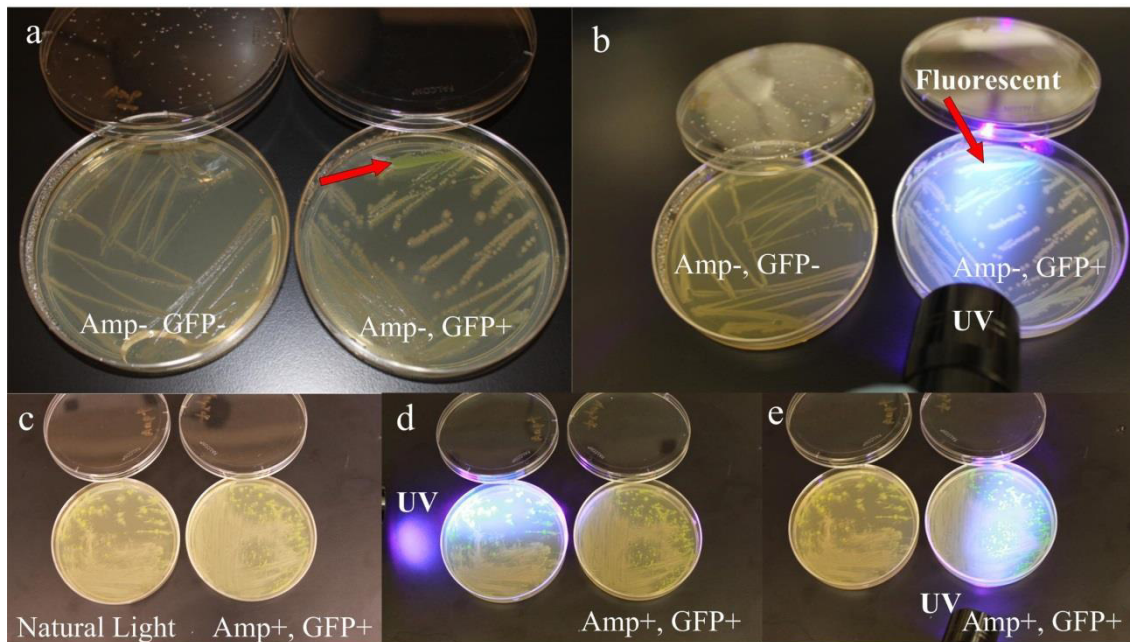
Fig. 5.3 Results of the pGREEN gene transformation. (a) The Amp-, GFP- petri dish does not have GFP gene, so only regular *E. coli* strain grows; the Amp-, GFP+ petri dish has GFP gene but does not have antibiotics (Ampicillin), so the regular and the transformed *E. coli* grow together and compete against each other. Only few GFP transformed *E. coli* mutant are observed (red arrow). (b) Using a UV light source to observe the fluorescent glow of the transformed *E. coli*. (c-e) Petri dishes based cultures with antibiotics (ampicillin) added to the culture.

Ampicillin is needed to sort the GFP gene transformed *E. coli* (Fig. 5.3). In Fig 5.3a and Fig. 5.3b, very few GFP transformed *E. coli* are observed (marked by the red arrow); however, in Fig. 5.3c-e, the GFP transformed *E. coli* will survive under ampicillin, but the regular *E. coli* will be killed. Therefore, more GFP transformed colonies are observed (the green spots in natural light

and the glowing spots under UV). The amount of GFP transformed colonies in the four plates are shown in Fig. 5.4. Adding ampicillin can efficiently sort the GFP *E. coli* and suppress the growth of regular *E. coli*.
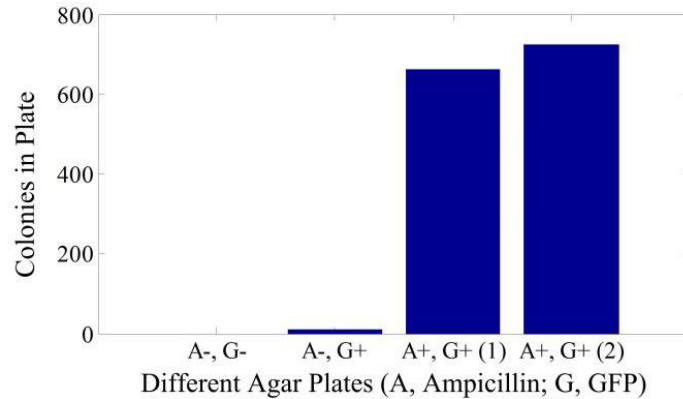
Fig. 5.4 The amount of GFP transformed colonies in the four plates. A, Ampicillin; G, GFP.

The transformed *E. coli* are kept in the plates and stored at 4 ˚C for the following experiments.

5.3 Post-fabrication of the top and the bottom substrates of the DMF chip

The top plate of the EWOD system should be post-fabricated. The hydrophilic area is a non-Teflon area created by Teflon lift-off technique (Ng et al., 2015). The lithography process is shown in Fig. 5.5.
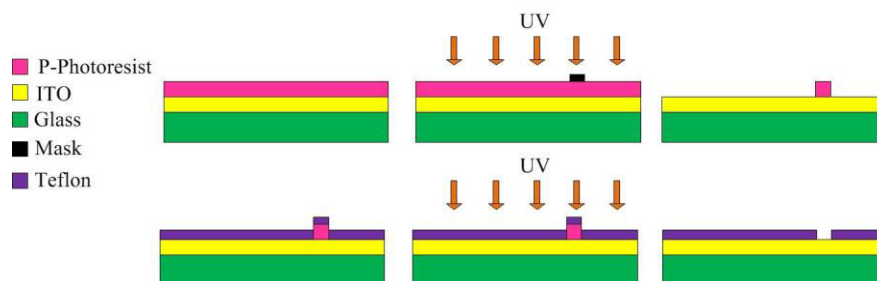
Fig. 5.5 Teflon lift-off technique to fabricate the on-chip microwell bacteria culture.

The ITO glasses are purchased from Adafruit. The ITO glasses are post-fabricated in the cleanroom facility at UNLV. First, spin coat the photoresist directly onto the ITO layer. Use the photomask to cover the microwell spot and expose the chip under UV for 40 seconds. Develop the chip for 30 seconds to remove the unwanted photoresist. Spin coat a 250 nm Teflon to the surface, then baked at 160 ˚C. Pour UV to the whole chip and use acetone to strip all the remaining photoresist. The Teflon above the microwell spot is on the remaining photoresist spot, which will be removed (lift-off) by acetone.

To post-fabricate the bottom plate, extra steps should be carried out. The differences between the bottom and the top plate is the extra insulating layer (Su-8 negative photoresist is used as the dielectric layer here). To keep the extra layer not being developed in the last lift-off process, negative photoresist is needed (Fig. 5.6).
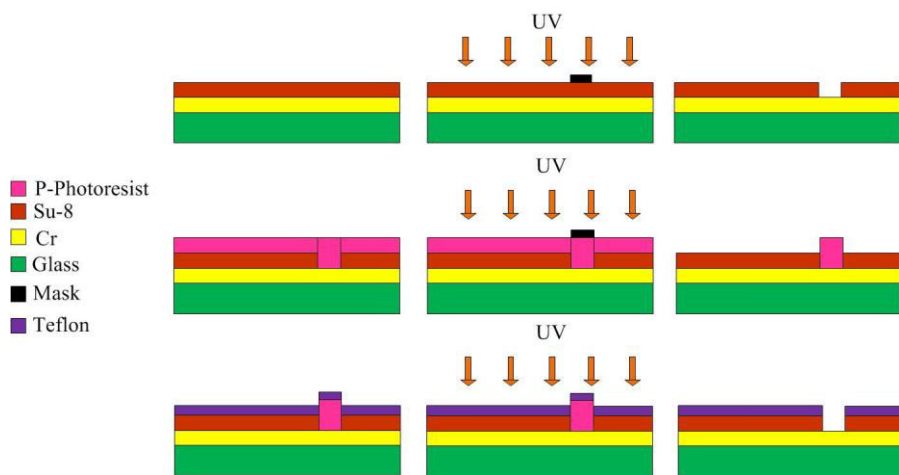
Fig. 5.6 Bottom plate post-fabrication.

The Chromium electrode on the bottom microwell serves as the working electrode for the electrochemistry electrodes. Bare metal electrodes are required for the desired sensing operations. The negative photoresist is coated on the bottom substrate surface. After the first round exposing and developing, the bare metal electrode opening is formed. The following steps are the same as

the Teflon lift-off process as we fabricated the top late (Dryden et al., 2013). The negative photoresist will be left on the surface as the dielectric layer because the exposure to UV induces the SU-8 molecule cross-linked and becomes resistive to the developer. Using this post fabrication method, we can keep using the same black-dot based photo mask to pattern the microwell.

5.4 On-chip cell cultures

The most significant advantages of using on-chip cell cultures and micro electrode on-chip electrochemistry measurements are shorter culturing duration and smaller sample volume. Shortening the culturing period can provide accurate diagnostic results at the earliest time for the most efficient treatment; the smaller sample volume can reduce the patients' stress and pain at the sampling phase. The formation of the on-chip micro cell cultures is demonstrated in Fig. 5.7.
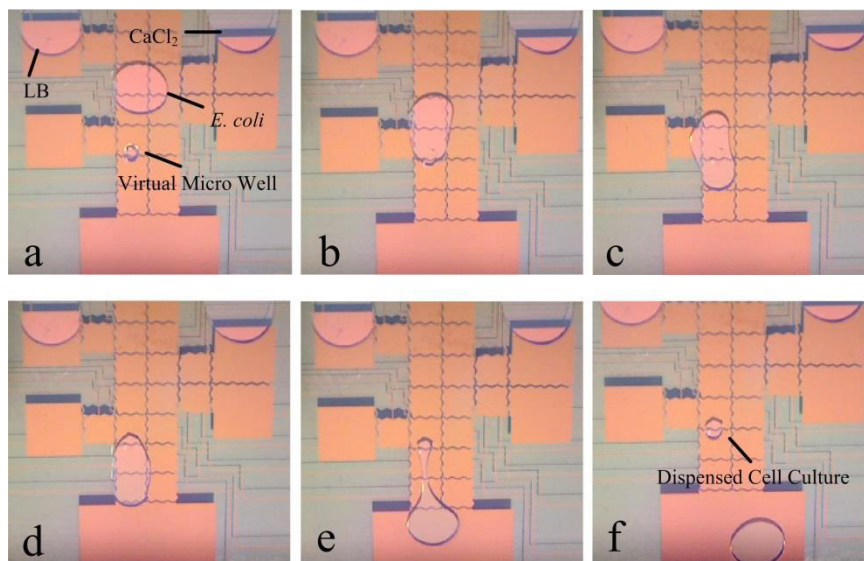
Fig. 5.7 Passively dispensing bacteria cultures.

First, bacteria suspensions are dispensed using passive dispensing. The passive dispensing is realized by actuating a suspended liquid through a hydrophilic 'virtual microwell' (Fig. 5.1 and

Fig. 5.7), the hydrophilic area will keep a cylindrical liquid drop locally. The remaining liquid will be actuated away from the microwell (Fig. 5.7). LB nutrient cultures are added to the microwell automatically to compensate the evaporated liquid in the cylindrical cell suspensions at the microwell.

The on-chip *E. coli* are observed under microscope (Fig. 5.8). The transformed E. coli colonies can be observed by naked eyes. In natural light ambient, the GFP looks in green color. Under UV light, the fluorescent glow can be observed. Without adding new LB cultures, the droplet-based cell culture will dry out in 15-20 minutes. The bacteria will stay at both the bottom and the top substrate. We remove the top plate and observe it under the microscope. In Fig. 5.8a, c, and e, the microwell is observed under natural light; In Fig. 5.8b, d, and f, the microwell is observed without the natural light. Results show the Amp+, GFP+ group has the most GFP transformed *E. coli*; *E. coli* colonies can be observed in natural light in Fig. 5.8c, but cannot be seen when the light is turned off, which means the colonies are mixed with regular E. coli, which doesn't expressing GFP, and most of them are not GPF transformed colonies.
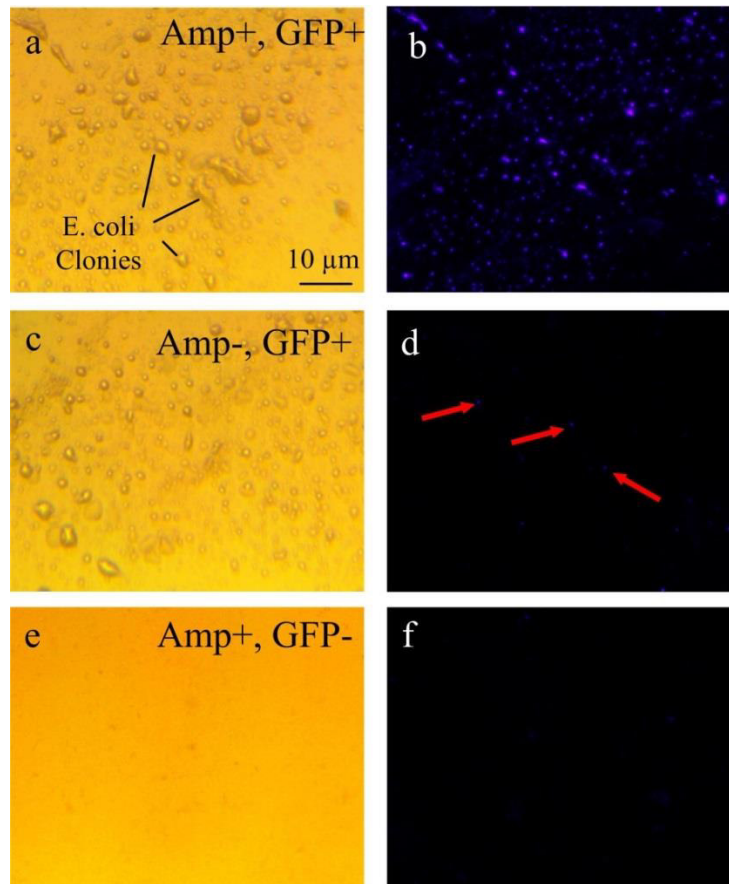
Fig. 5.8 (a-b) Add ampicillin to the microwell culture to inhibit the growth of regular *E. coli*, but the GFP mutant *E. Coli* can be seen under UV light. (c-d) Microwell bacteria culture without ampicillin added to sort the transformed bacteria mutant. The bacteria colonies are visible in natural light ambient in (c), but very few of the colonies are visible under UV (d), which means the regular *E. coli* strain occupies the resource and inhibit the growth of the transformed bacteria. (e-f) There is not GFP transformation conducted, but still has ampicillin in the culture. Regular bacteria do not have the anti-ampicillin gene.

5.5 Electrochemistry measurement

We disconnect the high driving voltage cable and interface the potentiometer with the bottom electrodes and the top ITO electrodes. The electrodes on the bottom substrate is connected to the

working electrode input, the ITO layer is connected to the reference electrode input. Resazurin is used as a bio-marker for the bacteria viability (Besant, Sargent, & Kelley, 2015; Khazalpour & Nematollahi, 2014). Different from the conventional way to detect redox fluorescent product of the resazurin by the metabolic process of the bacteria (O'Brien, Wilson, Orton, & Pognan, 2000), we use electrochemistry differential cyclic voltammetry to test the redox reaction of the resazurin. The mechanism is based on the following reduction:
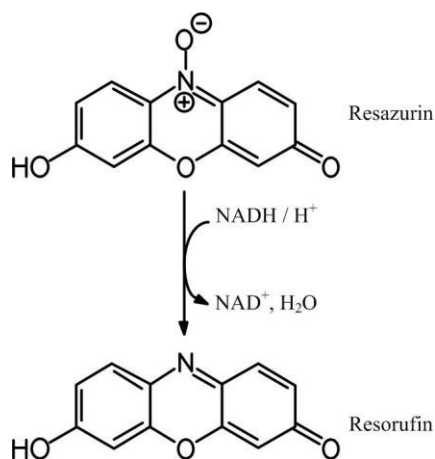
Fig. 5.9 Reduction of resazurin to resorufin in living bacteria.

Resazurin is a blue dye, when irreversibly reduced to pink colored and highly red fluorescent resorufin (Fig. 5.9). Adding antibiotic to the bacteria cultures, metabolically-active bacteria has a reducing environment to reduce the compound, and the viability of the cells can be read out as the changes in fluorescence. Resistant bacteria are still able to metabolize / reduce the compound, but the susceptible bacteria cannot. The fluorescence based optical detection requires the quantity of the bacteria and the glowing proteins to reach a detectable level, which usually requires an overnight culturing. However, in this study, we will use electrochemistry measurement technique to detect the bacteria viability in the microwell environment. The small volume bacteria culture allows the chemical concentration reaches the detectable level very

148

quickly. Less liquid sample is needed for this detection means less pain the patients will receive during the blood sampling.

Peak I in the blue curve (Fig. 5.10b) reveals an irreversible two electron process leading to resorufin; the second peak displays a reversible two electron process related to the formation of dihydroresorufin (Khazalpour & Nematollahi, 2014).

Using the isolated microwell environment for electrochemistry measurement is good for low quantity of bacteria in the culture. The passively dispensed droplet volume in the microwell can vary from 0.1 µL to more than 10 µL, which provides a relatively small liquid environment. The embedded on-chip micro electrodes can fit into this micro environment.
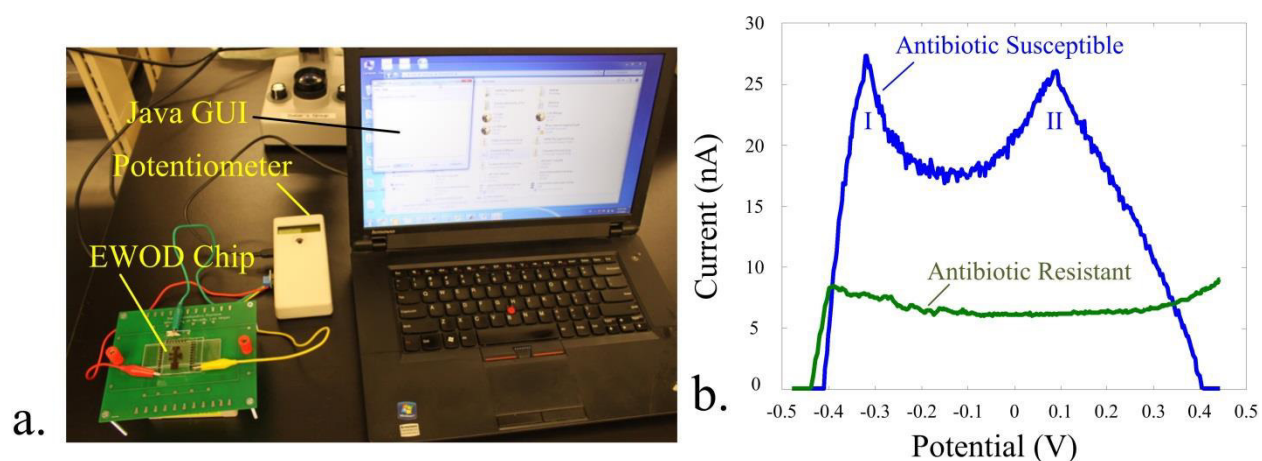
Fig. 5.10 a. The electrochemistry measurement (differential pulse voltammagrams) setup for resazurin redox detection. b. Cultured for 3 hours, the antibiotic susceptible bacteria dead, so the resazurin is still in the solution, and the curve is not changing and showing the two phases of the redox reaction.

The amount of colonies is calculated in the following way. A 50 µL bacteria suspension is diluted to 50 mL and cultured at room temperature for 48 hours. Take 0.1 mL of the suspension and pure it onto the agar plate. Cultured at 37 ˚C overnight. The colonies are counted under

149

natural light. One of the results is 33 colonies. The original CFU (colonies forming unit) is calculated by the following equation:

$$\frac{0.1\ mL}{50\ mL} = \frac{33}{x} \tag{5.1}$$

So the original suspension has x=16500 CFU/mL, which is 16.5 CFU/µL.

The sampled current points in Fig. 5.10b are normalized to compare to each other. Three samples are prepared from the same cell suspension. 200 µL, 100 µL suspensions are kept in tubes; 2 µL cell suspension is passively dispensed to the microwell on the DMF chip. The initial cell concentration is 16.5 CFU/µL. 1 mM resazurin is soluted into the suspension. 50 µL ampicillin solution from Carolina Biological Supply is added to the suspension. Electrochemical detection of the bacteria metabolism is conducted for every 5 hours. The on-chip microcultures are allowed to be dried out, and being refilled with LB culture when the measurement is conducted. The current signal decrease is measured.
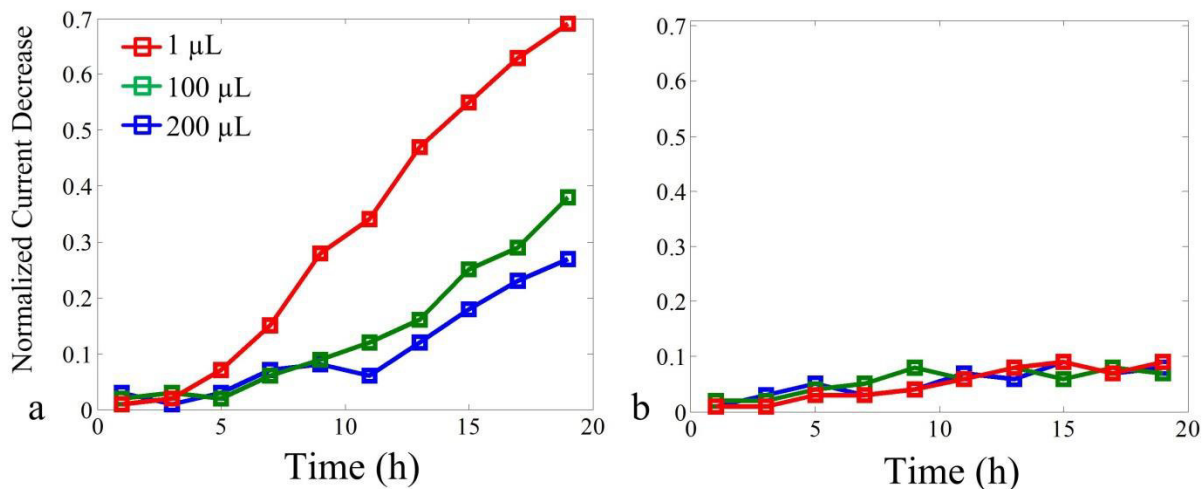
Fig. 5.11 a. Normalized current signal decrease of the 1 µL (red), 100 µL (green), and 200 µL (blue) cell cultures. The cell cultures have the same concentration of resazurin, ampicillin,

and GFP transformed bacteria (antibiotic resistant). b. The same measurement with Regular *E. coli* cultures.

The 1 µL mixed culture with antibiotic resistant *E. coli* has significant current decrease after 5 hours culturing. The 100 µL and the 200 µL cultures have slower response to the measurement. In Fig. 5.11b, the growth of the regular *E. coli* is inhibited by ampicillin, so there are no significant metabolic activities that can consume resazurin. However, we can still find a subtle current decrease for the three groups after 10 hours. The resazurin may be partially reduced by oxygen under natural light. This is why the ambient light source should be limited during the experiments. From Fig. 5.11a and b, the oxygen reduced resazurin is much less than the bacteria reduced resazurin. Therefore, this initial experiment design is valid.

On-chip microwell electrochemical measurements show the superior required detection time and the higher reduced current in Fig. 5.11a. Conducting electrochemical measurements in a micro environment using miniaturized electrodes is promising for shortening the diagnostic time and reducing the clinical sample.

5.4 Conclusion

In this chapter, we developed a DMF based on-chip culture environment. Post fabricated DMF top and bottom substrates have local hydrophilic areas to allow miniaturized microwell cell cultures passively dispensed at the microwell. pGREEN plasmid DNA is implanted into the regular *E. coli*. More successful transformation has to be assisted by the antibiotic sorting, which kills the competitors and saves the antibiotic resistant *E. coli*. On-chip cell cultures with electrochemical detection saves tremendous amount of time to achieve the same output current decrease. The micro environment measurement has many advantages to be investigated. The

DMF chip is a promising tool for detect the viability of the antibiotic resistant bacteria using electrochemical measurements.

Chapter 6 Summary, contributions, and future work

This dissertation covers both low-cost DMF chips on PCB and high performance glass DMF chips; their surfaces are characterized using contact angles (c.a.), c.a. hysteresis, threshold voltages, and actuation velocities. Significant improvements are observed by using the proposed dynamic top plate into the DMF system. A super portable control interface allows users to operate the droplets on any WiFi terminals, such as a smart phone or a laptop, which avoids massive wire connections. Using this developed DMF system for the on-chip bacteria cultures and electrochemistry measurement are promising for bacteria susceptibility detection and other microbiological experiments.

The purpose of my study is to develop a lab-on-chip micro droplet actuator, which can be controlled by a smartphone or a laptop wirelessly through the WiFi connection. The micro droplet actuator is built upon a Chromium coated electrode array on a glass substrate. Super-portable 3-D printing chip interfaces connect the chip pads to external control electronics. A highly efficient high-voltage module is developed to provide up to 200 V DC as the driving voltages. The on-chip oscillator provides 0-10 kHz, 5 V pulses as the MOSFET gate-toggling signal for the generation of the 200 V pulses at the 'drains' of the MOSFETS. The digital microfluidic chip developed upon the EWOD technology is called 'digital microfluidics (DMF)'. By using this technology, the micro-liter level droplets can be manipulated in a high throughput manner, which is promising for the next generation laboratory automation technology. Future applications, such as intelligent DMF with embedded systems, electrowetting optical lenses, adaptive droplet volume control, bio-inspired renewable energy optimization, bio-MEMS, on-chip cell cultures, and point-of-care diagnostics will be explored.

Appendix: The next generation portable EWOD DMF system controlled via Wi-Fi

A.1 Introduction

The modern EWOD DMF system has been studied for about 16 years since the first DMF development from Duke University (M. G. Pollack et al., 2000). The main composition of the system includes bench equipment such as power supply, signal generator, voltage amplifier, and bulky control systems. People have been trying to make the system portable via PCB substrates and on-board control systems (Gong, Fan, & Kim, 2004) or using a smart phone compatible 3-D printed cube to hold the EWOD chip (Yafia, Ahmadi, Hoorfar, & Najjaran, 2015). These examples are promising but still have problems in sacrificing the actuation efficiency for the portability. It is very possible to make the system super-portable and accessible with a Wi-Fi controller. Every individual device that has a Wi-Fi transceiver will be able to connect to the EWOD DMF device on demand.

In the chapter, we will introduce a low cost ($3) Wi-Fi module (ESP8266, and a comparison with other similar devices in Table A.1) and its interface with the EWOD DMF system and the controlling smart phones or laptops. ESP8266 has a dimension of 14 mm by 24 mm, possesses very few pins, has a reach of over 30+ meters, contains an extensive list of AT commands to easily interface with the device and has an entire community and website dedicated to the development of this chip in terms of software.

The only drawback of the ESP8266 is the low bandwidth but for the given application of product, it is high enough. Table A.1 compares this module to the others on the market.

Table A.1. A comparison of EST8266 to some popular commercial Wi-Fi modules.

Name	Cost	Bandwidth	Size	Max Current	Pins
ESP8266	<$4	<56kbps	1.42cm X 2.45cm	300mA	8
XBee Wi-Fi	<$40	72mbps	2.20cm X 3.4cm	309mA	20
HF-LPB100	<10$	N/A	2.31cm X 3.28cm	200mA	48
HF-LPT100	<8$	N/A	2.2cm X 1.35cm	200mA	10

Table A.2. Different versions of the ESP module

ESP Model	Surface Area (cm^2)	Antenna	FCC Comp.	Price per module	Pin Count
1	3.55	PCB	Yes	$2.97	8
2	2.09	U-FL	Yes		
3	2.12	Ceramic	Yes	$2.93	14
4	1.78	None	Yes	N/A	N/A
5	2.02	U-FL	Yes	N/A	N/A
6	2.09	None	No	N/A	N/A
7	3.52	Ceramic U-FL	No	N/A	N/A
8	2.72	None	No	N/A	N/A
9	1	None	Yes	N/A	N/A
10	1.42	None	Yes	N/A	N/A
11	2.51	Ceramic	Yes	$3.10	8
12	3.84	PCB	Yes	$3.13	16

It's okay to put the tables on one whole page so they aren't discontinuous. In the tables above, price check for ESP Models 02, 04, 05, 06, 07, 08, 09, and 10 are ignored as they are either not FCC compliant or they lack an integrated antenna which would greatly increase the price beyond reasonable possibility of it being cost efficient as well as expanding the size of the ESP module profile. The ESP8266 supports SPI communication to a FTDI converter, allowing for it to be directly programmed through a FTDI converter, connecting directly from a computer to the

ESP8266 module. The FTDI converter also solves the issue of the voltage level difference of USB at 5V and the ESP8266 at 3.3V. A great advantage to using the ESP8266 is its ability to act as itself a Wi-Fi station in the sense that any device (laptop, smartphone, etc.) with Wi-Fi capabilities can directly interface the chip and communicate it to a webpage, offering a seamless experience between any and all devices, making it an extremely portable and practical design to interface with as all that is required is a Wi-Fi device equipped with a web browser.

A.2 Circuits, interfaces, and pins

The overall circuit design is fairly simple. It needs an ESP8266, 6 MCP23017s, 2 10K resistors, a 3.3 V level shifter and three switches. The 3.3 V level shifter is not actually required assuming the power supply to the entire circuit is 3.3 V, however 5 V is much more common as a power supply, so in-effect, the level shifter allows for a power supply of the range of 5.5 V to 3.3 V, allowing for less likelihood of user error in setting up the PCB. The switches are also not completely necessary as the switches exist to allow for programming and runtime mode within the PCB. However, allowing the user to program the ESP after it has been soldered onto the PCB can save a lot of time and money.

The 10 K resistors are needed for the open-drain design of the I2C protocol. When the SCL/SDA line is pulled to ground, it is considered a 0 value, and floating is considered a "1." Therefore, the 10K resistors must be connected to the voltage source and the SDA/SCL. Each SDA/SCL needs its own resistor to the voltage source (Fig. A.1).
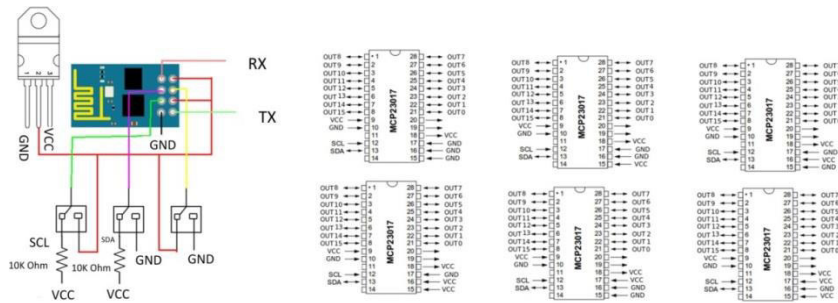
Fig. A.1 ESP8266 connection interfaces with GPIO.

GPIO2 connects to a switch that toggles between an output of SCL and the 3.3 V source from the level shifter. GPIO2 must be set to high to be programmed. GPIO0 connects to a switch that toggles between an output of SDA and GND. GPIO0 must be set to GND to be programmed. Reset connects to a switch that toggles between VCC and GND for the purpose of being able to easily reset the ESP device while in operation in case something goes wrong.

The red electrodes indicate that they are not being excited and the green indicates an electrode that is being excited (Fig. A.2). An electrode can be excited by this interface by simply clicking on the electrode from a web browser. Below is the output of the webpage delivered by the ESP8266 setup displayed on a web-browser on a laptop.
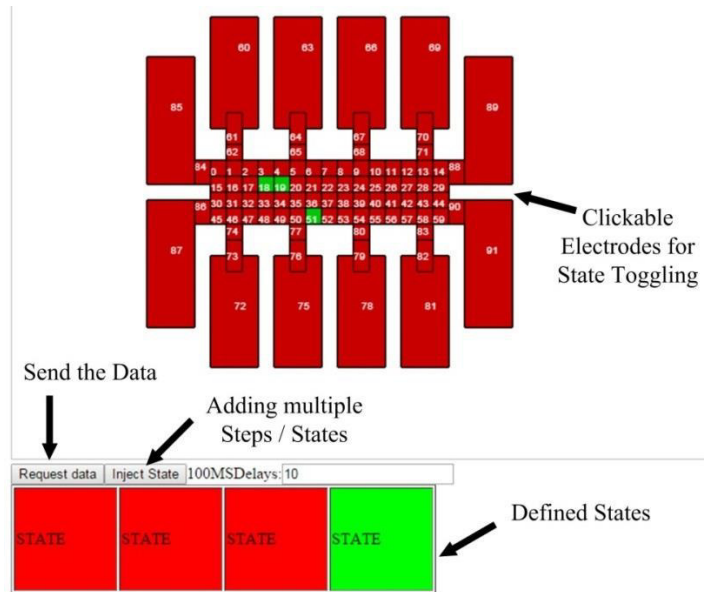
Fig. A.2 The EWOD DMF control panel in a web browser.

A.3 Portable high voltage driver

A highly efficient and portable power supply is used for this system. Instead of using conventional bench bulky equipment, we toggle the high voltage transistors' gates, and successfully achieved up to 10 kHz high voltage pulses (Chapter 2). In the updated driving system that described in Chapter 3, we used mechanical relays as the high voltage switch. The high voltage pulses are directly added to the top right side; the 3.3 V digital signals are from microcontrollers and added to the left top side. However, the high frequency driving voltages will partially penetrable to the capacitors and a 30 V offset will appear at the output, which is undesirable. For a better insulation, we use the optical switch with DC high voltage at the right top side and keep the high voltage transistors' gates toggling all the time (Fig. A.3). The GPIO is totally controlled by the wireless module (ESP8266) using the HTML panel shown in Fig. A.2. The low voltage toggling signal is created by LM555 instead of microcontrollers, which decreases the dimension of the system further.

159
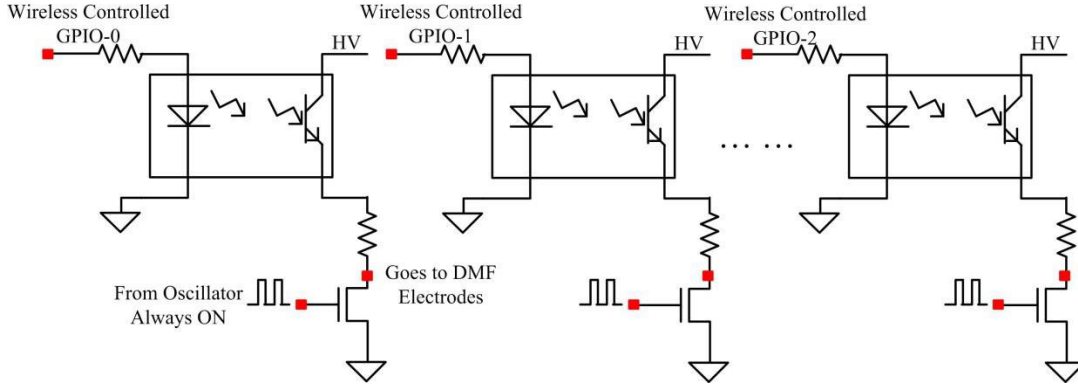
Fig. A.3 The developed portable DMF driving system.

The output frequency of the LM555 timer is tested. Vcc=5V, C=0.01 µF. The charge time is given by:

$$t_1 = 0.693(R_A + R_B)C \tag{A.1}$$

$$t_1 = 0.693(R_B)C \tag{A.2}$$

Thus the total period is:

$$T = t_1 + t_2 = 0.693(R_A + 2R_B)C \tag{A.3}$$

The frequency of oscillation is:

$$f = \frac{1}{T} = \frac{1.44}{(R_A + 2R_B)C} \tag{A.4}$$

The output frequency is plotted versus R_B (Fig. A.4).
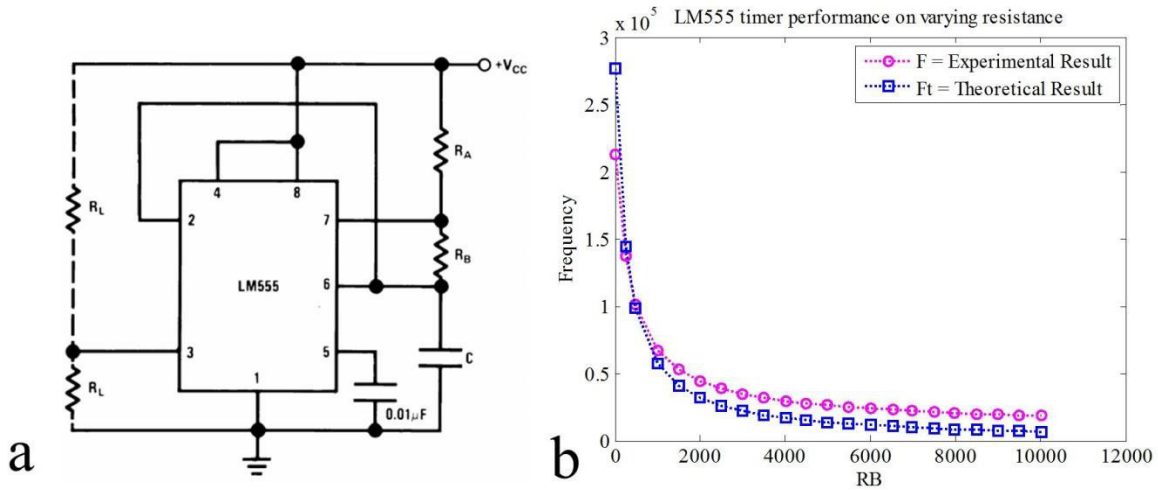
Fig. A.4 The experimental and theoretical output frequency of LM555.

The frequency is adjustable in the range of 200 Hz – 10 kHz by changing the R_B up to 50 kΩ while keeping R_A at 500 Ω. According to Eq. A.1 and A.2, the duty cycle is plotted by varying R_B (Fig. A.5):
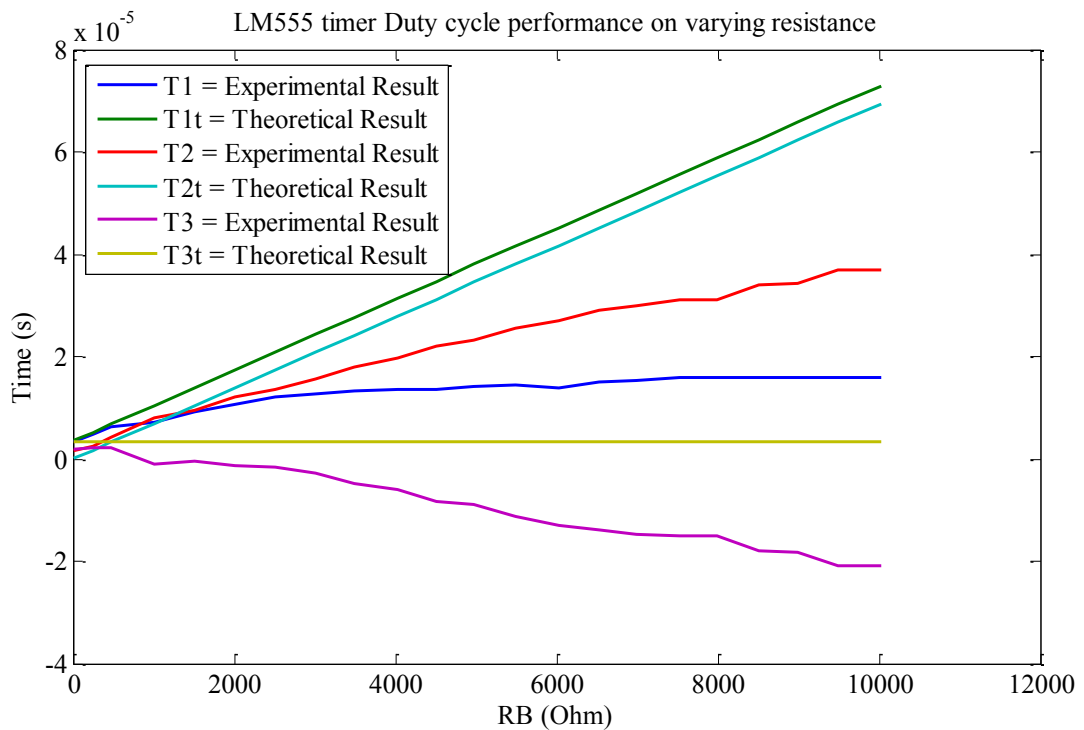
Fig. A.5 LM555 duty cycle varies versus R_B.

The oscillation duty cycle should be close to 50% to ensure the equivalent charging time and the discharging time to the dielectric-liquid capacitor. T1 represents the charging time; T2 means the discharging time; T3=T1-T2. Smaller R_B results in better duty cycle (close to 50%).

The toggling voltages from the LM555 (Fig. A.6) is connected to the gates of the high voltage MOSFET shown in Fig. A.5. The duty cycle is adjustable by changing the resistors. Large drain resistors (>1 MΩ) shown in Fig. A.3 limited the current in the channel, which leads to under-charged pulses seen in Fig. A.6 (the second row) in higher frequencies. Using smaller drain resistors will solve this problem (the third and the fourth row in Fig. A.6). This requires efficient high voltage source to provide enough current for this pulses. The High voltage power source can provide up to 50 mA current under 180 V DC.

The raw signal data of the 5 V toggling pulses are shown in Fig. A.6:
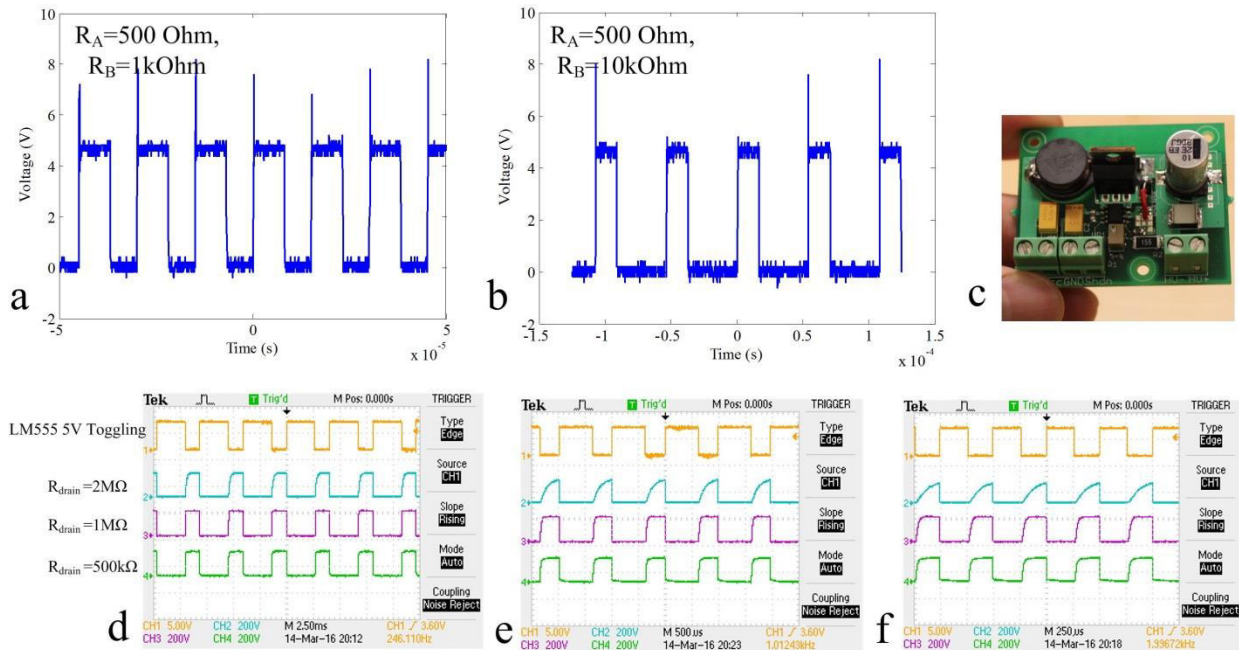
Fig. A.6 The raw data of the output pulses using RB=1 kOhm (a) and 10 kOhm (b). (c) The highly efficient high voltage module (Http://Www.gaudi.ch/GaudiLabs/?page_id=392.). (f-e) A comparison of the 5V toggling pulses and three channels of high voltage pulses with different drain resistors shown in Fig. 6.3. Different pulse frequencies are applied: 250 Hz (d), 1 kHz (e), 2 kHz (f).
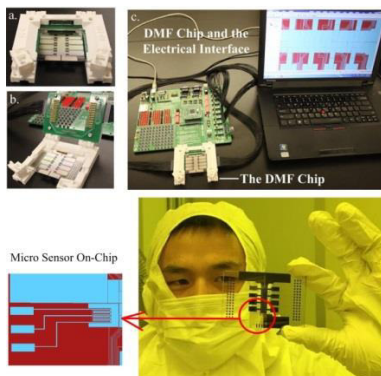
Fig. A.7 Using the 3-D printing pogo-pin interfaces from DropBot (Fobel et al., 2013) as the external control interface. The latest DMF version has a special area for regional heating, cooling, and ultra-sensitive on-chip sensing (marked in the red circle).

The portable high voltage module can work at a high efficiency (85%), and provide up to 50 mA current to drive high speed toggles. The MOSFET-OptoSwitch module shown in Fig. A.3 is new and working very well for the DMF system. The most updated DMF system is shown in Fig. A.7.

A.4 GPIO Expander – MCP23017

In order to actuate 90 different electrodes independently, 90 different GPIO pins are required. No micro-controller or virtually any single device is capable of this. Therefore, a GPIO expander is needed that is capable of 90 different GPIO pins. A question rests on whether SPI or I2C, but due to the ESP8266 only having two GPIO pins, this leaves I2C as the only contender as SPI

requires a minimum of 3 pins to operate. The MCP23017 was selected as the ideal GPIO expander, and using six of these ICs are enough to fully obtain 90 independent GPIOs. Below is a table analyzing different GPIOs and their advantages and disadvantages as well as cost per unit.

Table A.3 Comparison of popular I/O expanders

Name	Voltage	I2C/SPI	GPIOs	Ind. Adr.	Cost $
MCP23017	1.8-5.5	I2C	16	8	1.25
MCP23008	1.8-5.5	I2C	8	8	1.1
TCA9534	1.65-5.5	I2C	8	8	1.6
TCA9538	1.8-5	I2C	8	4	1.75
PCA9534	2.7-5	I2C	8	8	1.71
TCA7408	1.8-3.6	I2C	8	1	2.01
TCA6418E	1.65.-3.6	I2C	18	1	2.27
TCA6424	1.8-5	I2C	24	2	1.4
PCA9535	2.3-5.5	I2C	16	8	2.33

The needed GPIO Expander has several requirements to be used in this design. It must support 3.3 V power supply as that is what the ESP8266 runs on; it must be I2C as ESP8266 only has two free pins; it must support a total of 90 I/O ports, which is calculated by GPIOs × Ind. Adr; and ideally the cost should be minimum. Independent Addressing is where a GPIO IC can have its own address to prevent conflict from other GPIOs. For instance, if there are two GPIOs with the same address, and you write to one, it will write to both, effectively making one

of them useless, thereby the amount of independent addresses does limit it. As based on our needed requirements, all of them support the proper voltage. The XRA1405 does not support I2C. Only MCP23017 and PCA9535 support up to 90 unique GPIO addresses, so ultimately it boils down to which is cheaper, and the MCP23017 is nearly twice as cheap, so clearly the MCP23017 is the winner. Now continuing, the MCP23017 will be discussed in details on its functionality to actually work. The image below is the QFN package of the MCP23017.
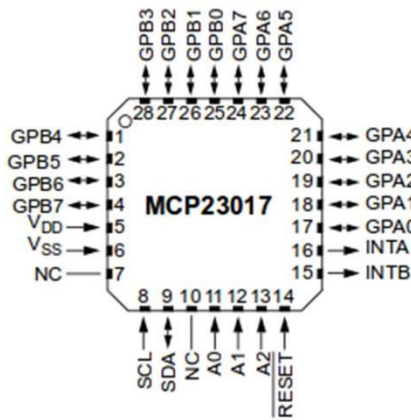
Fig. A.8 MCP23017 QFN package.

The VDD needs to be connected to the 3.3 voltage source and the VSS needs to be connected to the ground. NC stands for no-connect, meaning to leave it floating. INTA/INTB can also be leave floating as we are not concerned about the interrupt output of the MCP23017 (Fig. A.8). RESET should always be connected to high at all times to leave it operating. A0, A1, and A2 are the independent addresses and each MCP23017 needs to be assigned a different identifier value to prevent address conflict. SCL/SDA is the I2C connection protocol pins to the ESP8266. SDA of MCP23017 goes to GPIO2 of ESP8266 and SCL of MCP23017 goes to GPIO0 of ESP8266. GPA0-7 and GPB0-7 are the actual output pins that control the EWOD circuitry. The actual pin identifier to the EWOD circuitry can be calculated as the following: (The bit-wise number representation of A2A1A0, A2 being the most significant bit) × 16 + (suffix number on

165

GPA/GPB) + (If GPB) × 8. For instance, if A2A1A0 = 010, and on pin GPB3, the output representation is 2×16+3+(1)×8 = 43.

Currently the market has products that can give an extensive amount of GPIO pins through the use of certain microcontroller units (MCUs) such as the AT32UC3C 144-pin LQFP IC which delivers 123 GPIO pins. This IC is not easy to use for the purpose of "plug-n-play" as the chip itself cannot be used until it is integrated onto a PCB as it cannot be plugged directly into a breadboard. Furthermore, the price is quite high at over $300 per unit. The solution presented in this study provides a system capable of many GPIO for 10% of the cost. However, the AT32UC3C is capable of much better performance than a nearly 2 mili-second delay per pin output which is the presented solution, but for the given purpose of controlling the EWOD circuitry, this is sufficient. The market also has available Wi-Fi capable devices. However the setting up and running of the ESP8266 is not the most trivial of tasks and solutions online will give fragments of each step needed to complete this communication to the ESP8266 directly as opposed to using an intermediary communicator such as the Arduino. What the market does not have is a final product capable of both Wi-Fi and GPIO integrated into a single circuit. At the reasonable price of $39, this is something the market could do with and benefit. A completed product with software flashed into the ESP8266 allowing for any remote Wi-Fi capable device to access and control the 90+ GPIO pins is something that can be used for many applications and in this specific usage of the EWOD device.

A.5 Programming environment for esp8266

The ability to freely program the ESP8266 is not the easiest task and many guides on the internet do not fully work or have some errors. After numerous testing operating systems and CPU architectures, the only combination that would work was Debian on an x86 processor

running an i386 operating system. Therefore, a freshly formatted Debian 7.0 32 bit operating system was used in setting up an environment to successfully be able to cross compile and flash the ESP8266. The following steps must be performed: installation of the core libraries of the Debian environment, the GCC/Crosstool compiler, the ESP SDK, the Xtensa libraries, the ESP image tool, and ESP uploader. All these steps are also covered in (https://github.com/esp8266/esp8266-wiki/wiki/Toolchain). However it is the intention of this document to not need to go through another website to follow the installation as well as giving some additional clarity on what each step does.

A.6 Installing Debian environemnt libraries

This guide is assuming that the Debian operating system is newly installed without any additional files installed which may cause conflict in the process. Also, it assumes the user has some minimal experience in the Linux environment as well as how to operate a terminal. Note, that an error will be given saying it cannot find a specific package in the Debian 7.0 package manager. It can be ignored and be continued without the specific package.

It should be noted that this is a Debian environment and not an Ubuntu derivative. Therefore you will need to be in root and not use the "sudo" command. To be in root, simply type "su" in terminal and type the password given. "$username" obviously needs to be changed to whatever user you are logged into in the Debian environment. Executing the following commands in terminal will begin installation:

apt-get install git autoconf build-essential gperf bison flex texinfo libtool libncurses5-dev wget gawk libc6-dev-i386 python-serial libexpat-dev

mkdir /opt/Espressif

chown $username /opt/Espressif/

A.7 GCC/Crosstool compiler

The next step is to install the Xtensa cross architectural compiler. This is due to the ESP8266 not running on an x86 processor, meaning its compiled byte code is significantly different from that of an x86 processor. Therefore code compiled on an x86 processor can NOT be used for an ESP8266, yet the code still needs to be compiled on an x86 and then written to the ESP8266 architecture. So to install, type the following in console as root:

cd /opt/Espressif

git clone -b lx106 git://github.com/jcmvbkbc/crosstool-NG.git

cd crosstool-NG

./bootstrap && ./configure --prefix=`pwd` && make && make install

./ct-ng xtensa-lx106-elf

./ct-ng build

PATH=$PWD/builds/xtensa-lx106-elf/bin:$PATH

A.8 ESP SDK installation

Now to actually write ESP code, the ESP SDK is required. This contains the libraries and files necessary for the actual ESP environment. Absolutely make sure you are no longer in root. If you are still in root, type "exit" in the console which will bring you back to the currently logged in user. Now execute the following code (as user!):

cd /opt/Espressif

wget   -O   esp_iot_sdk_v0.9.3_14_11_21.zip   https://github.com/esp8266/esp8266-wiki/raw/master/sdk/esp_iot_sdk_v0.9.3_14_11_21.zip

wget -O esp_iot_sdk_v0.9.3_14_11_21_patch1.zip https://github.com/esp8266/esp8266-wiki/raw/master/sdk/esp_iot_sdk_v0.9.3_14_11_21_patch1.zip

unzip esp_iot_sdk_v0.9.3_14_11_21.zip

unzip esp_iot_sdk_v0.9.3_14_11_21_patch1.zip

mv esp_iot_sdk_v0.9.3 ESP8266_SDK

mv License ESP8266_SDK/

cd /opt/Espressif/ESP8266_SDK

sed -i -e 's/xt-ar/xtensa-lx106-elf-ar/' -e 's/xt-xcc/xtensa-lx106-elf-gcc/' -e 's/xt-objcopy/xtensa-lx106-elf-objcopy/' Makefile

mv examples/IoT_Demo .

A.9 Xtensa libraries

Previously the Xtensa cross-compiler was installed, however, the libraries for the particular target platform of the ESP8266 was not installed. This needs to be done now (once again as user, not root).

cd /opt/Espressif/ESP8266_SDK

wget -O lib/libc.a https://github.com/esp8266/esp8266-wiki/raw/master/libs/libc.a

wget -O lib/libhal.a https://github.com/esp8266/esp8266-wiki/raw/master/libs/libhal.a

wget -O include.tgz https://github.com/esp8266/esp8266-wiki/raw/master/include.tgz

tar -xvzf include.tgz

A.10 ESP image maker

The ESP Image Maker is required to create a file that can be used as the new data to write to the ESP8266. You need a CD/DVD burner such as an .iso file. First an .iso file needs to be generated on the local machine and then written to the external device. Execute the following commands (once again as user, not root).

cd /opt/Espressif

wget   -O   esptool_0.0.2-1_i386.deb   https://github.com/esp8266/esp8266-wiki/raw/master/deb/esptool_0.0.2-1_i386.deb

dpkg -i esptool_0.0.2-1_i386.deb

A.11 ESP uploader

Now with the image maker installed, we need a tool to which can actually write the image to the ESP device. So execute the following:

cd /opt/Espressif

git clone https://github.com/themadinventor/esptool esptool-py

ln -s $PWD/esptool-py/esptool.py crosstool-NG/builds/xtensa-lx106-elf/bin/

Blinky Base Code:

The code was based off the blinky makefile and libraries, and so therefore this one will be as well. So execute these commands in terminal:

cd /opt/Espressif

git clone https://github.com/esp8266/source-code-examples.git

cd source-code-examples/blinky

make

If it compiles successfully, move the source code files for the EWOD water moving code to the blinky folder. Remember to type "make" when inside the blinky folder with the new code. Now to actually flash the ESP, make sure to be in the root directory of the blinky program and execute the following command:

sudo make ESPPORT=/dev/ttyUSB0 flash

If it gives an error about unable to connect, check to make sure all pins are successfully connected as specified. Also, if the ESP was in runtime mode, it will need to be reset by toggling the reset pin between the high/low by moving it from high to low, then back to high. Remember, RESET is on when its voltage is GND and RESET is off when its voltage is VCC. Also, the GPIO0 and GPIO2 will need to be put into flash mode. All these steps of configuring the physical connection to flash are in the section of "Flashing the ESP8266."

To flash the ESP8266 it is required to have some communication device from the ESP8266 to the computer. However, the computer itself can not directly accomplish this. Therefore, an additional device is needed, namely an FTDI chip. An FTDI chip allows for high bandwidth serial communication between a computer and the ESP8266, allowing for it to be configured. The FTDI chip must have a 3.3V communication setting or it will not work as USB operates on 5V and ESP8266 operates on 3.3V. It is recommended to buy an OSEPP FTDI breakout board as it supports both 3.3 V and 5 V communication, as well as its pins supporting both male and female solving for any pin configuration headache. The image below shows the OSEPP FTDI

breakout board. Note, that right now it is binded to 5V due to the jumper. If the jumper is moved up a pin to the 3v3, it will then act on 3.3V. This is required.
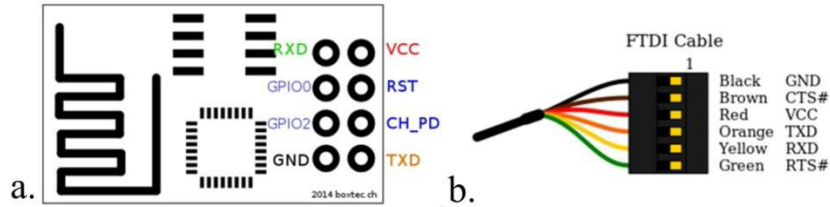
Fig. A.9 (a) ESP8266 module layout. (b) FTDI converter.

Connect the RX/TX pins in a 3v3 FTDI cable to the TX/RX pins in the ESP module. Connect a 3v3 power supply to the VCC/GND pins. Note that it is possible to use an Arduino 3v3 supply for this. Connect the CH_PID pin to VCC as well. The rest of the pins should be floating. However, be prepared to occasionally ground the RST pin. This would help if the board is stuck on some command.

In addition, connect a USB cable from the computer to the FTDI Breakout Board. Now hopefully the device is on and able to communicate. If all is connected, it will begin to flash and it will take a few minutes. Under NO circumstances should you allow the power to fail. If power drops, the firmware will only be partially updated, resulting in a corrupted ROM and the end of the ESP8266. Now the ESP8266 should have an updated firmware.

A.12 Conclusion

This Appendix covers a portable DMF driving system controlled by a smart Wi-Fi to serial converter. Several innovations have been described in detail. A highly efficient portable high voltage supply and driving circuit is used to create the driving voltage. The toggling frequency can be adjusted by simply changing the LM555 external resistors. Theoretical and experimental results have a good agreement with each other.

References

Abdelgawad, M., & Wheeler, A. R. (2007). Rapid prototyping in copper substrates for digital microfluidics. *Advanced Materials, 19*(1), 133-137.

Abdelgawad, M., & Wheeler, A. R. (2008). Low-cost, rapid-prototyping of digital microfluidics devices. *Microfluidics and Nanofluidics, 4*(4), 349-355.

Abdelgawad, M., & Wheeler, A. R. (2009). The digital revolution: A new paradigm for microfluidics. *Advanced Materials, 21*(8), 920-925.

Alvarez, M., Friend, J., & Yeo, L. Y. (2008). Rapid generation of protein aerosols and nanoparticles via surface acoustic wave atomization. *Nanotechnology, 19*(45), 455103.

Alvarez, M., Yeo, L. Y., Friend, J. R., & Jamriska, M. (2009). Rapid production of protein-loaded biodegradable microparticles using surface acoustic waves. *Biomicrofluidics, 3*(1), 014102.

Analog Devices.Extending the capacitive input range of AD7745/AD7746.

Avramov-Zamurovic, S., & Lee, R. D. (2009). A high-stability capacitance sensor system and its evaluation. *Instrumentation and Measurement, IEEE Transactions On, 58*(4), 955-961.

Baird, E., Young, P., & Mohseni, K. (2007). Electrostatic force calculation for an EWOD-actuated droplet. *Microfluidics and Nanofluidics, 3*(6), 635-644.

Banerjee, A. N., Qian, S., & Joo, S. W. (2011). High-speed droplet actuation on single-plate electrode arrays. *Journal of Colloid and Interface Science, 362*(2), 567-574.

Baratian, D., Cavalli, A., van den Ende, D., & Mugele, F. (2015). On the shape of a droplet in a wedge: New insight from electrowetting. *Soft Matter,*

Barbulovic-Nad, I., Yang, H., Park, P. S., & Wheeler, A. R. (2008). Digital microfluidics for cell-based assays. *Lab on a Chip, 8*(4), 519-526.

Bashash, S., & Jalili, N. (2007). Robust multiple frequency trajectory tracking control of piezoelectrically driven micro/nanopositioning systems. *Control Systems Technology, IEEE Transactions On, 15*(5), 867-878.

Basu, A. S. (2013). Droplet morphometry and velocimetry (DMV): A video processing software for time-resolved, label-free tracking of droplet parameters. *Lab on a Chip, 13*(10), 1892-1901.

Bazghaleh, M., Grainger, S., Mohammadzaheri, M., Cazzolato, B., & Lu, T. (2013). A digital charge amplifier for hysteresis elimination in piezoelectric actuators. *Smart Materials and Structures, 22*(7), 075016.

Beaulieu, L., Godin, M., Laroche, O., Tabard-Cossa, V., & Grütter, P. (2007). A complete analysis of the laser beam deflection systems used in cantilever-based systems. *Ultramicroscopy, 107*(4), 422-430.

Berthier, J., Dubois, P., Clementz, P., Claustre, P., Peponnet, C., & Fouillet, Y. (2007). Actuation potentials and capillary forces in electrowetting based microsystems. *Sensors and Actuators A: Physical, 134*(2), 471-479.

Besant, J. D., Sargent, E. H., & Kelley, S. O. (2015). Rapid electrochemical phenotypic profiling of antibiotic-resistant bacteria. *Lab on a Chip, 15*(13), 2799-2807.

Bhattacharjee, P., McDonnell, A., Prabhakar, R., Yeo, L., & Friend, J. (2011). Extensional flow of low-viscosity fluids in capillary bridges formed by pulsed surface acoustic wave jetting. *New Journal of Physics, 13*(2), 023005.

Borcia, R., Borcia, I. D., & Bestehorn, M. (2014). Can vibrations control drop motion? *Langmuir, 30*(47), 14113-14117.

Brassard, D., Malic, L., Normandin, F., Tabrizian, M., & Veres, T. (2008). Water-oil core-shell droplets for electrowetting-based digital microfluidic devices. *Lab on a Chip, 8*(8), 1342-1349.

Brunet, P., Eggers, J., & Deegan, R. (2007). Vibration-induced climbing of drops. *Physical Review Letters, 99*(14), 144501.

Buguin, A., Talini, L., & Silberzan, P. (2002). Ratchet-like topological structures for the control of microdrops. *Applied Physics A, 75*(2), 207-212.

Bush, J. W., Peaudecerf, F., Prakash, M., & Quéré, D. (2010). On a tweezer for droplets. *Advances in Colloid and Interface Science, 161*(1), 10-14.

Chang, C., Bostwick, J. B., Steen, P. H., & Daniel, S. (2013). Substrate constraint modifies the rayleigh spectrum of vibrating sessile drops. *Physical Review E, 88*(2), 023015.

Chang, J., Choi, D. Y., Han, S., & Pak, J. J. (2010). Driving characteristics of the electrowetting-on-dielectric device using atomic-layer-deposited aluminum oxide as the dielectric. *Microfluidics and Nanofluidics, 8*(2), 269-273.

Chen, C., Tsai, S., Chen, M., & Jang, L. (2011). Effects of gap height, applied frequency, and fluid conductivity on minimum actuation voltage of electrowetting-on-dielectric and liquid dielectrophoresis. *Sensors and Actuators B: Chemical, 159*(1), 321-327.

Chen, T., Dong, C., Gao, J., Jia, Y., Mak, P., Vai, M., & Martins, R. P. (2014). Natural discharge after pulse and cooperative electrodes to enhance droplet velocity in digital microfluidics. *AIP Advances, 4*(4), 047129.

Chen, T., Jia, Y., Dong, C., Gao, J., Mak, P., & Martins, R. P. (2016). Sub-7-second genotyping of single-nucleotide polymorphism by high-resolution melting curve analysis on a thermal digital microfluidic device. *Lab on a Chip,16, 743-752.*

Chi, Z., Jia, M., & Xu, Q. (2014). Fuzzy PID feedback control of piezoelectric actuator with feedforward compensation. *Mathematical Problems in Engineering, 2014.*

Cho, S. K., Moon, H., & Kim, C. (2003). Creating, transporting, cutting, and merging liquid droplets by electrowetting-based actuation for digital microfluidic circuits. *Microelectromechanical Systems, Journal Of, 12*(1), 70-80.

Choi, H., Cheung, J., Kim, S., & Ahn, J. (2011). Structural dynamic displacement vision system using digital image processing. *NDT & E International, 44*(7), 597-608.

Choi, K., Ng, A. H., Fobel, R., & Wheeler, A. R. (2012). Digital microfluidics. *Annual Review of Analytical Chemistry, 5*, 413-440.

Cooney, C. G., Chen, C., Emerling, M. R., Nadim, A., & Sterling, J. D. (2006). Electrowetting droplet microfluidics on a single planar surface. *Microfluidics and Nanofluidics, 2*(5), 435-446.

Cruz, P., Mari, A., & Roca, P. (1998). Nonlinear time-dependent analysis of segmentally constructed structures. *Journal of Structural Engineering, 124*(3), 278-287.

Curtis, A. S., Reid, S., Martin, I., Vaidyanathan, R., Smith, C., Nikukar, H., & Dalby, M. J. (2013). Cell interactions at the nanoscale: Piezoelectric stimulation. *NanoBioscience, IEEE Transactions On, 12*(3), 247-254.

Daniel, S., & Chaudhury, M. K. (2002). Rectified motion of liquid drops on gradient surfaces induced by vibration. *Langmuir, 18*(9), 3404-3407.

Daniel, S., Chaudhury, M. K., & De Gennes, P. (2005). Vibration-actuated drop motion on surfaces for batch microfluidic processes. *Langmuir, 21*(9), 4240-4248.

Daniel, S., Sircar, S., Gliem, J., & Chaudhury, M. K. (2004). Ratcheting motion of liquid drops on gradient surfaces. *Langmuir, 20*(10), 4085-4092.

Daniel, S., Chaudhury, M. K., & Chen, J. C. (2001). Fast drop movements resulting from the phase change on a gradient surface. *Science (New York, N.Y.), 291*(5504), 633-636.

DeVoria, A., & Mohseni, K. (2015). Droplets in an axisymmetric microtube: Effects of aspect ratio and fluid interfaces. *Physics of Fluids (1994-Present), 27*(1), 012002.

Dong, C., Chen, T., Gao, J., Jia, Y., Mak, P., Vai, M., & Martins, R. P. (2014). On the droplet velocity and electrode lifetime of digital microfluidics: Voltage actuation techniques and comparison. *Microfluidics and Nanofluidics, ,* 1-11.

Dryden, M. D., Rackus, D. D., Shamsi, M. H., & Wheeler, A. R. (2013). Integrated digital microfluidic platform for voltammetric analysis. *Analytical Chemistry, 85*(18), 8809-8816.

Dupre, L. R., Van Keer, R., & Melkebeek, J. A. (1999). Identification of the relation between the material parameters in the preisach model and in the Jiles–Atherton hysteresis model. *Journal of Applied Physics, 85*(8), 4376-4378.

Elbuken, C., Glawdel, T., Chan, D., & Ren, C. L. (2011). Detection of microdroplet size and speed using capacitive sensors. *Sensors and Actuators A: Physical, 171*(2), 55-62.

Eydelnant, I. A., Uddayasankar, U., Liao, M. W., & Wheeler, A. R. (2012). Virtual microwells for digital microfluidic reagent dispensing and cell culture. *Lab on a Chip, 12*(4), 750-757.

Fair, R. B. (2007). Digital microfluidics: Is a true lab-on-a-chip possible? *Microfluidics and Nanofluidics, 3*(3), 245-281.

Fairbairn, M., & Moheimani, S. (2013). Sensorless enhancement of an atomic force microscope micro-cantilever quality factor using piezoelectric shunt control. *Review of Scientific Instruments, 84*(5), 053706.

Fleming, A. J., & Leang, K. K. (2014). Types of nanopositioners. *Design, modeling and control of nanopositioning systems* (pp. 43-55) Springer.

Fobel, R., Fobel, C., & Wheeler, A. R. (2013). DropBot: An open-source digital microfluidic control system with precise control of electrostatic driving force and instantaneous drop velocity measurement. *Applied Physics Letters, 102*(19), 193513.

Fobel, R., Kirby, A. E., Ng, A. H., Farnood, R. R., & Wheeler, A. R. (2014). Paper microfluidics goes digital. *Advanced Materials, 26*(18), 2838-2843.

Friend, J. R., Yeo, L. Y., Arifin, D. R., & Mechler, A. (2008). Evaporative self-assembly assisted synthesis of polymeric nanoparticles by surface acoustic wave atomization. *Nanotechnology, 19*(14), 145301.

Friend, J., & Yeo, L. Y. (2011). Microscale acoustofluidics: Microfluidics driven via acoustics and ultrasonics. *Reviews of Modern Physics, 83*(2), 647.

Fukuda, Y., Feng, M. Q., Narita, Y., Kaneko, S., & Tanaka, T. (2013). Vision-based displacement sensor for monitoring dynamic response using robust object search algorithm. *Sensors Journal, IEEE, 13*(12), 4725-4732.

Gao, J., Liu, X., Chen, T., Mak, P., Du, Y., Vai, M., . . . Martins, R. P. (2013). An intelligent digital microfluidic system with fuzzy-enhanced feedback for multi-droplet manipulation. *Lab on a Chip, 13*(3), 443-451.

Ge, P., & Jouaneh, M. (1995). Modeling hysteresis in piezoceramic actuators. *Precision Engineering, 17*(3), 211-221.

Ghafar-Zadeh, E., & Sawan, M. (2007). A hybrid microfluidic/CMOS capacitive sensor dedicated to lab-on-chip applications. *Biomedical Circuits and Systems, IEEE Transactions On, 1*(4), 270-277.

Ghafar-Zadeh, E., & Sawan, M. (2008). Charge-based capacitive sensor array for cmos-based laboratory-on-chip applications. *Sensors Journal, IEEE, 8*(4), 325-332.

Ghafar-Zadeh, E., Sawan, M., & Therriault, D. (2009). CMOS based capacitive sensor laboratory-on-chip: A multidisciplinary approach. *Analog Integrated Circuits and Signal Processing, 59*(1), 1-12.

Goldfarb, M., & Celanovic, N. (1997). A lumped parameter electromechanical model for describing the nonlinear behavior of piezoelectric actuators. *Journal of Dynamic Systems, Measurement, and Control, 119*(3), 478-485.

Gong, J. (2008). All-electronic droplet generation on-chip with real-time feedback control for EWOD digital microfluidics. *Lab on a Chip, 8*(6), 898-906.

Gong, J., Cha, G., Ju, Y. S., & Kim, C. (2008). Thermal switches based on coplanar EWOD for satellite thermal control. Paper presented at the *Micro Electro Mechanical Systems, 2008. MEMS 2008. IEEE 21st International Conference On,* 848-851.

Gong, J., Fan, S., & Kim, C. (2004). Portable digital microfluidics platform with active but disposable lab-on-chip. Paper presented at the *Micro Electro Mechanical Systems, 2004. 17th IEEE International Conference on.(MEMS),* 355-358.

Greenspan, H. P. (1978). On the motion of a small viscous droplet that wets a surface. *Journal of Fluid Mechanics, 84*(01), 125-143.

Heng, X., & Luo, C. (2014). Bioinspired plate-based fog collectors. *ACS Applied Materials & Interfaces, 6*(18), 16257-16266.

Hodgson, R. P., Tan, M., Yeo, L., & Friend, J. (2009). Transmitting high power rf acoustic radiation via fluid couplants into superstrates for microfluidics. *Applied Physics Letters, 94*(2), 024102.

Hong, J., Kim, Y. K., Kang, K. H., Oh, J. M., & Kang, I. S. (2013). Effects of drop size and viscosity on spreading dynamics in DC electrowetting. *Langmuir, 29*(29), 9118-9125.

Hong, J., Park, J. K., Koo, B., Kang, K. H., & Suh, Y. K. (2013). Drop transport between two non-parallel plates via AC electrowetting-driven oscillation. *Sensors and Actuators B: Chemical, 188*, 637-643.

Hong, S., Chou, T., Chan, S. H., Sheng, Y., & Tsao, H. (2012). Droplet compression and relaxation by a superhydrophobic surface: Contact angle hysteresis. *Langmuir, 28*(13), 5606-5613.

Http://Cmosedu.com/cmos1/electric/electric.htm.

Http://Www.gaudi.ch/GaudiLabs/?page_id=392.

Ink-jet printers zoom into the office market. (1979). *New Scientist, 480.*

Kang, D., Ali, M. M., Zhang, K., Huang, S. S., Peterson, E., Digman, M. A., .Zhao, W. (2014). Rapid detection of single bacteria in unprocessed blood using integrated comprehensive droplet digital detection. *Nature Communications, 5, 1-10.*

Khazalpour, S., & Nematollahi, D. (2014). Electrochemical study of alamar blue (resazurin) in aqueous solutions and room-temperature ionic liquid 1-butyl-3-methylimidazolium tetrafluoroborate at a glassy carbon electrode. *RSC Advances, 4*(17), 8431-8438.

Kim, H., Jebrail, M. J., Sinha, A., Bent, Z. W., Solberg, O. D., Williams, K. P.,. Meagher, R. J. (2013). A microfluidic DNA library preparation platform for next-generation sequencing. *PloS One, 8*(7), e68988.

Kim, M., Pan, M., Gai, Y., Pang, S., Han, C., Yang, C., & Tang, S. K. (2015). Optofluidic ultrahigh-throughput detection of fluorescent drops. *Lab on a Chip, 15*(6), 1417-1423.

Kim, M. S., Kim, T., Kong, S., Kwon, S., Bae, C. Y., Choi, J.,. Park, J. (2010). Breast cancer diagnosis using a microfluidic multiplexed immunohistochemistry platform. *PloS One, 5*(5), e10441.

Kim, N., Hong, S., Park, S., & Hong, Y. (2006). The movement of micro droplet with the effects of dielectric layer and hydrophobic surface treatment with RF atmospheric plasma in EWOD structure. Paper presented at the *Journal of Physics: Conference Series, , 34*(1) 650.

Kim, H., Bartsch, M. S., Renzi, R. F., He, J., Van de Vreugde, J. L., Claudnic, M. R., & Patel, K. D. (2011). Automated digital microfluidic sample preparation for next-generation DNA sequencing. *Journal of Laboratory Automation, 16*(6), 405-414.

Kirby, A. E., & Wheeler, A. R. (2013). Microfluidic origami: A new device format for in-line reaction monitoring by nanoelectrospray ionization mass spectrometry. *Lab on a Chip, 13*(13), 2533-2540.

Koo, B., & Kim, C. (2013). Evaluation of repeated electrowetting on three different fluoropolymer top coatings. *Journal of Micromechanics and Microengineering, 23*(6), 067002.

Kranz, C., Friedbacher, G., Mizaikoff, B., Lugstein, A., Smoliner, J., & Bertagnolli, E. (2001). Integrating an ultramicroelectrode in an AFM cantilever: Combined technology for enhanced information. *Analytical Chemistry, 73*(11), 2491-2500.

Kuntaegowdanahalli, S. S., Bhagat, A. A. S., Kumar, G., & Papautsky, I. (2009). Inertial microfluidics for continuous particle separation in spiral microchannels. *Lab on a Chip, 9*(20), 2973-2980.

Kwapiszewski, R., Skolimowski, M., Ziółkowska, K., Jędrych, E., Chudy, M., Dybko, A., & Brzózka, Z. (2011). A microfluidic device with fluorimetric detection for intracellular components analysis. *Biomedical Microdevices, 13*(3), 431-440.

Li, F., & Mugele, F. (2008). How to make sticky surfaces slippery: Contact angle hysteresis in electrowetting with alternating voltage. *Applied Physics Letters, 92*(24), 244108.

Li, H., Friend, J., Yeo, L., Dasvarma, A., & Traianedes, K. (2009). Effect of surface acoustic waves on the viability, proliferation and differentiation of primary osteoblast-like cells. *Biomicrofluidics, 3*(3), 034102.

183

Li, Y., Fu, Y., Brodie, S., Alghane, M., & Walton, A. (2012). Integrated microfluidics system

    using surface acoustic wave and electrowetting on dielectrics technology. *Biomicrofluidics,*

    6(1), 012812.

Li, Y., Parkes, W., Haworth, L. I., Ross, A., Stevenson, J., & Walton, A. J. (2008). Room-

    temperature fabrication of anodic tantalum pentoxide for low-voltage electrowetting on

    dielectric (EWOD). *Microelectromechanical Systems, Journal Of, 17*(6), 1481-1488.

Li, Y., Baker, R. J., & Raad, D. (2016). Improving the performance of electrowetting on

    dielectric microfluidics using piezoelectric top plate control. *Sensors and Actuators B:*

    Chemical, 229, 63-74.

Li, Y., Chen, R., & Baker, R. J. (2014). A fast fabricating electro-wetting platform to implement

    large droplet manipulation. Paper presented at the *Circuits and Systems (MWSCAS), 2014*

    IEEE 57th International Midwest Symposium On, 326-329.

Li, Y., Li, H., & Baker, R. J. (2014). Volume and concentration identification by using an

    electrowetting on dielectric device. Paper presented at the *Circuits and Systems Conference*

    (DCAS), 2014 IEEE Dallas, 1-4.

Li, Y., Tian, X., Qian, L., Yu, X., & Jiang, W. (2011). Anodal transcranial direct current

    stimulation relieves the unilateral bias of a rat model of parkinson's disease. Paper presented

    at the *Engineering in Medicine and Biology Society, EMBC, 2011 Annual International*

    Conference of the IEEE, 765-768.

Li, Y., Li, H., & Baker, R. J. (2015). A low-cost and high-resolution droplet position detector for an intelligent electrowetting on dielectric device. *Journal of Laboratory Automation, 20*(6), 663-669.

Lin, Y., Evans, R. D., Welch, E., Hsu, B., Madison, A. C., & Fair, R. B. (2010). Low voltage electrowetting-on-dielectric platform using multi-layer insulators. *Sensors and Actuators B: Chemical, 150*(1), 465-470.

Longley, J. E., Dooley, E., Givler, D. M., Napier III, W. J., Chaudhury, M. K., & Daniel, S. (2012). Drop motion induced by repeated stretching and relaxation on a gradient surface with hysteresis. *Langmuir, 28*(39), 13912-13918.

Luo, C., Heng, X., & Xiang, M. (2014). Behavior of a liquid drop between two nonparallel plates. *Langmuir, 30*(28), 8373-8380.

Mach, A. J., & Di Carlo, D. (2010). Continuous scalable blood filtration device using inertial microfluidics. *Biotechnology and Bioengineering, 107*(2), 302-311.

Mayergoyz, I. D. (1986). Mathematical models of hysteresis. *Magnetics, IEEE Transactions On, 22*(5), 603-608.

Medoro, G., Manaresi, N., Leonardi, A., Altomare, L., Tartagni, M., & Guerrieri, R. (2003). A lab-on-a-chip for cell detection and manipulation. *Sensors Journal, IEEE, 3*(3), 317-325.

Mei, N., Seale, B., Ng, A. H., Wheeler, A. R., & Oleschuk, R. (2014). Digital microfluidic platform for human plasma protein depletion. *Analytical Chemistry, 86*(16), 8466-8472.

Moon, H., Cho, S. K., & Garrell, R. L. (2002). Low voltage electrowetting-on-dielectric. *Journal of Applied Physics, 92*(7), 4080-4087.

Mugele, F. (2009). Fundamental challenges in electrowetting: From equilibrium shapes to contact angle saturation and drop dynamics. *Soft Matter, 5*(18), 3377-3384.

Mugele, F., & Baret, J. (2005). Electrowetting: From basics to applications. *Journal of Physics: Condensed Matter, 17*(28), R705.

Murade, C., van den Ende, D., & Mugele, F. (2011). Electrically assisted drop sliding on inclined planes. *Applied Physics Letters, 98*(1), 014102.

Murran, M. A., & Najjaran, H. (2012a). Direct current pulse train actuation to enhance droplet control in digital microfluidics. *Applied Physics Letters, 101*(14), 144102.

Murran, M. A., & Najjaran, H. (2012b). Capacitance-based droplet position estimator for digital microfluidic devices. *Lab on a Chip, 12*(11), 2053-2059.

Nanayakkara, Y. S., Perera, S., Bindiganavale, S., Wanigasekara, E., Moon, H., & Armstrong, D. W. (2010). The effect of AC frequency on the electrowetting behavior of ionic liquids. *Analytical Chemistry, 82*(8), 3146-3154.

Nelson, W. C., & Kim, C. '. (2012). Droplet actuation by electrowetting-on-dielectric (EWOD): A review. *Journal of Adhesion Science and Technology, 26*(12-17), 1747-1771.

Nelson, C. S., Fuller, C. K., Fordyce, P. M., Greninger, A. L., Li, H., & DeRisi, J. L. (2013). Microfluidic affinity and ChIP-seq analyses converge on a conserved FOXP2-binding motif

in chimp and human, which enables the detection of evolutionarily novel targets. *Nucleic Acids Research, 41*(12), 5991-6004.

Nery, E. W., Jastrzębska, E., Żukowski, K., Wróblewski, W., Chudy, M., & Ciosek, P. (2014). Flow-through sensor array applied to cytotoxicity assessment in cell cultures for drug-testing purposes. *Biosensors and Bioelectronics, 51*, 55-61.

Ng, A. H., Chamberlain, M. D., Situ, H., Lee, V., & Wheeler, A. R. (2015). Digital microfluidic immunocytochemistry in single cells. *Nature Communications, 6, 1-10.*

Ng, A. H., Choi, K., Luoma, R. P., Robinson, J. M., & Wheeler, A. R. (2012). Digital microfluidic magnetic separation for particle-based immunoassays. *Analytical Chemistry, 84*(20), 8805-8812.

Ng, A. H., Uddayasankar, U., & Wheeler, A. R. (2010). Immunoassays in microfluidic systems. *Analytical and Bioanalytical Chemistry, 397*(3), 991-1007.

Ng, A. H., Lee, M., Choi, K., Fischer, A. T., Robinson, J. M., & Wheeler, A. R. (2015). Digital microfluidic platform for the detection of rubella infection and immunity: A proof of concept. *Clinical Chemistry, 61*(2), 420-429.

Noblin, X., Kofman, R., & Celestini, F. (2009). Ratchetlike motion of a shaken drop. *Physical Review Letters, 102*(19), 194504.

O'Brien, J., Wilson, I., Orton, T., & Pognan, F. (2000). Investigation of the alamar blue (resazurin) fluorescent dye for the assessment of mammalian cell cytotoxicity. *European Journal of Biochemistry, 267*(17), 5421-5426.

Orlandi, P. A., & Lampel, K. A. (2000). Extraction-free, filter-based template preparation for rapid and sensitive PCR detection of pathogenic parasitic protozoa. *Journal of Clinical Microbiology, 38*(6), 2271-2277.

Paik, P., Pamula, V. K., & Fair, R. B. (2003). Rapid droplet mixers for digital microfluidic systems. *Lab on a Chip, 3*(4), 253-259.

Pollack, M., Shenderov, A., & Fair, R. (2002). Electrowetting-based actuation of droplets for integrated microfluidics. *Lab on a Chip, 2*(2), 96-101.

Pollack, M. G., Fair, R. B., & Shenderov, A. D. (2000). Electrowetting-based actuation of liquid droplets for microfluidic applications. *Applied Physics Letters, 77*(11), 1725-1726.

Prakash, M., Quere, D., & Bush, J. W. (2008). Surface tension transport of prey by feeding shorebirds: The capillary ratchet. *Science (New York, N.Y.), 320*(5878), 931-934.

Qiu, Z., Zhang, X., & Zhang, X. (2014). A vision-based vibration sensing and active control for a piezoelectric flexible cantilever plate. *Journal of Vibration and Control, ,* 1077546314536752.

Quinn, A., Sedev, R., & Ralston, J. (2003). Influence of the electrical double layer in electrowetting. *The Journal of Physical Chemistry B, 107*(5), 1163-1169.

Rackus, D. G., Shamsi, M. H., & Wheeler, A. R. (2015). Electrochemistry, biosensors and microfluidics: A convergence of fields. *Chemical Society Reviews.*

Rayleigh, L. (1879). On the capillary phenomena of jets. Paper presented at the *Proc. R. Soc.*
London, , 29(196-199) 71-97.

Ren, H., & Fair, R. B. (2002). Micro/nano liter droplet formation and dispensing by capacitance
metering and electrowetting actuation. Paper presented at the *Nanotechnology, 2002. IEEE-*
NANO 2002. Proceedings of the 2002 2nd IEEE Conference On, 369-372.

Ren, H., Fair, R. B., & Pollack, M. G. (2004). Automated on-chip droplet dispensing with
volume control by electro-wetting actuation and capacitance metering. *Sensors and*
Actuators B: Chemical, 98(2), 319-327.

Renvoisé, P., Bush, J., Prakash, M., & Quéré, D. (2009). Drop propulsion in tapered tubes. *EPL*
(Europhysics Letters), 86(6), 64003.

Ribeiro, D., Calçada, R., Ferreira, J., & Martins, T. (2014). Non-contact measurement of the
dynamic displacement of railway bridges using an advanced video-based system.
Engineering Structures, 75, 164-180.

Robert, G., Damjanovic, D., Setter, N., & Turik, A. (2001). Preisach modeling of piezoelectric
nonlinearity in ferroelectric ceramics. *Journal of Applied Physics, 89*(9), 5067-5074.

Rubega, M. A., & Obst, B. S. (1993). Surface-tension feeding in phalaropes: Discovery of a
novel feeding mechanism. *The Auk,* 169-178.

Salawu, O. S., & Williams, C. (1995). Bridge assessment using forced-vibration testing. *Journal*
of Structural Engineering, 121(2), 161-173.

Schertzer, M., Ben Mrad, R., & Sullivan, P. (2012). Automated detection of particle
concentration and chemical reactions in EWOD devices. *Sensors and Actuators B:
Chemical, 164*(1), 1-6.

Schertzer, M., Ben-Mrad, R., & Sullivan, P. E. (2010). Using capacitance measurements in
EWOD devices to identify fluid composition and control droplet mixing. *Sensors and
Actuators B: Chemical, 145*(1), 340-347.

Seo, M., Nie, Z., Xu, S., Mok, M., Lewis, P. C., Graham, R., & Kumacheva, E. (2005).
Continuous microfluidic reactors for polymer particles. *Langmuir, 21*(25), 11614-11622.

Shamsi, M. H., Choi, K., Ng, A. H., & Wheeler, A. R. (2014). A digital microfluidic
electrochemical immunoassay. *Lab on a Chip, 14*(3), 547-554.

Shen, H., Fan, S., Kim, C., & Yao, D. (2014). EWOD microfluidic systems for biomedical
applications. *Microfluidics and Nanofluidics, 16*(5), 965-987.

Shih, S. C., Yang, H., Jebrail, M. J., Fobel, R., McIntosh, N., Al-Dirbashi, O. Y.,. Wheeler, A. R.
(2012). Dried blood spot analysis by digital microfluidics coupled to nanoelectrospray
ionization mass spectrometry. *Analytical Chemistry, 84*(8), 3731-3738.

Sładek, J., Ostrowska, K., Kohut, P., Holak, K., Gąska, A., & Uhl, T. (2013). Development of a
vision based deflection measurement system and its accuracy assessment. *Measurement,
46*(3), 1237-1249.

Song, G., Zhao, J., Zhou, X., Abreu-García, D., & Alexis, J. (2005). Tracking control of a

    piezoceramic actuator with hysteresis compensation using inverse preisach model.

    Mechatronics, IEEE/ASME Transactions On, 10(2), 198-209.

Song, J., Evans, R., Lin, Y., Hsu, B., & Fair, R. (2009). A scaling model for electrowetting-on-

    dielectric microfluidic actuators. *Microfluidics and Nanofluidics, 7*(1), 75-89.

Sun, J., Zhang, J., Liu, Z., & Zhang, G. (2013). A vision measurement model of laser

    displacement sensor and its calibration method. *Optics and Lasers in Engineering, 51*(12),

    1344-1352.

Tan, X., Zeng, P., Yi, W., & Cheng, M. (2013). Graphene based digital microfluidics. Paper

    presented at the *Micro Electro Mechanical Systems (MEMS), 2013 IEEE 26th International*

    Conference On, 1195-1198.

Thaitrong, N., Kim, H., Renzi, R. F., Bartsch, M. S., Meagher, R. J., & Patel, K. D. (2012).

    Quality control of next-generation sequencing library through an integrative digital

    microfluidic platform. *Electrophoresis, 33*(23), 3506-3513.

Truckenmüller, R., Giselbrecht, S., Rivron, N., Gottwald, E., Saile, V., Van den Berg, A., . . .

    Van Blitterswijk, C. (2011). Thermoforming of Film-Based biomedical microdevices.

    Advanced Materials, 23(11), 1311-1329.

Vallet, M., Berge, B., & Vovelle, L. (1996). Electrowetting of water and aqueous solutions on

    poly (ethylene terephthalate) insulating films. *Polymer, 37*(12), 2465-2470.

Vancea, J., Reiss, G., Schneider, F., Bauer, K., & Hoffmann, H. (1989). Substrate effects on the surface topography of evaporated gold films—a scanning tunnelling microscopy investigation. *Surface Science, 218*(1), 108-126.

Vappou, J., Hou, G. Y., Marquet, F., Shahmirzadi, D., Grondin, J., & Konofagou, E. E. (2015). Non-contact, ultrasound-based indentation method for measuring elastic properties of biological tissues using harmonic motion imaging (HMI). *Physics in Medicine and Biology, 60*(7), 2853.

Walters, D., Cleveland, J., Thomson, N., Hansma, P., Wendman, M., Gurley, G., & Elings, V. (1996). Short cantilevers for atomic force microscopy. *Review of Scientific Instruments, 67*(10), 3583-3590.

Wheeler, A. R., Moon, H., Bird, C. A., Ogorzalek Loo, R. R., Kim, C. ", Loo, J. A., & Garrell, R. L. (2005). Digital microfluidics with in-line sample purification for proteomics analyses with MALDI-MS. *Analytical Chemistry, 77*(2), 534-540.

Wigginton, K. R., & Vikesland, P. J. (2010). Gold-coated polycarbonate membrane filter for pathogen concentration and SERS-based detection. *Analyst, 135*(6), 1320-1326.

Yafia, M., Ahmadi, A., Hoorfar, M., & Najjaran, H. (2015). Ultra-portable smartphone controlled integrated digital microfluidic system in a 3D-printed modular assembly. *Micromachines, 6*(9), 1289-1305.

Yafia, M., & Najjaran, H. (2013). High precision control of gap height for enhancing principal digital microfluidics operations. *Sensors and Actuators B: Chemical, 186*, 343-352.

Yeo, L. Y., & Friend, J. R. (2009). Ultrafast microfluidics using surface acoustic waves. *Biomicrofluidics, 3*(1), 012002.

Yeo, L. Y., & Friend, J. R. (2014). Surface acoustic wave microfluidics. *Annual Review of Fluid Mechanics, 46*, 379-406.

Zhang, C., Xu, J., Ma, W., & Zheng, W. (2006). PCR microfluidic devices for DNA amplification. *Biotechnology Advances, 24*(3), 243-284.

Zhao, H. (2011). Role of hydrodynamic behavior of DNA molecules in dielectrophoretic polarization under the action of an electric field. *Physical Review E, 84*(2), 021910.

Zhao, X., & Tan, Y. (2006). Neural network based identification of preisach-type hysteresis in piezoelectric actuator using hysteretic operator. *Sensors and Actuators A: Physical, 126*(2), 306-311.

Curriculum Vitae

Yiyan Li
PhD Candidate of Electrical and Computer Engineering
University of Nevada, Las Vegas
4505 S. Maryland Parkway
Las Vegas, NV 89154-4026
(+1) 702-688-0222
liy10@unlv.nevada.edu / yiyanli185@gmail.com
www.yilectronics.com

<u>EDUCATION</u>

University of Nevada, Las Vegas	**Electrical and Computer Engineering**	**PhD, 2012-2016**
Chongqing University	**Biomedical Engineering (Electrical)**	**M.S., 2009-2012**
Henan University of Science and Technology	**Biomedical Engineering (Electrical)**	**B.S., 2005-2009**

<u>RESEARCH AND DEVELOPMENT</u>

Areas of Interest: Sequencing, Integrated circuits and sensors; biosensors and bioelectronics; electromagnetics computation; neural modulation; semiconductor fabrication; RF electronics; medical instrumentation prototyping.

2012-Present
- **Design a high throughput digital microfluidic chip. (On-going research).**
  Including digital microfluidic chip design and fabrication; system design for pico-amps level current sensing; capacitive sensing system and its GUI monitoring system. Wireless controller (WiFi to serial converter) ESP8266 is used for real-time experiment control.

- **Design an ultrafast capacitive to digital converter for droplet sensing in digital microfluidics. (On-going research).**
  Using GFUS SiGe 8HP (0.13 µm) technology to fabricate an ultrafast capacitive to digital converter for droplet sensing in digital microfluidics.

- **Design a high precision DMF top plate height controller using a PZT actuator.**
  Including mechatronic design, vibration control, PZT precise positioning, PZT deflection modeling, displacement sensing, 12-bit digital-to-analog converter (DAC) MCP4921, PIC24fJ96 16-bit MCU, and intelligent DMF control.

- **Develop an on-chip integrated digital color-sensor based droplet PH value measurement system.**
  Including DMF patterning, TCS34725 RGB sensor, MCU interfaces, PIC24fJ96 16-bit MCU, and serial communications.

- **Investigation on the droplet motion under a beak-like non-parallel DMF device.**
  Including PZT bimorph actuator positioning, Omron Z4M-W40 laser displacement sensor, amplifier design, feedback control, DAC MCP4921, PIC24fJ96 16-bit MCU, and mechatronics. This work also includes droplet contact angle measurement, c.a. hysteresis evaluation, surface engineering, and dynamic droplet trajectory tracking.

- **Design a capacitance-to-digital sensor based droplet composition measurement system.**
  Use a 24-bit capacitive-to-digital converter (CDC) for droplet position monitoring in a DMF system. The system includes AD7745, Altera DE2 FPGA system, PCB design, and real-time monitoring by serial communications.

- **Design an ultra-thin flat lens with metamaterials for wave front shaping.**
  Electromagnetic numerical computation for a negative index nano-antenna array. The simulation is conducted by moment method, FDTD, and FEM.

- **Investigation on behavioral and pathological effects of transcranial direct current stimulation in a rat model of Alzheimer's disease.**
  Including design, layout, and fabricate the brain stimulator. Design feedback motor evoked potential monitoring system for the cortex excitability evaluation. Build neural disorder models of Alzheimer's disease. This study includes immunohistochemistry, HE, silver staining experiments, and tissue engineering-related study.

- **Design an electrowetting DMF chip on a CMOS ASIC chip.**
  Use high voltage ON's C5 technology, design an electrowetting surface directly on the passivation layer of a CMOS chip. Use the top metal layer as the electrode. Use on-chip decoders to address the electrodes. Use Cadence, ElectricVLSI, LtSpice for circuit design, simulation, and chip layout.

- **Design a continuous time K-Delta-1-Sigma modulator for broadband analog-to-digital conversion.**
  Design a time-interleaved oversampling delta-sigma modulator with ON's C5 technology. Use Cadence, ElectricVLSI, LtSpice for circuit design, simulation, and chip layout.

- **Design a commercial software for Hunter-Schmidt Meta-Analysis.**
  This tool is coded with VBA and multimedia authorware for Meta-Analysis experiments. This work includes algorithm implementation, software development, and on-line promotion.

- **Modeling the long-range ordered, broccoli-like SERS arrays for the detection of endocrine disrupting chemicals.**
  FDTD modeling for broccoli-like gold particle SERS fields.

2009-2012
- **Investigated behavioral and pathological effects of transcranial direct current stimulation in a rat model of Parkinson's disease.**

Stimulator circuit design, voltage booster design, skull electrode design, and rat PD model design; rat behavioral experiments and tissue staining.

▪ **Design an ultra-low power sleep monitoring device.**
Use low-power MCU TI MSP430 to monitor and analyze the pulse wave for sleep quality evaluation.

▪ **Design a portable ECG defibrillation overload recovery testing instrument.**
Develop a C8051 controlled, LabView interfaced ECG electrode testing equipment.

2008-2009
▪ **Undergraduate research on a low cost and high resolution intelligent on-line ECG system.**
PCB fabrication with in-house drills and copper boards; Circuit design and simulation using Altium PCB designer; ECG monitoring using National Instruments AD converters and LabView based online GUI.

TEACHING EXPERIENCE AT UNLV

I have teaching experiences in analog/digital integrated circuit design, computer logic basics, signal and systems, and the corresponding labs with CMOS integrated circuit fabrication, microcontrollers, AD/DA converters, FPGAs, circuit simulations, and system integration on PCBs. I have multiple project experiences of interfacing sensors, actuators to microcontrollers, and collecting, processing raw data using serial communication with PC. I am familiar with I2C, SPI, RS232, and USB protocols. I understand the basic operations of PLC and SCADA systems for instrumentation and process control.

2016 Spring
1. EE420L, Engineering Electronics II Lab.
Lectures will be given before the students start doing the labs. This course focused on analog circuit simulation and development, RC circuits, compensated scope probe circuit, op-amps, audio amplifiers, and beta-multipliers. Simulations are based on LTSpice, circuits are built with breadboards.

2. EE220, Circuit II. Tutoring homework and project problems and grading.

2015 Fall
1. EE421L, Digital Integrated Circuit Design Laboratory.
Lectures were given before the students start doing the labs. The main course contents are using Cadence to design and layout digital integrated circuits, such as digital to analog converters, logic gates, muxes, adders, and flip-flops. The final project of this lab is integrating all of the developed circuits in the semester into a 1.5 mm × 1.5 mm die, the chip was fabricated with MOSIS using ON's C5 technology.

2. EE621, Digital Integrated Circuit Design.

Tutoring homework problems and help on student project troubleshooting; configure CDK with Cadence on the server; collect, and grade circuit and layout files from students. Outcomes of this course: layout digital circuits and chips; design, estimate delays, and determine speed bottlenecks in digital circuits, describe the operation of MOSFETs using square law equations, discuss the movement of electrons and holes in pn-junctions and transistors under various operating conditions, and sketch the cross-sectional view of a layout.

2015 Spring
1. **EE420L, Engineering Electronics II Lab.**
Lectures will be given before the students start doing the labs. This course focused on analog circuit simulation and development, RC circuits, compensated scope probe circuit, op-amps, audio amplifiers, and beta-multipliers. Simulations are based on LTSpice, circuits are built with breadboards.

2. EE620, Engineering Electronics II and Analog Integrated Circuit Design.
Tutoring homework problems and help on student project troubleshooting; collect and grade homework and project files from students. Outcomes of this course: MOSFET spice parameters and operations; gain, speed, and matching trade-offs when setting the width, length, and overdrive of transistors; current mirrors, amplifiers, and differential amplifiers; voltage and current references; op-amps; frequency response; op-amps stability.

2014 Fall
1. EE460L, Communications Lab.
Tutoring communication labs and helping on theoretical and experimental verification of DSBSC, FM modulation, PCM coding / encoding, baseband digital communication and BER in noisy channel using TIMS 301 communication module.

2. CPE200L, Computer Logic Design Lab II.
This is an FPGA based advanced computer logic design lab. This course covers serial communication, random number generators, multipliers and Nios II processors, and a final project.

2014 Spring
1. CPE200L, Computer Logic Design Lab II.
This is an FPGA based advanced computer logic design lab. This course covers serial communication, random number generators, multipliers and Nios II processors, and a final project.

2. EE320, Engineering Electronics I.
Tutoring homework problems and help on project troubleshooting; grading homework and projects. This course covers inverting and non-inverting op-amps, integrators' output current of MOSTETs and diodes; diode circuit design and analysis; amplifier design and analysis; use spice for circuit simulation.

2013 Fall
1. CPE100L, Computer Logic Design Lab.

This is an FPGA based advanced computer logic design lab. This course covers logic gates, combinational logic, multiplexers, ALU, alarms design, clock design, and final project.

2. CPE100, Computer Logic Design.
Tutoring homework problems and help on project troubleshooting; grading homework and projects. This course covers basic concepts in computer engineering; binary, octal, decimal and hexadecimal systems; Arithmetics of non-decimal numbers; logic gates; combinational logics; sequential logics; clocked synchronous state machines.

3. EE360, Signal and Systems.
Tutoring homework problems and help on project troubleshooting; grading homework and projects. This course covers fundamentals of signal and system analysis, focusing on representations of discrete-time and continuous-time signals and representations of linear, time-invariant systems. Applications are drawn broadly from engineering and physics, including feedback and control, communications, and signal processing.

WORK EXPERIENCES

1. Software Engineer, 03/01/2014-03/01/2015, website and Apps development, 3E Promotions, LLC.
2. Software Engineer, 03/05/2013-01/05/2014, meta-analysis commercial software development, department of management at UNLV.
3. Electrical Engineer Intern, 10/01/2009-01/01/2011, electrical brain stimulator and sleep monitoring system development, Chongqing Haikun Medical Instrumentation, LLC.
4. CT/MRI Engineer Intern, 10/01/2008-03/01/2009, internship of pathological diagnostics using CT/MRI, Orthepedic Hospital at Luoyang.

TECHNICAL SKILLS AND DESIGN TOOLS

Electrical & Computer Engineering Design Tools: Cadence Virtuoso, Electric VLSI, Spectre, UltraSim, LTSpice, Cadence Diva, Mentor Graphics Calibre, Altera Quartus II and DE2 FPGA System, Lumerical FDTD, Moment Method Programing, Remcom Xfdtd, and Visual Basic.NET with Microsoft Access.
Biological & Biomedical Experiment Skills: Tissue processing, cryostat and paraffin tissue section, H&E, cell cultures, immunohistochemistry.
Nanofabrication: Photolithography, E-beam deposition, microfluidic device patterning.

HONORS AND AWARDS

2016 UNLV GPSA Forum Presentation Award
2015 UNLV GPSA Award.
2013 NASA EPSCoR Fellowship.
2011 CQU VSCF Award.
2009 HAUST Annual Leadership Award.
2009 Henan Province Outstanding Undergraduate Alumni Award.

SUBMITTED JOURNAL ARTICLES

1. **Y. Li** and R. Jacob Baker. Droplet transportation under subthreshold voltages in digital microfluidics with top plate vibrations. *Applied Physics Letters*. **Submitted**.
2. **Y. Li** and R. Jacob Baker. Droplet transportation in a beak-like EWOD DMF device. *Microfluidics and Nanofluidics*. **Submitted.**

PUBLICATIONS

Y. Li and R. Jacob Baker. Improving the performance of electrowetting on dielectric microfluidics using piezoelectric top plate control. *Sensors and Actuators B: Chemical*, 229 (2016) 63-74.

Y. Li, H. Li and R. Jacob Baker. A low-cost and high-resolution droplet position detector for an intelligent electrowetting on dielectric device. *Journal of Laboratory Automation*. 20 (2015) 663-669.

Y. Li and R. Jacob Baker. Precise EWOD top plate positioning using inverse Preisach model based hysteresis compensation. *IEEE Dallas Circuits and Systems Conference*. (2015) 1-4.

Y. Li and R. Jacob Baker. A highly efficient and reliable electrowetting on dielectric device for point-of-care diagnostics. *IEEE Dallas Circuits and Systems Conference*. (2015) 1-4.

Y. Li and R. Jacob Baker. Computer vision assisted measurement of the displacements of a bimorph piezoelectric cantilever beam. *IEEE Biomedical Circuits and Systems Conference*. (2015) 1-4.

Y. Li, R. Chen and R. J. Baker. A fast fabricating electro-wetting platform to implement large droplet manipulation. *IEEE International Midwest Symposium on Circuits and Systems*. (2014) 326-329.

Y. Li, H. Li and R. J. Baker. Volume and concentration identification by using an electrowetting on dielectric device. *IEEE Dallas Circuits and Systems Conference*. (2014) 1-4.

Y. Li, X. Tian, L. Qian, X. Yu and W. Jiang. Anodal transcranial direct current stimulation relieves the unilateral bias of a rat model of Parkinson's disease. *IEEE Engineering in Medicine and Biology Society*. (2011) 765-768.

K. Huang, **Y. Li**, X. Tian, D. Zeng, X. Gao. Design and analyses of an ultra-thin flat lens for wave front shaping in the visible. *Physics Letters A*. 379 (2015) 3008-3012.

X. Yu, **Y. Li**, H. Wen, Y. Zhang, X. Tian. Intensity-dependent effects of repetitive anodal transcranial direct current stimulation on learning and memory in a rat model of Alzheimer's disease. *Neurobiology of Learning and Memory*. 123 (2015) 168-178.

T. Wang, Z. Zhang, **Y. Li**, G. Xie. Amplified electrochemical detection of mecA gene in methicillin-resistant Staphylococcus aureus based on target recycling amplification and isothermal strand-displacement polymerization reaction. *Sensors and Actuators B: Chemical*. 221 (2015) 148-154.

J. Chen, G. Qin, W. Shen, **Y. Li** and B. Das. Fabrication of long-range ordered, broccoli-like SERS arrays and application in detecting endocrine disrupting chemicals. *Journal of Materials Chemistry C*. 3 (2015) 1309-1318.

J. Chen, W. Shen, B. Das, **Y. Li** and G. Qin. Fabrication of tunable au SERS nanostructures by a versatile technique and application in detecting sodium cyclamate. *Rsc Advances*. 4 (2014) 22660-22668.

X. Jing, X. Cao, L. Wang, T. Lan, **Y. Li** and G. Xie. DNA-AuNPs based signal amplification for highly sensitive detection of DNA methylation, methyltransferase activity and inhibitor screening. *Biosensors and Bioelectronics*. 58 (2014) 40-47.

C. Ma, M. Liang, L. Wang, H. Xiang, Y. Jiang, **Y. Li** and G. Xie. MultisHRP-DNA-coated CMWNTs as signal labels for an ultrasensitive hepatitis C virus core antigen electrochemical immunosensor. *Biosensors and Bioelectronics*. 47 (2013) 467-474.

J. Li, X. Tian and **Y. Li**. Design of temperature control system for burn-avoiding infrared physiotherapy apparatus based on fuzzy PID. *Transducer and Microsystem Technologies*. 1 (2012) 120-123.

L. Luo, X. Tian, P. Zhang and **Y. Li**. Defibrillation overload recovery performance test system for ECG electrode. *Chinese Journal of Scientific Instrument.* 32 (2011) 1981-1986.

L. Li, X. Tian and **Y. Li**. Amplitude and phase measurement circuit design used on neuromuscular disease assessment system. *Application of Electronic Technique*. 37 (2011) 1-8.

J. Zhang, X. Tian and **Y. Li**. Design on MSP430-based portable sleep monitoring instrument. *Transducer and Microsystem Technologies*. 30 (2011) 118-121.